

INTERIM  
IN-43-CR  
OCT.  
43615

p-83

SEMI-ANNUAL REPORT

(for July - December 1994)

Contract Number NAS5-31363

OCEAN OBSERVATIONS WITH EOS/MODIS:

Algorithm Development and Post Launch Studies

Howard R. Gordon  
University of Miami  
Department of Physics  
Coral Gables, FL 33124

(Submitted January 13, 1995)

(NASA-CR-197894) OCEAN  
OBSERVATIONS WITH EOS/MODIS:  
ALGORITHM DEVELOPMENT AND POST  
LAUNCH STUDIES Semiannual Report, 1  
Jul. - 31 Dec. 1994 (Miami Univ.)  
83 p

N95-23473

Unclass

G3/43 0043615



### Abstract

Several significant accomplishments were made during the present reporting period.

- Initial simulations to understand the applicability of the MODIS 1380 nm band for removing the effects of stratospheric aerosols and thin cirrus clouds were completed using a model for an aged volcanic aerosol. The results suggest that very simple procedures requiring no *a priori* knowledge of the optical properties of the stratospheric aerosol may be as effective as complex procedures requiring full knowledge of the aerosol properties, except the concentration which is estimated from the reflectance at 1380 nm. The limitations of this conclusion will be examined in the next reporting period.
- The lookup tables employed in the implementation of the atmospheric correction algorithm have been modified in several ways intended to improve the accuracy and/or speed of processing. These have been delivered to R. Evans for implementation into the MODIS prototype processing algorithm for testing.
- A method was developed for removal of the effects of the O<sub>2</sub> "A" absorption band from SeaWiFS band 7 (745-785 nm). This is important in that SeaWiFS imagery will be used as a test data set for the MODIS atmospheric correction algorithm over the oceans.
- Construction of a radiometer, and associated deployment boom, for studying the spectral reflectance of oceanic whitecaps at sea was completed. The system was successfully tested on a cruise off Hawaii on which whitecaps were plentiful during October-November. This data set is now under analysis.

## 1. Atmospheric Correction Algorithm Development

### a. Task Objectives:

During CY 1994 there are five objectives under this task:

(i) Investigate the effects of stratospheric aerosol on the proposed correction algorithm, and investigate the possible use of the 1380 nm MODIS band to remove the stratospheric aerosol perturbation.

(ii) Investigate the effect of vertical structure in aerosol concentration and type on the behavior of the proposed correction algorithm.

(iii) Investigate the effects of polarization on the accuracy of the algorithm.

(iv) Improve the accuracy and speed of the existing algorithm.

(v) Investigate removal of the O<sub>2</sub> "A" absorption band at 762 nm from the 745-785 nm SeaWiFS band so the latter can be used in atmospheric correction of SeaWiFS. The importance of this to MODIS is that SeaWiFS data will be used extensively to test and improve the MODIS algorithm. Thus, it is essential for the MODIS algorithm development and testing, that the O<sub>2</sub> absorption be adequately dealt with for SeaWiFS.

### b. Work Accomplished:

(i) We have completed the addition of a third layer to our successive order of scattering radiative transfer code to include stratospheric aerosols. A literature search was carried out and three stratospheric aerosol models were selected representing a background stratospheric aerosol, a fresh volcanic aerosol, and an aged volcanic aerosol. Computations of the optical properties of the aerosol were carried out and initial radiative transfer simulations have been performed. The third layer in the model contains the stratospheric aerosol. To simulate the radiance observed in the 1380 nm band we use a single layer in our code and omit the Fresnel-reflecting sea surface.

This in effect assumes that all of the photons that penetrate through the stratospheric aerosol are immediately absorbed by water vapor in the free troposphere.

In the absence of stratospheric aerosol, the total reflectance  $\rho_t(\lambda)$ , at a wavelength  $\lambda$ , measured by MODIS can be decomposed as follows:

$$\rho_t(\lambda) = \rho_r(\lambda) + \rho_a(\lambda) + \rho_{ra}(\lambda) + t(\theta_v, \lambda)\rho_w(\lambda), \quad (1)$$

where  $\rho_r(\lambda)$  is the radiance resulting from multiple scattering by air molecules (Rayleigh scattering) in the absence of aerosols,  $\rho_a(\lambda)$  is the radiance resulting from multiple scattering by aerosols in the absence of the air, and  $\rho_{ra}(\lambda)$  is the interaction term between molecular and aerosol scattering.<sup>1</sup> In this equation,  $t$  is the diffuse transmittance of the atmosphere along the viewing direction specified by  $\theta_v$ , the angle between the normal to the sea surface and the sensor.<sup>2</sup> Radiance arising from specular reflection of direct sunlight from the sea surface (sun glitter) has been ignored because SeaWiFS can be tilted away from the glitter pattern. The influence of whitecaps has also been ignored under the assumption that their contribution can be removed from an estimate of the surface wind speed.<sup>3</sup> The goal of the atmospheric correction is the retrieval of  $\rho_w$  from  $\rho_t$ .

The stratospheric aerosol contributes to the reflectance at all of the MODIS ocean bands. Thus, in the presence of the stratospheric aerosol layer the reflectance will be increased by an amount  $\delta\rho_t^{(s)}$ , i.e.,

$$\rho_t^{(s)}(\lambda) = \rho_t(\lambda) + \delta\rho_t^{(s)}(\lambda),$$

where  $\rho_t^{(s)}$  is the reflectance of the entire ocean-atmosphere system in the presence of stratospheric aerosol. As much of this contribution as possible should be removed from the visible and NIR bands before applying the atmospheric correction. Thus, the goal is to be able to remove  $\delta\rho_t^{(s)}(\lambda)$  from  $\rho_t^{(s)}(\lambda)$  before applying the atmospheric correction algorithm, which was developed for application to  $\rho_t(\lambda)$ .

We have carried out simulations of radiative transfer with our three-layer model to examine several possibilities for utilizing the 1380 nm band for correction for stratospheric aerosols. Although, the analysis of these computations is incomplete, we will provide a brief report of the results thus far.

It is assumed that the reflectance at 1380 nm is totally due to the stratospheric aerosol. Also, as usual it is assumed that the aerosol properties in the lower layer are completely unknown. The atmospheric correction algorithm, as presently implemented, is then operated in several ways using the three-layer computations as pseudodata.

1. The "measured" reflectances at 443, 765 and 865 are used in the algorithm as usual, i.e., no attention is paid to the fact that a stratospheric aerosol may be present [ $\rho_t^{(s)}(\lambda)$  assumed to be  $\rho_t(\lambda)$ ], and the error in the atmospheric correction at 443 nm is determined.
2. The stratospheric aerosol is incorporated into the algorithm by simply subtracting the reflectance at 1380 nm from those at 443, 765, and 865, i.e.,  $\rho_t(\lambda) = \rho_t^{(s)}(\lambda) - \rho_t^{(s)}(1380)$ . These are then inserted into the correction algorithm and determining the error in the correction at 443 nm is determined.
3. It is assumed that the spectral variation of the optical thickness of the stratospheric aerosol is known (either from an instrument like SAGE or from measurements from the surface). The reflectance at 1380 nm (due entirely to the stratospheric aerosol) is scaled by the ratio of the stratospheric optical depth at the given  $\lambda$ ,  $\tau_s(\lambda)$ , to that at (or in the case of surface measurements, near) 1380 nm, and subtracted from the measured reflectances at the other wavelengths, i.e.,

$$\rho_t(\lambda) = \rho_t^{(s)}(\lambda) - \frac{\tau_s(\lambda)}{\tau_s(1380)} \rho_t^{(s)}(1380)$$

The  $\rho_t(\lambda)$  are then inserted into the correction algorithm and the error in the correction at 443 nm determined.

4. It is assumed that accurate measurements or predictions of the other optical properties of the stratospheric aerosol, the spectral scattering phase function and single scattering albedo, along with the spectral variation of the optical depth are available for the stratospheric aerosol. The reflectance at 1380 nm is then scaled, by the ratio of the single-scattered stratospheric aerosol reflectances at  $\lambda$  to that at 1380 nm, and subtracted from the reflectances in the visible and NIR, i.e.,

$$\rho_t(\lambda) = \rho_t^{(s)}(\lambda) - \frac{\omega_s(\lambda)\tau_s(\lambda)p_s(\theta_v, \phi_v; \theta_0, \phi_0; \lambda)}{\omega_s(1380)\tau_s(1380)p_s(\theta_v, \phi_v; \theta_0, \phi_0; 1380)} \rho_t^{(s)}(1380),$$

where

$$p_s(\theta_v, \phi_v; \theta_0, \phi_0; \lambda) = P_s(\theta_-, \lambda) + (r(\theta_v) + r(\theta_0)) P_s(\theta_+, \lambda),$$

$$\cos \theta_{\pm} = \pm \cos \theta_0 \cos \theta_v - \sin \theta_0 \sin \theta_v \cos(\phi_v - \phi_0),$$

and  $\tau(\alpha)$  is the Fresnel reflectance of the interface for an incident angle  $\alpha$ . The parameters  $\tau_s(\lambda)$ ,  $\omega_s(\lambda)$ , and  $P_s(\alpha, \lambda)$  are, respectively, the stratospheric aerosol optical thickness, single scattering albedo, and scattering phase function for a scattering angle  $\alpha$ . The angles  $\theta_0$  and  $\phi_0$  are, respectively, the zenith and azimuth angles of a vector from the point on the sea surface under examination (pixel) to the sun, and likewise,  $\theta_v$  and  $\phi_v$  are the zenith and azimuth angles of a vector from the pixel to the sensor. These are measured with respect to the *upward* normal so  $\theta_v$  and  $\theta_0$  are both less than  $90^\circ$ . The resulting values of  $\rho_t(\lambda)$  are then inserted into the correction algorithm and the error at 443 nm is determined. This procedure is based on the assumption that the stratospheric aerosol enhancement of  $\rho_t$  is all due to single scattering.

5. As in (4) it is assumed that all of the optical properties of the aerosol are known except the concentration. A one-layer multiple scattering code (with a totally absorbing lower surface to represent the troposphere) is used to determine  $\tau_s(1380)$  from  $\rho_t^{(s)}(1380)$ . This determines all of the optical properties of the stratospheric aerosol. These properties are inserted into a one-layer multiple scattering code (with a Fresnel-reflecting sea surface as the lower boundary) to compute  $\delta\rho_t^{(s)}(\lambda)$ , which is subtracted from the measured reflectances  $\rho_t^{(s)}(\lambda)$  to provide  $\rho_t(\lambda)$ . The resulting values of  $\rho_t(\lambda)$  are then inserted into the correction algorithm and the error at 443 nm is determined. This procedure is based on the assumption that there is *no radiative interaction* between the stratospheric aerosol layer and the other two layers.
6. Except for the step in which  $\delta\rho_t^{(s)}(\lambda)$  is removed from  $\rho_t(\lambda)$ , this is identical to procedure 5. Once all of the optical properties of the stratospheric aerosol are known, they are inserted into a *two-layer* multiple scattering code (as opposed to a *one-layer* code in procedure 5 above) with a Fresnel-reflecting sea surface as the lower boundary. The top layer consists of the stratospheric aerosol and the lower layer has only Rayleigh scattering. This incorporates the Rayleigh-stratospheric aerosol interaction explicitly (albeit approximately because of the absence of the tropospheric aerosol), leaving only the Rayleigh-tropospheric aerosol and stratospheric-tropospheric aerosol interactions unaddressed. After subtracting the result of this computation from  $\rho_t^{(s)}(\lambda)$ , the result is inserted into the standard correction algorithm in which allowance is made for the fact that  $\rho_r$  has already been removed with the stratospheric component. This approach is possible because the properties of the Rayleigh scattering layer are completely known.

We now present the results obtained using these procedures for cases with an aged volcanic aerosol in the stratosphere with  $\tau_s = 0.05$  and  $0.15$ , and a Maritime aerosol (relative humidity 80%) with  $\tau_a = 0.15$  in the marine boundary layer. In the absence of stratospheric aerosol, the

algorithm yields an almost perfect atmospheric correction. Figures 1 and 2 provide the error in the recovered value of  $t\rho_w(443)$  for each of the procedures above. On the figures the procedure number is given with the description of the symbols. The goal is that the error approach that which would be obtained were the stratospheric aerosol *absent*, which is provided by the very heavy black line. In the model description on the figures, the symbols "3L," "2L," "R," "S," and "(R+S)" stand for radiances computed from a three-layer model, a two-layer model, a one-layer model with Rayleigh scattering only, a one-layer model with stratospheric aerosol scattering only, and a two-layer model with stratospheric aerosols on the top and molecular scattering in the bottom.

To no surprise, the most complex method of dealing with the stratospheric aerosol (No. 6 above) yields the best overall correction; however, the second best methods (Nos. 1 and 2) are the simplest and require absolutely no *a priori* knowledge of the stratospheric aerosol's optical properties. This is similar the Gordon and Castaño<sup>4</sup> conclusion regarding the influence of the El Chichón aerosol on CZCS atmospheric correction, i.e., that the presence of the aerosol had little effect on atmospheric correction.

(ii) A Monte Carlo code employing a fifty-layer atmosphere has been developed to carry out this investigation. To realistically treat the aerosol in the code, we divided the atmosphere into four broad regions: (1) the marine boundary layer from the surface to 2 km, where the aerosol concentration is independent of altitude; (2) the free troposphere, where the aerosol concentrations varies in proportion to  $\exp[-z/h]$ , where  $z$  is the altitude (2-12 km) and  $h$  (the scale height) is 2 km; (3) the background stratosphere (12-30 km), where the aerosol concentration is also exponential with a scale height of 5 km; and (4) a volcanic region (20-25 km) within the stratosphere which can contain a uniformly mixed volcanic aerosol. The optical properties of each of the four regions can be characterized by individual aerosol models, and any of the regions can be free of aerosols if desired.



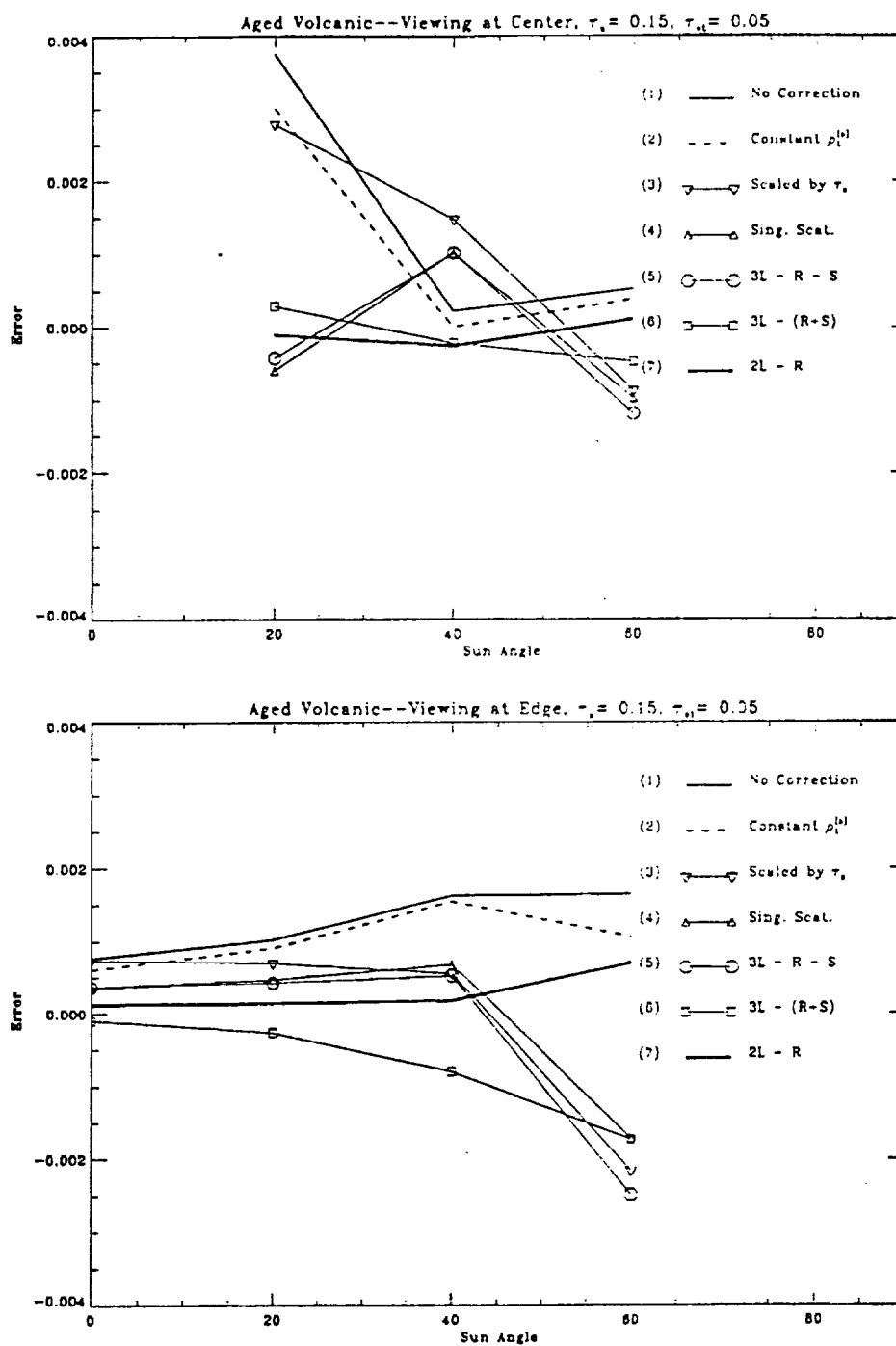


Figure 1. Error in retrieved water-leaving reflectance as a function of the solar zenith angle for several methods of dealing with the stratospheric aerosol (1-6).  $\tau_a = 0.15$ ,  $\tau_{st} = 0.05$ . Top: scan center, bottom: scan edge.

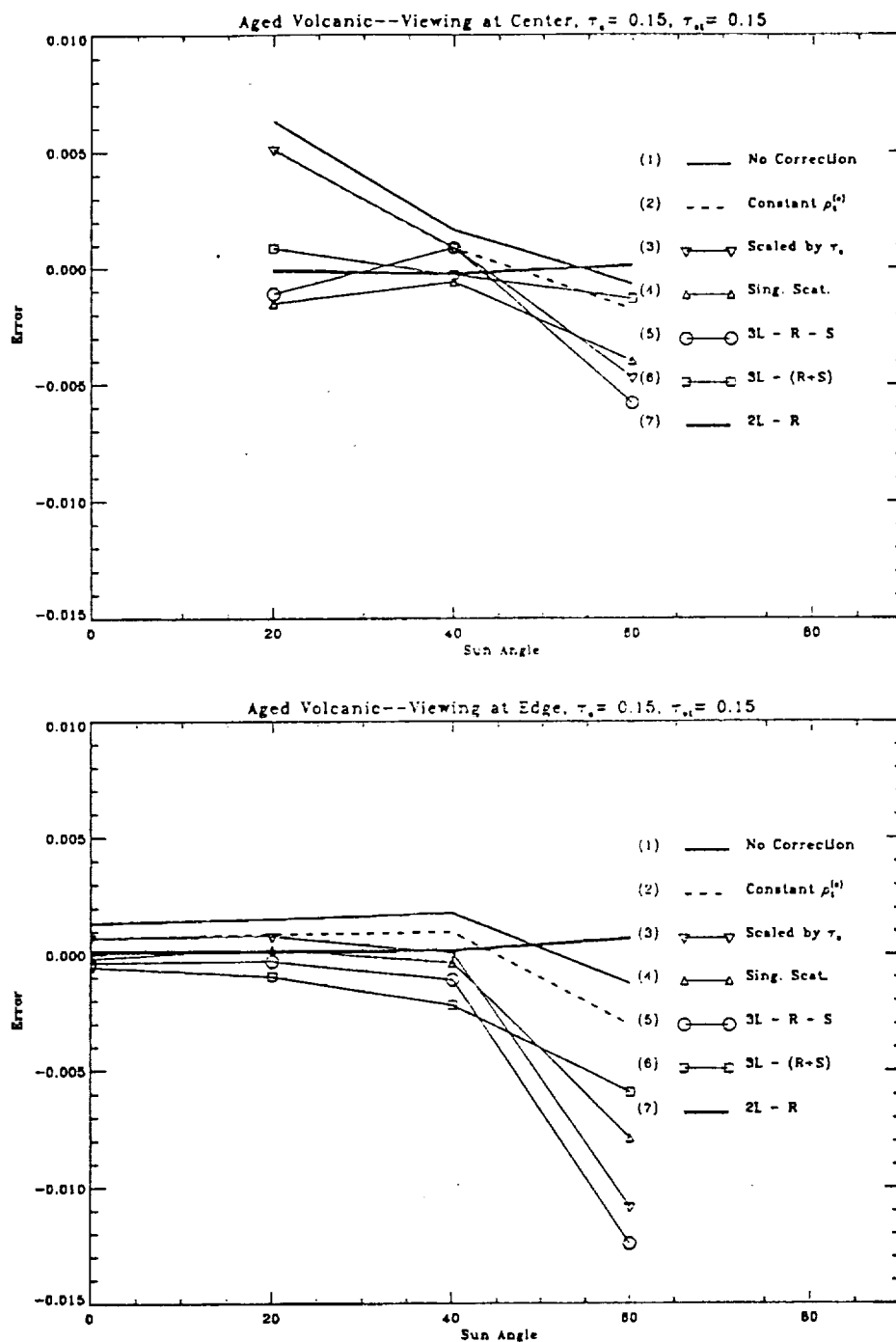


Figure 2. Error in retrieved water-leaving reflectance as a function of the solar zenith angle for several methods of dealing with the stratospheric aerosol (1-6).  $\tau_a = 0.15$ ,  $\tau_{st} = 0.15$ . Top: scan center, bottom: scan edge.

The models for the two lower regions are taken from Shettle and Fenn.<sup>5</sup> Briefly, based on size distribution and composition measurements they developed two models with log-normal size distributions called the Tropospheric (to model the aerosol in the free troposphere — few large particles) and the Oceanic (to model the aerosol produced by sea spray — few small particles). They combined these to form the Maritime model to represent the aerosol in the marine boundary layer. In terms of total aerosol number per unit volume the Maritime model consists of 99% Tropospheric and 1% Oceanic. Gordon and Wang<sup>6</sup> added a Coastal model (99.5% Tropospheric and 0.5% Oceanic) to provide a description of the aerosol that might be more representative of the boundary layer near the coast.

For the two upper regions we use a model for the background stratosphere from the WMO<sup>7</sup> and for the volcanic aerosol from King et al.<sup>8</sup> Both models assume a 75% solution of  $\text{H}_2\text{SO}_4$ . We have also included a volcanic ash model<sup>7</sup> to represent fresh volcanic aerosol. The size distributions in these regions are modified gamma distributions.

The code contains provision for a wind-roughened sea surface with a surface slope distribution governed by the Cox and Munk<sup>9</sup> probability density function.

Preliminary computations (using the code) relating to the influence of vertical structure of the aerosol on atmospheric correction (the algorithm assumes that the aerosol is all in the surface boundary layer) have been carried out. These show an increased error in the retrievals in the presence of vertical structure; however, the error is not excessive. We have not progressed further with this aspect of the study as we decided to complete the addition of polarization to the code first (the next item).

(iii) We have added polarization to our fifty-layer Monte Carlo code. Initial exercising of the code has been for an aerosol-free atmosphere. In this case the results agree with our successive order of scattering code<sup>10</sup> to within  $\sim 0.1\%$  for an atmosphere bounded by a flat Fresnel-reflecting ocean. For a sea surface roughened by the wind, differences in the two codes of the order of  $\sim 0.5\%$  persist. Considerable effort on this part of the project during the last three months has been devoted to tracking down the source of this difference.

(iv) For the implementation of our correction algorithm,<sup>6</sup> extensive lookup tables relating  $\rho_t - \rho_r - t\rho_w = \rho_a + \rho_{ra}$  to the single-scattered aerosol radiance,  $\rho_{as}$ , are required for each aerosol model we employ. Initially, we related  $\rho_a + \rho_{ra}$  to  $\rho_{as}$  by

$$\log[\rho_t(\lambda) - \rho_r(\lambda) - t\rho_w(\lambda)] = \log[a(\lambda)] + b(\lambda)\log[\rho_{as}(\lambda)], \quad (2)$$

where  $a(\lambda)$  and  $b(\lambda)$  are the function of wavelength and the geometry. [For details, see the MODIS water-leaving radiance ATBD Version 2.] For a given aerosol model, we calculated the  $a$  and  $b$  from a linear fit of  $\log(\rho_t - \rho_r - t\rho_w)$  to  $\log(\rho_{as})$  for each wavelength and the given geometry, i.e., for all  $\theta_v$ ,  $\theta_0$ ,  $\phi_v$  and  $\lambda$ , from simulations, using the method of least-squares. This resulted in a relationship that depends only on the aerosol model and geometry. It reduces the data storage of 3 ~ 4 times since the values of  $\rho_t - \rho_r - t\rho_w$  and  $\rho_{as}$  need not be stored for each aerosol concentration, i.e., optical thickness ( $\tau_a$ ). For the angle  $\phi_v$ , however, we still have to store  $a(\lambda)$  and  $b(\lambda)$  for a large number of values of the angle  $\phi_v$  for interpolation. To further reduce storage, we expanded  $a(\lambda)$  and  $b(\lambda)$  in a Fourier series in  $\phi_v$  and stored only the Fourier coefficients. All of the reflectances are even functions of the relative azimuth angle  $\phi_v$ , so  $\rho_t - \rho_r - t\rho_w$  and  $\rho_{as}$  are as well, and  $a(\lambda)$  and  $b(\lambda)$  will be even functions of  $\phi_v$ . Thus, we can write

$$a(\theta_v, \theta_0, \lambda, \phi_v) = a^{(0)}(\theta_v, \theta_0, \lambda) + 2 \sum_{m=1}^M a^{(m)}(\theta_v, \theta_0, \lambda) \cos m\phi_v,$$

$$b(\theta_v, \theta_0, \lambda, \phi_v) = b^{(0)}(\theta_v, \theta_0, \lambda) + 2 \sum_{m=1}^M b^{(m)}(\theta_v, \theta_0, \lambda) \cos m\phi_v,$$

or

$$a^{(m)}(\theta_v, \theta_0, \lambda) = \frac{1}{\pi} \int_0^\pi a(\theta_v, \theta_0, \lambda, \phi_v) \cos m\phi_v d\phi_v,$$

$$b^{(m)}(\theta_v, \theta_0, \lambda) = \frac{1}{\pi} \int_0^\pi b(\theta_v, \theta_0, \lambda, \phi_v) \cos m\phi_v d\phi_v.$$

$a(\lambda)$  and  $b(\lambda)$  for any  $\phi_v$  can then be obtained easily from the stored values of  $a^{(m)}$  and  $b^{(m)}$ . We have now investigated the use of azimuthal interpolation in place of the Fourier transform. This will increase the size of the tables; however, it may increase the speed. Also, to see if the accuracy of the lookup tables could be improved, we have also replaced Eq. (2) by

$$\log[\rho_t(\lambda) - \rho_r(\lambda) - t\rho_w(\lambda)] = \log[a(\lambda)] + b(\lambda)\log[\rho_{as}(\lambda)] + c(\lambda)\log^2[\rho_{as}(\lambda)]. \quad (3)$$

In the implementation of this using the Fourier transform, this increases the size of the lookup tables by 50%.

We have compared the accuracy of the atmospheric correction for standard test cases used in the MODIS water-leaving radiance ATBD, i.e., the Maritime, Coastal, and Tropospheric aerosol models with a relative humidity of 80%,  $\tau_a = 0.2$  and  $0.4$ , solar zenith angles from  $\theta_0 = 0$  to  $60^\circ$ , azimuth angle  $\phi_v = 90^\circ$ , and viewing angle  $\theta_v \approx 45^\circ$  (scan edge). The scan center is not examined because the reflectance there is independent of  $\phi_v$ . The results are presented in Tables 1-6. In the tables, the terms "linear" and "quad" refer to Eq. (2) and (3), respectively, the term "Fourier" refers to computations with 15 Fourier coefficients for  $a$ ,  $b$ , and  $c$  (for the "quad" cases), and the numbers, 19, 24, and 37, refer to the number of values of  $\phi_v$  used in the azimuthal interpolation. Noting that the maximum error in water-leaving reflectance at 443 nm is  $\pm 0.001$ - $0.002$ , we note that there is little difference between the various schemes, with the exception that the quadratic fitting procedure [Eq. (3)] produces superior results for the Tropospheric cases with large  $\theta_0$ . Thus, the choice probably should be based on the speed of the various algorithms.

(v) To simulate radiative transfer in the  $O_2$  absorption, we modified our fifty-layer simulation code so that line-by-line computations could be carried out. What we wanted to learn was the influence of the  $O_2$  absorption on the radiance or the reflectance leaving the top of the atmosphere (TOA) in a band extending from 745 to 785 nm (SeaWiFS band 7). Specifically, since the proposed SeaWiFS/MODIS algorithm ignores the  $O_2$  absorption, our goal was to be able to estimate what the TOA radiance would be in the absence of the absorption band.

This study has been completed. Two simple modifications to the SeaWiFS algorithm suffice to correct for the absorption in the absence of stratospheric aerosols. A possible strategy for detecting stratospheric aerosols and/or thin cirrus clouds was also suggested. The complete study is included as Appendix 1. A paper describing the results is in press in *Applied Optics*.

c. Data/Analysis/Interpretation: See item b above.

d. Anticipated Future Actions:

Table 1: Error in retrieved water leaving reflectance  
for viewing at edge through Tropospheric aerosols.  
True value of  $\tau_a(865)$  is 0.20.

| Algorithm       | $\theta_0$  |             |             |             |
|-----------------|-------------|-------------|-------------|-------------|
|                 | 0°          | 20°         | 40°         | 60°         |
| linear Fourier  | +1.2787E-04 | +1.8096E-04 | +5.7206E-05 | -1.5225E-03 |
| linear 19       | +1.2787E-04 | +2.1100E-04 | +1.3915E-04 | -1.4221E-03 |
| quad. Fourier   | -9.9469E-05 | -6.1776E-05 | +1.7423E-05 | +1.9481E-04 |
| quad. linear 19 | -9.9469E-05 | -3.3934E-05 | +1.0664E-04 | +2.8400E-04 |
| quad. linear 24 | -9.9469E-05 | -6.8206E-04 | +2.8372E-05 | +1.8390E-04 |
| quad. linear 37 | -9.9469E-05 | -5.8398E-04 | +4.6089E-05 | +2.0859E-04 |

Table 2: Error in retrieved water leaving reflectance  
for viewing at edge through Coastal aerosols.  
True value of  $\tau_a(865)$  is 0.20.

| Algorithm       | $\theta_0$  |             |             |             |
|-----------------|-------------|-------------|-------------|-------------|
|                 | 0°          | 20°         | 40°         | 60°         |
| linear Fourier  | +2.1622E-05 | +1.8054E-04 | +5.7206E-04 | +1.6048E-03 |
| linear 19       | +2.1622E-05 | +1.9103E-04 | +5.9777E-04 | +1.5984E-03 |
| quad. Fourier   | -1.4609E-04 | -1.7202E-05 | +2.9835E-04 | +1.2792E-03 |
| quad. linear 19 | -1.4609E-04 | -4.1556E-06 | +3.2136E-05 | +1.2924E-03 |
| quad. linear 24 | -1.4609E-04 | -1.7000E-04 | +2.8661E-04 | +1.2534E-03 |
| quad. linear 37 | -1.4609E-04 | -1.3556E-05 | +2.9393E-04 | +1.2632E-03 |

Table 3: Error in retrieved water leaving reflectance  
for viewing at edge through Maritime aerosols.  
True value of  $\tau_a(865)$  is 0.20.

| Algorithm       | $\theta_0$  |             |             |             |
|-----------------|-------------|-------------|-------------|-------------|
|                 | 0°          | 20°         | 40°         | 60°         |
| linear Fourier  | +6.4034E-05 | +7.1921E-05 | +5.9443E-05 | -1.3646E-05 |
| linear 19       | +6.3950E-07 | +7.5364E-05 | +3.0333E-05 | +7.6612E-05 |
| quad. Fourier   | -5.2648E-05 | -8.7184E-05 | -2.1609E-04 | -3.5412E-04 |
| quad. linear 19 | -5.2648E-05 | -7.2438E-05 | -2.0611E-05 | -3.1127E-04 |
| quad. linear 24 | -5.2648E-05 | -8.8141E-05 | -2.1783E-04 | -3.6232E-04 |
| quad. linear 37 | -5.2648E-05 | -8.6554E-05 | -2.1681E-04 | -3.5245E-04 |

Table 4: Error in retrieved water leaving reflectance  
for viewing at edge through Tropospheric aerosols.  
True value of  $\tau_a(865)$  is 0.40.

| Algorithm       | $\theta_0$  |             |             |             |
|-----------------|-------------|-------------|-------------|-------------|
|                 | 0°          | 20°         | 40°         | 60°         |
| linear Fourier  | -1.6432E-03 | -2.0691E-03 | -4.2873E-03 | -1.1461E-02 |
| linear 19       | -1.6432E-03 | -2.0169E-03 | -4.1456E-03 | -1.1328E-02 |
| quad. Fourier   | -1.1468E-03 | -1.5905E-03 | -3.4071E-03 | -6.7699E-03 |
| quad. linear 19 | -1.1468E-03 | -1.5418E-03 | -3.2215E-03 | -6.6015E-03 |
| quad. linear 24 | -1.1468E-03 | -1.6033E-03 | -3.3762E-03 | -6.8075E-03 |
| quad. linear 37 | -1.1468E-03 | -1.5905E-03 | -3.3365E-03 | -6.7561E-03 |

Table 5: Error in retrieved water leaving reflectance  
for viewing at edge through Coastal aerosols.  
True value of  $\tau_a(865)$  is 0.40.

| Algorithm       | $\theta_0$  |             |             |             |
|-----------------|-------------|-------------|-------------|-------------|
|                 | 0°          | 20°         | 40°         | 60°         |
| linear Fourier  | -1.4262E-04 | +1.6253E-04 | +7.5737E-04 | +1.4211E-03 |
| linear 19       | -1.4262E-04 | +1.8523E-04 | +8.0941E-04 | +1.4326E-03 |
| quad. Fourier   | -2.1960E-04 | +2.9393E-06 | +4.7064E-04 | +1.5163E-03 |
| quad. linear 19 | -2.1960E-04 | +2.1175E-05 | +5.3098E-04 | +1.5594E-03 |
| quad. linear 24 | -2.1960E-04 | +5.6997E-07 | +4.4502E-04 | +1.4777E-03 |
| quad. linear 37 | -2.1960E-04 | +6.9179E-06 | +4.5546E-04 | +1.4992E-03 |

Table 6: Error in retrieved water leaving reflectance  
for viewing at edge through Maritime aerosols.  
True value of  $\tau_a(865)$  is 0.40.

| Algorithm       | $\theta_0$  |             |             |             |
|-----------------|-------------|-------------|-------------|-------------|
|                 | 0°          | 20°         | 40°         | 60°         |
| linear Fourier  | -6.6683E-07 | -4.5914E-05 | -2.6444E-04 | +3.8958E-04 |
| linear 19       | -8.4192E-07 | -4.5866E-05 | -8.9504E-05 | -4.3686E-04 |
| quad. Fourier   | -3.7942E-05 | -9.6641E-05 | -1.6513E-04 | +3.7413E-04 |
| quad. linear 19 | -3.7942E-05 | -8.4076E-05 | -7.0274E-05 | +5.1993E-04 |
| quad. linear 24 | -3.7942E-05 | -1.0493E-04 | -1.2546E-04 | +4.6471E-04 |
| quad. linear 37 | -3.7942E-05 | -1.0111E-04 | -1.1231E-04 | +4.7841E-04 |





lookup tables will have to be regenerated many times using different assumptions in order to be prepared to deal with most of the scenarios known to exist.

Regeneration of the lookup tables is a formidable task. The individual simulations require approximately 10 minutes on the DEC 3000/400. Thus, 33,000 simulations would require approximately 5500 hours, or approximately 230 days (7.5 months). Utilizing our original four CPU's on a 24-hour basis would reduce the computation time to about 2 months. This was unacceptable for many reasons. First if the computers are being used for routine lookup table generation no other research can be carried out. Next, the lookup tables will have to be regenerated many times not just once, so the computers would rarely be available for other aspects of the algorithm development. Finally, after launch of SeaWiFS and processing of the initial data is complete, we will be required to generate the necessary new sets of tables in a very timely manner, i.e., 1-2 weeks not several months. We decided we could meet this need with two DECserver 2100 systems, one of which was procured this year (1994) and with the remaining one scheduled for 1995.

The DECserver 2100 system has four processors each of which is approximately twice as fast as the DEC 3000/400 CPU. Thus, with one DECserver 2100 a single set of lookup tables could be generated in one month. With the addition of a second DECserver 2100, the generation time would be cut to two weeks. As we plan regular CPU upgrades of the DECservers, by the launch of MODIS the speed should be considerably faster which will also allow us to respond to unforeseen events in a timely manner. Under this plan the four existing DEC 3000/400 work stations will always be available for basic algorithm studies, as will the servers, when not generating tables. The DECserver 2100's will form the backbone of the Team Member's Computing Facility to be used for post-launch MODIS products.

(iii) None.

(iv) None.

(v) None.

**f. Publications:**

K. Ding and H.R. Gordon, Atmospheric correction of ocean color sensors: Effects of earth curvature, *Applied Optics*, **33**, 7096-7016 (1994).

K. Ding and H.R. Gordon, Analysis of the influence of O<sub>2</sub> "A" band absorption on atmospheric correction of ocean color imagery, *Applied Optics* (In press).

M. Wang and H.R. Gordon, A Simple, Moderately Accurate, Atmospheric Correction Algorithm for SeaWiFS, *Remote Sensing of Environment* (In press).

## 2. Whitecap Correction Algorithm

### a. Task Objectives:

As discussed in the previous report, our objective in this period was to build a new radiometer to measure the whitecap enhanced reflectance from the sea surface. This radiometer would be mounted on a boom off the bow of a ship, directed straight down. The radiometer would record the reflectance from a spot of the order of 10 cm in diameter on the sea surface in a continuous manner, and a video camera would be bore-sighted with this radiometer to help with data interpretation. The background return from clear water would provide the whitecap-free reflectance, and the reflectance above the background would provide the average reflectance enhancement of the ocean due to whitecaps. A self-contained meteorology package would determine the speed of the ship relative to the air, a GPS unit would provide the speed of the ship, and from the two the true wind vector would be recorded. Thus the reflectance increase as a function of the wind speed would be obtained for algorithm validation. We expected to be able to complete this instrument package by the end of the calendar year.

### b. Work Accomplished:

During the past reporting period we built the whitecap radiometer and associated boom. The radiometer measured the upwelling radiance in six spectral bands (as opposed to the proposed three). These bands were spread throughout the visible from 410 nm to 860 nm (410 nm, 500 nm, 550 nm, 670 nm, 760 nm, 860 nm). This system was field tested during a three week MODIS cruise

off of Hawaii (R/V Mauna Wave, Chief Scientist Dennis Clark), and the radiometer performed very well. To convert the upwelling radiance into reflectance, downwelling irradiance was obtained with an old instrument that we had available (5 channel deck cell). This instrument did not perform as well, and needs to be updated. Because of some delays we were not able to obtain the bore-sighted video camera or meteorology station. Fortunately in all these cases redundant data was available from other cruise participants. Weather records were recorded by Dr. Stan Hooker and Mr. Jim Brown, a video camera was borrowed for short periods from Dennis Clark, and we did side by side irradiance measurements with another deck cell operated by Dennis Clark. With all of these measurements a very good initial trial data set was obtained. We are currently reducing this data, with particular attention to getting correct irradiance measurements for accurate reflectance values.

**c. Data/Analysis/Interpretation:**

During the cruise mentioned in the previous section a good data set for whitecaps was obtained. The wind was typically 20 knots almost every day, with plenty of whitecaps visible. We are currently reducing this data.

**d. Anticipated Future Actions:**

The following improvements or augmentations to the system will be performed in the next 6 month period.

1. A video system will be obtained and added to the system to allow easier data interpretation. During the sea test of the instrumentation it was obvious that this is an important addition to the system.
2. The five channel deck cell will be rebuilt to increase the data to 6 channels, and to correct some of the stability and reliability problems experienced during the field test.
3. The meteorology package will be integrated into the system.

4. The system will be field tested on cruises in which we participate.

Other actions are to work and complete the data reduction for the initial data set which we have already collected.

e. Problems/Corrective Actions: See item d above.

f. Publications:

H.R. Gordon and M. Wang, Influence of Oceanic Whitecaps on Atmospheric Correction of SeaWiFS, *Applied Optics*, 33, 7754-7763 (1994).

### 3. In-water Radiance Distribution.

a. Task Objectives:

Acquire radiance data at sea.

b. Work Accomplished:

Radiance camera is now basically complete.

c. Data/Analysis/Interpretation: None.

d. Anticipated Future Actions:

Acquire data at sea at the earliest opportunity. This will most likely be cruises scheduled by Dennis Clark in July 1995 and Fall 1995.

e. Problems/Corrective Actions: None.

f. Publications: None.

### 4. Residual Instrument Polarization.

a. Task Objectives: None.

## 5. Direct Sun Glint Correction.

a. Task Objectives: None.

## 6. Prelaunch Atmospheric Correction Validation.

a. Task Objectives:

The long-term objectives of this task are two fold. First, we need to demonstrate that our atmospheric correction scheme will work to the required accuracy. To effect this we will apply the algorithm to compute the sky radiance in the blue from measurements in the near infrared. We should be able to do this to about the same accuracy as looking downward from space. Second, we need to study the properties of aerosols over the ocean, in particular the aerosol phase function and its spectral variation, in order to verify the applicability of the aerosol models on which we are basing the atmospheric correction.

To carry out these objectives requires instrumentation for measuring the sky radiance, solar aureole, and the optical thickness of the atmosphere. Instrumentation for measuring the optical thickness and the sky radiance is available in our laboratory and has been modified to operate with the relevant MODIS spectral bands. Development of an aureole camera for use on a ship is a high priority because the sky radiance near the sun is required in aerosol optical property retrieval algorithms. Our near-term objective was to see if such inversions could be carried out without aureole data. A second objective was to develop and assemble an aureole camera system for obtaining such data at sea. The third objective is to begin to obtain a long-term time series of the aerosol properties in a maritime environment. For this we are in the process of procuring a CIMEL sun/sky radiometer that can be operated in a remote environment and send data back to the laboratory via a satellite link. These are similar to the radiometers used by B. Holben and Y. Kaufman.

**b. Work Accomplished:**

We planned and executed a field trip to Key West, FL in April (1994) to obtain sky radiance and other aerosol data. Key West is a small island and was chosen to simulate as much as possible measurements made from a ship, i.e., to reduce the perturbation by the land as much as possible. The planned measurements included (1) aerosol optical thickness as a function of wavelength in nine bands from 380 to 1026 nm, (2) sky radiance using the full-sky camera at 560, 671, and 860 nm, and (3) sky radiance at selected positions using a hand-held radiometer at 558, 669, and 866 nm. We began analysis of the Key West data; however, for the only day with a clear enough sky, the data were obtained at such a small solar zenith angle that inversion is only accurate for the forward part of the phase function. Our present inversions yield a value of single scatter albedo that was far too low. We are trying to track down the source of the difficulty; however, we believe that the error results from the absence of solar aureole data.

The aureole camera system has now been designed and assembled. The idea is fairly simple, a cooled CCD camera has been outfitted with a lens focused at infinity, an interference filter which selects the spectral band of interest, and a small aperture over this filter. A neutral density occulter is placed approximately 1 meter from the aperture, and this occulter is positioned to block the direct sunlight from entering the camera system. In this manner the sky radiance close to the sun can be measured, without the direct sunlight (approximately 6 orders of magnitude larger) interfering with the measurement. We are currently doing the characterization of the camera system electronics and optics. This is part of the calibration procedure. During the next reporting period we will also be assembling the field data acquisition software package. Our goal is to field test this system during a short cruise in July.

The CIMEL Electronique, Automatic Sun Tracking Photometer, a Vitel Inc. GOES Data Transmitter with accessories, and a set of Solar Power Panels are now on order.

**c. Data/Analysis/Interpretation:** Nothing concrete yet.

**d. Anticipated Future Actions:**

During the next reporting period we will be working on characterizing the camera system, and finalizing the data acquisition software. We had also expected to participate on a short cruise off of Hawaii during February on which we could have tested this system at sea and acquired a more complete sky radiance data set. The cruise track for this cruise was optimal for us as it was planned to stay in the lee of Lanai, an area where cloud free skies are probable. Due to the slip in the SeaWiFS launch, this cruise has now been rescheduled for July.

We also expect to take delivery of the CIMEL Electronique, Automatic Sun Tracking Photometer and assemble to radiometer with the GOES Data Transmitter and Solar Power Panels. Testing will begin after assembly with the goal of deploying the instrument in the field in the first six months of 1995.

e. Problems/Corrective Actions: None.

f. Publications: None.

## 7. Detached Coccolith Algorithm and Post Launch Studies.

### a. Task Objectives:

The algorithm for retrieval of the detached coccolith concentration from the coccolithophorid, *E. huxleyi* is described in detail in our ATBD. The key is quantification of the backscattering coefficient of the detached coccoliths. Our earlier studies showed that calcite-specific backscatter coefficient was less variable than coccolith-specific backscatter coefficient, and this would be more scientifically meaningful for future science that will be performed with this algorithm. The variance of the calcite-specific backscatter has been analyzed for only a few species, thus, we need to examine this in other laboratory cultures and field samples. There is also a relationship between the rate of growth of the calcifying algae and the rate of production and detachment of the coccoliths which needs to be further quantified. With this in mind, the objectives of our coccolith studies are, under conditions of controlled growth of coccolithophores (using chemostats), to define the effect of growth rate on:

- the rate that coccoliths detach from cells (which also is a function of turbulence and physical shear);
- the rates of coccolith production;
- the morphology of coccoliths; and
- the volume scattering and backscatter of coccoliths.

The last aspect of these studies will be to perform shipboard measurements of suspended calcite and estimate its optical backscatter as validation of the laboratory measurements. A thorough understanding of these growth-related properties will provide the basis for a generic suspended calcite algorithm. As with algorithms for chlorophyll, and primary productivity, the natural variance between growth related parameters and optical properties needs to be understood before the accuracy of the algorithm can be determined.

**b. Work Accomplished:**

In the last 6 months, we have performed experiments on the effect of turbulence on the rate of detachment of coccoliths. These studies were performed under highly controlled conditions of turbulent dissipation rates. The rationale for this work was that in order to grow these organisms, they must be stirred and since one of our goals is to relate coccolith detachment to growth rate, we must insure that we understand the independent effects of turbulence on detachment.

For the studies of coccolith morphology, we have recently modified our microscope system with a phase contrast optical system which gives us much more resolution than we have ever had. This will save us considerable time in estimating numbers and morphologies of coccoliths because before, we needed to use a scanning electron microscope and make measurements on dead specimens. Now, we can count coccoliths and check morphology on living specimens using light microscopy (which is essentially instantaneous). In fact, we can actually count the numbers of these 2 micrometer diameter plates on individual cells.



Successful algorithm development also requires sea-truth data. We continued our analyses of optical data from a coccolithophore bloom in the North Atlantic. These data include volume scatter measurements, absorption measurements, pigment measurements, cell counts, suspended calcite measurements and particulate organic carbon and nitrogen measurements. The first paper on this material has been submitted for publication.

### c. Data/Analysis/Interpretation:

Our results from the laboratory experiments showed that when the cells are actively growing, coccolith detachment is not a function of turbulence. However, when cell growth slows or stops, then plates are held more loosely such that turbulence and coccolith detachment are directly related. This represents the first physiological study directly relating turbulence to detachment of coccoliths.

In regards to our work-up of scatter and absorption data from a coccolithophore bloom in the north Atlantic, we have found that chlorophyll-specific absorption by field populations of *E. huxleyi* was similar to previously reported laboratory culture measurements of the same species. Volume scatter measurements showed that the suspended coccoliths were responsible for about 80% of the total backscatter,  $b_b$ , in the center of the bloom. Vertical profiles of backscatter showed that greatest calcite-dependent light scatter was observed just below the base of the mixed layer. Areal maps of calcite-dependent backscatter and reflectance (calculated from absorption and backscatter) were extremely similar, due to the dominance of backscatter over absorption. Calculated reflectance in this mesoscale feature reached as high as 21% at 440 nm and 24% at 550 nm, slightly less than what has been observed previously in Gulf of Maine blooms. Total scatter,  $b$ , was also calculated as the difference between beam attenuation and absorption. The ratio of backscatter to total scatter  $\bar{b}_b \equiv b_b/b$  was about 0.01-0.02 at 440 nm and 550 nm for  $b$  values of 1 to 3  $\text{m}^{-1}$ . As total scatter decreased from 1  $\text{m}^{-1}$ ,  $\bar{b}_b$  increased. The behavior of  $\bar{b}_b$  is compared for coccolith-dominated versus chlorophyll-dominated waters. Vertical profiles of calcite-dependent scatter, combined with satellite remote sensing data, were used to assess the vertical transport velocity of coccoliths (1-2 m per day). This velocity was an order of magnitude greater than that expected from theoretical Stokes sinking calculations and previous sinking rate experiments. A number of hypotheses are proposed

to explain the the discrepancy; the most likely of which is that the subsurface peak in calcite-dependent scatter did not result from detached coccoliths sinking but resulted either from plated coccolithophores sinking, then detaching their plates, or from deep coccolithophores producing and detaching their plates in situ.

**d. Anticipated Future Actions:**

Given the completion of our turbulence experiments, we can now begin the chemostat experiments in which we will measure the light scatter properties of coccolithophores as a function of growth rate. These experiments should start in mid-February.

There is still more analysis to be done on the field coccolithophore data from the North Atlantic. There is sufficient material to publish a second paper on the relationship between backscatter, suspended calcite concentration, and reflectance. This will be written for *Limnology and Oceanography*.

**e. Problems/Corrective Actions: None**

**f. Publications: None**

**8. Other Developments.**

The PI spent a significant portion of the first quarter of this reporting period completing the necessary requests to obtain government permission to procure several items of capital equipment. Also, all personnel on the project devoted most of their effort in late September and October toward revising the Algorithm Theoretical Basis Document (ATBD) for normalized water leaving radiance. Version 2 of the ATBD's for Normalized water-leaving radiance (along with aerosol products) and detached coccoliths were delivered to M. King on November 2, 1994.

The SeaWiFS/MODIS algorithm for estimating the aerosol optical thickness for has now been coded and will be delivered to R. Evans in January for incorporation into the processing system.

A method for combining high-altitude aircraft radiance (upwelling) and surface radiance (downwelling) for determination of the columnar aerosol optical properties has been developed. A paper

on the subject is nearly complete and will be submitted to *Applied Optics* in January. This could provide a powerful method of studying aerosol properties over the ocean. Also, a second study concerning the perturbation of the sky radiance measurements made from islands, caused by the presence of the island itself, has been carried out and a paper is in preparation. Both of these have relevance to the "Prelaunch Atmospheric Correction Validation" (Topic 6 above) portion of our research, as well as to the validation of retrieved aerosol properties over the oceans from EOS sensors.

## 9. References.

- [1] P. Y. Deschamps, M. Herman and D. Tanre, "Modeling of the atmospheric effects and its application to the remote sensing of ocean color," *Applied Optics* **22**, 3751-3758 (1983).
- [2] H. R. Gordon, D. K. Clark, J. W. Brown, O. B. Brown, R. H. Evans and W. W. Broenkow, "Phytoplankton pigment concentrations in the Middle Atlantic Bight: comparison between ship determinations and Coastal Zone Color Scanner estimates," *Applied Optics* **22**, 20-36 (1983).
- [3] M. Wang and H. R. Gordon, "Influence of Oceanic Whitecaps on Atmospheric Correction of SeaWiFS," *Applied Optics* **33**, 7754-7763 (1994).
- [4] H. R. Gordon and D. J. Castaño, "The Coastal Zone Color Scanner Atmospheric Correction Algorithm: Influence of El Chichón," *Applied Optics* **27**, 3319-3321 (1988).
- [5] E. P. Shettle and R. W. Fenn, *Models for the Aerosols of the Lower Atmosphere and the Effects of Humidity Variations on Their Optical Properties* (Air Force Geophysics Laboratory, Hanscomb AFB, MA 01731, AFGL-TR-79-0214, 1979).
- [6] H. R. Gordon and M. Wang, "Retrieval of water-leaving radiance and aerosol optical thickness over the oceans with SeaWiFS: A preliminary algorithm," *Applied Optics* **33**, 443-452 (1994).

- [7] WCP-112, *A preliminary cloudless standard atmosphere for radiation computation* (World Meteorological Organization, WMO/TD-No. 24, Geneva, 1986).
  
- [8] M. D. King, Harshvardhan and A. Arking, "A Model of the Radiative Properties of the El Chichón Stratospheric Aerosol Layer," *Journal of Climate and Applied Meteorology* **23**, 1121-1137 (1984).
  
- [9] C. Cox and W. Munk, "Measurements of the Roughness of the Sea Surface from Photographs of the Sun's Glitter," *Jour. Opt. Soc. of Am.* **44**, 838-850 (1954).
  
- [10] H. R. Gordon and M. Wang, "Surface Roughness Considerations for Atmospheric Correction of Ocean Color Sensors. 1: The Rayleigh Scattering Component," *Applied Optics* **31**, 4247-4260 (1992).

**Appendix 1.**

**Analysis of the Influence of O<sub>2</sub> "A" band absorption  
on atmospheric correction of ocean color imagery**

by

Kuiyuan Ding and Howard R. Gordon

(In press in *Applied Optics*)

**Acknowledgement**

We are grateful to the National Aeronautics and Space Administration for support under Grant NAGW-273 and Contracts NAS5-31363 and NAS5-31743.

## Abstract

Two satellite borne ocean color sensors scheduled for launch in the mid 1990's each have a spectral band (nominally 745-785 nm) that completely encompasses the O<sub>2</sub> A band at 762 nm. These spectral bands are to be used in atmospheric correction of the color imagery by assessing the aerosol contribution to the total radiance at the sensor. The effect of the O<sub>2</sub> band on the radiance measured at the satellite is studied using a line-by-line backward Monte Carlo radiative transfer code. As expected, if the O<sub>2</sub> absorption is ignored, unacceptably large errors in the atmospheric correction result. The effects of the absorption depend on the vertical profile of the aerosol. By assuming an aerosol profile — the base profile — we show that it is possible to remove most of the O<sub>2</sub> absorption effects from atmospheric correction in a simple manner. We also investigate the sensitivity of the results to the details of the assumed base profile and find that, with the exception of situations in which there are significant quantities of aerosol in the stratosphere, e.g., following volcanic eruptions or in the presence of thin cirrus clouds, the quality of the atmospheric correction depends only weakly on the base profile. Situations with high concentrations of stratospheric aerosol require additional information regarding vertical structure to utilize this spectral band in atmospheric correction; however, it should be possible to infer the presence of such aerosol by a failure of the atmospheric correction to produce acceptable water-leaving radiance in the red. An important feature of our method for removal of the O<sub>2</sub> absorption effects is that it allows the use of lookup tables that can be prepared in the absence of O<sub>2</sub> absorption using more efficient radiative transfer codes.

## Introduction

The radiance  $L_w$  exiting the ocean in the visible carries information concerning the concentration of phytoplankton in near-surface waters. Phytoplankton are microscopic plants that through photosynthesis, i.e., they combine  $\text{CO}_2$  (dissolved in the water) and water to produce carbohydrates, form the first link in the marine food chain. Their influence on the  $\text{CO}_2$  makes knowledge of their spatial and temporal variability important in the global carbon cycle. The Coastal Zone Color Scanner<sup>1</sup> (CZCS) launched by NASA on Nimbus 7 in the fall of 1978 (and operational until mid 1986) acquired imagery over the oceans in four spectral bands centered at 443, 520, 550, and 670 nm, with spectral widths of approximately 20 nm. Gordon et al.<sup>2</sup> showed that the phytoplankton pigment concentration,  $C$  — the sum of the concentrations of chlorophyll  $a$  and its degradation product phaeophyton  $a$  — could be derived from this imagery after removing the effects of the atmosphere. The CZCS spectral bands were located in atmospheric "windows," so the atmospheric effects were due almost entirely to scattering by molecules (Rayleigh scattering) and by aerosols. Except for a small variation due to changes in atmospheric surface pressure, the Rayleigh scattering contribution can be computed exactly.<sup>3</sup> In contrast, the aerosol scattering is highly variable in space and time and must be determined from the imagery itself. This was effected by utilizing the band at 670 nm, where  $L_w$  is very small so the top of the atmosphere (TOA) radiance is due to the atmosphere, to assess the aerosol's contribution there. The spectral variation was then estimated by either using regions in the imagery where  $C \lesssim 0.25 \text{ mg/m}^3$  (clear water regions<sup>4</sup> for which  $L_w$  is known in the green bands as well as the red band) or by assigning a nominal spectral variation<sup>5,6</sup> based on experience and on the properties of maritime aerosols. However, each procedure required assumptions, preventing a totally deterministic correction.

With the success of the CZCS as a proof-of-concept mission several ocean color instruments are being prepared for launch: the sea-viewing wide-field-of-view sensor (SeaWiFS);<sup>7</sup> the moderate resolution imaging spectroradiometer (MODIS);<sup>8</sup> and the ocean color and temperature sensor (OCTS) on the advanced earth observation satellite (ADEOS) to be launched by Japan. To provide better atmospheric correction, these instruments have spectral bands in the near infrared NIR, where the ocean can be considered to be a Fresnel-reflecting medium that absorbs all photons penetrating

the surface. In the case of SeaWiFS and OCTS, the NIR bands are 40 nm wide and positioned at 765 and 865 nm in windows free of water vapor absorption. The rather large spectral widths were governed by the requirement for high signal-to-noise ratios. Thus, the 765 nm band on both sensors was forced to completely encompass the O<sub>2</sub> “A” absorption band at 762 nm. It was believed that correction for the ~ 10% absorption due to the O<sub>2</sub> “A” band would be possible. We have developed an approach to the correction of the 765 nm bands for both SeaWiFS and OCTS for O<sub>2</sub> absorption and report such in this paper.

We begin with a brief review of the proposed<sup>9</sup> atmospheric correction algorithm for SeaWiFS which utilizes the 765 nm band, and which ignores the presence of the O<sub>2</sub> absorption, i.e., was developed assuming the O<sub>2</sub> absorption feature in the 765 nm band did not exist. Next, through a series of Monte Carlo simulations, we examine the influence of the O<sub>2</sub> absorption on radiative transfer in the atmosphere. Based on these simulations a method for assessing and removing the O<sub>2</sub> effect is developed. Finally, we present examples of the performance of the end-to-end SeaWiFS atmospheric correction algorithm in the presence of the O<sub>2</sub> absorption.

### The proposed SeaWiFS correction algorithm

In a recent paper, Gordon and Wang<sup>9</sup> proposed an algorithm for the atmospheric correction of SeaWiFS, and ultimately, MODIS. Briefly, the total radiance  $L_t(\lambda)$  measured at the top of the atmosphere at a wavelength  $\lambda$  can be decomposed as follows:

$$L_t(\lambda) = L_r(\lambda) + L_a(\lambda) + L_{ra}(\lambda) + t(\theta_v, \lambda)L_w(\lambda), \quad (1)$$

where  $L_r(\lambda)$  is the radiance resulting from multiple scattering by air molecules (Rayleigh scattering) in the absence of aerosols,  $L_a(\lambda)$  is the radiance resulting from multiple scattering by aerosols in the absence of the air, and  $L_{ra}(\lambda)$  is the interaction term between molecular and aerosol scattering.<sup>10</sup> In this equation,  $t$  is the diffuse transmittance of the atmosphere along the viewing direction specified by  $\theta_v$ , the angle between the normal to the sea surface and the sensor.<sup>11</sup> Radiance arising from specular reflection of direct sunlight from the sea surface and subsequent propagation to the top of the atmosphere without scattering (sun glitter) has been ignored because SeaWiFS can be tilted away from the glitter pattern. However, specular reflection of skylight, created by both molecular



and aerosol scattering, is included in  $L_r$ ,  $L_a$ , and  $L_{ra}$ . The influence of whitecaps has been ignored under the assumption that their contribution can be estimated from an estimate of the surface wind speed.<sup>12</sup>

The goal of the atmospheric correction is the retrieval of  $L_w$  from  $L_t$ . It is convenient to convert radiance ( $L$ ) to a reflectance ( $\rho$ ) defined to be  $\pi L / F_0 \cos \theta_0$ , where  $F_0$  is the extraterrestrial solar irradiance, and  $\theta_0$  is the solar zenith angle. With this definition, Eq. (1) becomes

$$\rho_t(\lambda) = \rho_r(\lambda) + \rho_a(\lambda) + \rho_{ra}(\lambda) + t(\theta_v, \lambda)\rho_w(\lambda). \quad (2)$$

The reason for the particular decomposition in Eqs. (1) and (2) is that  $\rho_r$  can be computed exactly given the surface atmospheric pressure and  $\lambda$ .<sup>3</sup>

After computation of  $\rho_r$ , the algorithm utilizes  $\rho_t - \rho_r = \rho_a + \rho_{ra}$  in the near infrared (NIR) at 765 and 865 nm, where  $\rho_w$  can be taken to be zero except in turbid coastal waters or possibly intense open-ocean coccolithophore blooms,<sup>13</sup> to choose two aerosol models from a set of candidate models. The candidate models were taken from those proposed by Shettle and Fenn.<sup>14</sup> The chosen aerosol models are then used to predict  $\rho_a + \rho_{ra}$  in the visible which, when combined with  $\rho_r$  there, yields the desired  $t\rho_w$ . To assess the efficacy of the algorithm, simulations of  $\rho_t$  using aerosol models which were similar, but not identical, to the candidate aerosols models, were carried out. The simulated  $\rho_t$  was then used as pseudo data for insertion into the correction algorithm. The error  $\Delta\rho$  in the retrieval of  $t\rho_w$  at 443 nm was nearly always found to be  $\lesssim 0.002$  and often  $\lesssim 0.001$ . This error meets the SeaWiFS goal of retrieving  $L_w$  (or  $\rho_w$ ) at 443 nm to within  $\sim \pm 5\%$  in waters with low phytoplankton pigment concentrations, e.g., the Sargasso Sea in summer.

The algorithm as described ignores the presence of the  $O_2$ , i.e., in the simulations of  $\rho_t$  and  $\rho_r$  the model atmospheres were free of the  $O_2$  absorption in the 765 nm band. In the presence of  $O_2$  absorption  $\rho_t$  will be smaller in the 765 nm band than in its absence, so the computed value of  $\rho_a + \rho_{ra}$  at 765 nm will be smaller. Operation of the present correction algorithm in the presence of the  $O_2$  absorption with the smaller value of  $\rho_a + \rho_{ra}$  will lead to the choice of an inappropriate model with which to determine  $\rho_a + \rho_{ra}$  in the visible.

Our approach to dealing with the effects of the  $O_2$  absorption in the 765 nm band is to use the value of  $\rho_a + \rho_{ra}$  derived in the presence of the  $O_2$  absorption to determine the value it would have were the  $O_2$  absorption absent. The simulations presented below suggest that such an approach is viable.

### Radiative transfer in the $O_2$ A band

In this section we describe the technique used to study the radiative transfer in the  $O_2$  A band. What we wish to learn is the influence of the  $O_2$  absorption on the reflectance  $\rho_t$  leaving the TOA in a band extending from 745 to 785 nm. Specifically, since the proposed SeaWiFS algorithm ignores the  $O_2$  absorption, our goal is to be able to estimate what  $\rho_a + \rho_{ra}$  would be in the absence of the absorption band.

#### A. The $O_2$ A band.

The  $O_2$  A band extends from about 759 to 770 nm. There are 286 individual absorption lines having appreciable line strengths. Figure 1 shows a sample of the sea-level absorption coefficient as a function of wave number,  $\nu = 1/\lambda$ , computed from the positions, line strengths, and line widths of the individual absorption lines (assuming a Lorentz shape) taken from the AFGL compilation.<sup>15</sup> Note that this figure covers only about 1.165 nm but contains 12 spectral lines, and the absorption coefficient varies from approximately  $30 \text{ km}^{-1}$  to about  $0.2 \text{ km}^{-1}$  over a small fraction of a nm. Because of the strong variation of the absorption coefficient with wavelength, the absorption over a band containing several lines will not be an exponential function of the path length. Thus, it is not possible to assign a single mean absorption coefficient to the entire  $O_2$  A band. Furthermore, since the individual spectral lines are pressure and temperature broadened, even at discrete wavelengths, i.e., bands with width  $\ll$  the width of the individual spectral lines, the absorption coefficient will be dependent on altitude in the atmosphere. Thus, a complete treatment of the radiative transfer in this absorption band requires an atmosphere consisting of several layers in which the absorption coefficient is a very strong function of frequency.

## B. Preliminary discussion of the O<sub>2</sub> effect.

It is possible to understand qualitatively the effect of the O<sub>2</sub> A band on the radiance exiting the top of the atmosphere by examining single scattering. First, we assume that the atmosphere is free of aerosols, i.e., we only have Rayleigh scattering and the scattering coefficient will vary with altitude in proportion to the density in the same manner as the O<sub>2</sub> abundance. For a given viewing geometry we define the air mass  $M$  as

$$M = \frac{1}{\cos \theta_v} + \frac{1}{\cos \theta_0},$$

where  $\theta_0$  is the solar zenith angle and  $\theta_v$  is the viewing angle, i.e., the angle between the surface normal and the direction of propagation of the radiance exiting the TOA. Photons scattering from molecules at any altitude will have traversed a path of length proportional to  $M$  upon exiting the atmosphere. Thus, we expect the *decrease* in radiance exiting the atmosphere to be a function of  $M$ ; albeit *not* an exponential function. In the case of multiple scattering the path of the photon is no longer proportional to  $M$  so a similar argument does not apply; however, since the Rayleigh scattering optical thickness is small ( $\sim 0.025$ ) at 765 nm, multiple Rayleigh scattering will be small and the radiance decrease will still depend on  $M$  in much the same manner as for single scattering.

The addition of aerosols causes two complications: the aerosol concentration is a strong and variable function of altitude; and the aerosol concentration is usually sufficiently high that multiple scattering is significant. The influence of the vertical profile of the aerosol concentration is easy to understand in the single scattering approximation. Typically, over the oceans most of the aerosol is in the marine boundary layer which is 1-2 km thick. The aerosol component of the TOA radiance at 765 nm with a high concentration of aerosol in the boundary layer will be significantly larger than the molecular-scattering component. This radiance will have had to travel through most of the atmosphere (twice) before reaching the TOA. The total path is proportional to  $M$ , so we expect that the radiance decrease will be larger than that for an aerosol-free atmosphere (because more photons backscattered to the TOA will have had to travel farther in the atmosphere), and that it will be a function of the airmass. In contrast, if there is a high concentration of aerosol in the stratosphere, e.g., following a major volcanic eruption, a fraction of the TOA radiance will

have scattered from the stratosphere and not have traveled through a significant portion of the atmosphere. Then, for the same aerosol concentration as in the marine boundary layer example, the fractional decrease in the radiance due to the  $O_2$  absorption will be less.

In general the aerosol will be distributed continuously throughout the atmosphere. A typical profile will display a high concentration in the boundary layer, a rapid decrease in the free troposphere and slower decrease in the background stratosphere, and occasionally an increase (sometimes large) due to recent (e.g., the past 1–3 years) volcanic activity.<sup>16</sup> Thus, to simulate the fractional decrease in the TOA radiance near 765 nm due to the  $O_2$  A band absorption requires an atmosphere composed of enough layers to adequately represent the vertical distribution of the aerosol.

### C. The radiative transfer code and model.

The radiative transfer code we developed for this study is a backward Monte Carlo for a plane parallel atmosphere. Polarization of the light field is ignored. The backward procedure is used because it provides a significant increase in accuracy (over the forward Monte Carlo), for a given expense in computational time, when the radiance is desired in only a single viewing direction. In this kind of simulation, photons are ejected from the detector and followed to the sun. Actually, at each interaction in the atmosphere the probability that the photon will be scattered to the TOA in the direction of the sun is computed and used as the estimator. The atmosphere is bounded by the sea, which we model as a Fresnel reflecting surface that absorbs all photons that are transmitted through it. This is realistic because of the large absorption coefficient of liquid water in the NIR. The possibility that at any interaction a photon could be scattered toward the sea surface and be Fresnel-reflected back to the TOA is included in the Monte Carlo estimator. The code includes provision for the sea surface to be roughened by the wind with surface slopes obeying the Cox and Munk<sup>17</sup> distribution; however, in all of the simulations presented here the surface was smooth.

For our model atmosphere we assumed that the density and temperature follow the U.S. 1976 Standard Atmosphere.<sup>18</sup>  $O_2$  is distributed in proportion to the atmospheric density. The individual  $O_2$  spectral lines are assumed to have a Lorentz line shape. The line strengths and line widths

(at NTP) were taken from the AFGL<sup>15</sup> compilation, and the line width varies with altitude in proportion to  $P/\sqrt{T}$ , where  $P$  is the pressure and  $T$  is the absolute temperature. The full width at half maximum (FWHM) at the sea surface of a typical absorption line in the A band is of the order of  $0.1 \text{ cm}^{-1}$  or  $\sim 0.006 \text{ nm}$  (Figure 1). The atmosphere is composed of thirty-seven homogeneous layers. For each layer the  $\text{O}_2$  absorption coefficient as a function of wave number  $\nu$  was computed and tabulated at  $10^5$  values of  $\nu$  between  $\nu = 13,422.82 \text{ cm}^{-1}$  ( $\lambda = 745 \text{ nm}$ ) and  $12,738.85 \text{ cm}^{-1}$  ( $\lambda = 785 \text{ nm}$ ). With this resolution, there are approximately 15 tabulated values within the FWHM of each absorption line at the surface. Linear interpolation is used for values of  $\nu$  between tabulated values.

For a realistic treatment of the aerosol in the code, we further divide the atmosphere into four broad regions (Figure 2): (1) the marine boundary layer from the surface to 2 km, where the aerosol concentration is independent of altitude; (2) the free troposphere, where the aerosol concentrations varies in proportion to  $\exp[-z/h]$ , where  $z$  is the altitude (2-12 km) and  $h$  (called the scale height) is 2 km; (3) the background stratosphere (12-30 km), where the aerosol concentration is also exponential with a scale height of 5 km; and (4) a volcanic region (18-20 km) within the stratosphere that can contain a uniformly mixed volcanic aerosol. The optical properties of each of the four regions can be characterized by individual aerosol models, and any of the regions can be free of aerosols if desired. There is no aerosol above 30 km.

As in Ref. 9, the aerosol models used for the two lower regions were taken from Shettle and Fenn.<sup>14</sup> Based on size distribution and composition measurements, they developed two models called the Tropospheric (to model the aerosol in the free troposphere — few large particles) and Oceanic (to model the aerosol produced by sea spray — few small particles). They combined these to form the Maritime model to represent the aerosol in the marine boundary layer. In terms of total aerosol number per unit volume, the Maritime model consists of 99% Tropospheric and 1% Oceanic. Gordon and Wang<sup>9</sup> added a Coastal model (99.5% Tropospheric and 0.5% Oceanic) to provide a description of the aerosol that might be more representative of the boundary layer near the coast.

For the upper two regions we use a model for the background stratosphere from the WMO<sup>19</sup> and a model for the volcanic aerosol from King et al.<sup>20</sup> Both models assume a 75% solution of  $\text{H}_2\text{SO}_4$ . We have also included a volcanic ash model<sup>19</sup> to represent fresh volcanic aerosol. The size distributions in these regions are modified gamma distributions.

With all of the optical properties of the atmosphere prescribed, the Monte Carlo code operates as follows. A photon is ejected from the receiver in a direction opposite to the observation direction with a wave number  $\nu$  chosen from a uniform probability density over  $12,738.82 \leq \nu \leq 13,422.82 \text{ cm}^{-1}$ . This choice of  $\nu$  corresponds to assuming the extraterrestrial solar irradiance is constant over the this spectral interval, i.e.,  $F_0$  is replaced by its spectral band-averaged value. This is a convenience rather than a necessity. The Rayleigh optical extinction coefficient is then computed for  $\nu$  based on Fenn et al.<sup>16</sup> The aerosol extinction coefficient for each layer is provided by the aerosol model and concentration. It is assumed to be independent of  $\lambda$  over the 745–785 nm band. The optical distance (defined as  $\int c(l) dl$ , where  $c(l)$  is the extinction coefficient along the path  $l$ ) the photon travels is then determined from an exponential probability density function. From the tabulated values of the absorption and scattering coefficients, the physical distance that this corresponds to is determined, yielding the position of the first interaction point. The various estimators are computed, the photon allowed to scatter, and the process is repeated. In a typical computer run we trace the histories of  $10^7$  photons. This implies that there are approximately 1,300 photons sampling the FWHM of each individual  $\text{O}_2$  absorption line at the sea surface.

#### D. Tests of the radiative transfer code.

Validation of the radiative transfer code was effected in two ways. In the absence of the  $\text{O}_2$  absorption, the code was compared to the output of a successive order of scattering code similar to that used by Gordon and Wang.<sup>9</sup> In this case,  $\nu$  was not sampled, the molecular scattering was distributed uniformly from the surface to 100 km ( $\tau_r = 0.0255$ ), and the aerosol scattering was uniformly distributed from the surface to 30 km ( $\tau_a = 0.2$ ). The difference in the radiances computed by the two codes was usually  $\lesssim 0.1\%$ . This suggests that when the  $\text{O}_2$  absorption features of the code are not employed, it is capable of returning radiances accurate to within 0.1%.

It is difficult to test completely the code's handling of the O<sub>2</sub> absorption band, because, in contrast to the situation in the previous paragraph, we do not have a second, highly accurate code for comparison. However, the LOWTRAN<sup>21</sup> atmospheric propagation code, which treats band absorption well, does have an approximate multiple scattering capability for calculating radiance reflected from the earth-atmosphere system.<sup>22</sup> If aerosol scattering is omitted, at 765 nm multiple scattering effects should be small enough so that LOWTRAN can compute the radiance. Since LOWTRAN does not have the provision for a Fresnel-reflecting sea surface, we ran both codes with a totally absorbing lower boundary. The differences in the radiances ( $L_r$ ) over the spectral band  $12,735 \leq \nu \leq 13,425 \text{ cm}^{-1}$  between LOWTRAN and our code were  $\sim 1\%$ . Since our code treats both multiple scattering and gas absorption in a more precise manner than LOWTRAN, we believe this demonstrates that our code is satisfactory.

Finally, since the Lorentz line shape underestimates the absorption in the core of the lines and overestimates the absorption in the wings in the upper atmosphere ( $z \gtrsim 10 \text{ km}$ ), we carried out a series of simulations using the Voigt<sup>23</sup> line shape to describe the O<sub>2</sub> absorption. For an aerosol-free atmosphere, the two line shapes yielded reflectances within the inherent error of the Monte Carlo procedure ( $\sim 0.1\%$ ). The Lorentz line shape was used in the computations reported here.

### Removal of O<sub>2</sub> A band absorption

In this section we develop the necessary relationships for removing the effects of the O<sub>2</sub> A band absorption from the 765 nm band. We shall use the notation that primes represent quantities computed or measured when the O<sub>2</sub> absorption band is *present* (*prime and present* both begin with "p"), and unprimed quantities represent those in the *absence* of the O<sub>2</sub> absorption. Thus Eq. (2) becomes

$$\begin{aligned}\rho_t - \rho_r &= \rho_a + \rho_{ra} \equiv \rho_A, \\ \rho'_t - \rho'_r &= \rho'_a + \rho'_{ra} \equiv \rho'_A,\end{aligned}\tag{3}$$

where we have explicitly used the fact that  $\rho_w$  is taken to be zero. The known quantities in these equations are  $\rho'_t$  (measured) and  $\rho_r$ . The SeaWiFS correction algorithm<sup>9</sup> will employ precomputed lookup tables of  $\rho_r$  at standard atmospheric pressure, and  $\rho_A$  for a variety of aerosol models and optical thicknesses. As the notation suggests, these tables for the 765 nm SeaWiFS band have been

computed assuming that the  $O_2$  absorption band does not exist. Thus, we need to find  $\rho_A$  from  $\rho'_t$  and  $\rho_r$ .

Our technique involves three steps: (1) finding  $\rho'_r$  from an empirical relationship between  $\rho'_t$  and  $\rho_r$  developed from simulations; (2) using the second equation in Eq. (3) to deduce  $\rho'_A$ ; and (3) finding  $\rho_A$  from an empirical relationship between  $\rho'_A$  and  $\rho_A$  developed from simulations. The desired  $\rho_A$  is then used in the atmospheric correction algorithm. A desirable feature of this  $O_2$  correction is that both sets of  $O_2$ -free lookup tables can still be employed. This is important because of the intense computational burden required for computing accurate reflectances in the presence of the  $O_2$  absorption. In this section the empirical relationships we have mentioned above are developed.

#### A. Relationship between $\rho_r$ and $\rho'_r$ .

As described in an earlier section, we expect that the fractional decrease in the reflectance of the atmosphere-ocean system in the 745–785 nm spectral band due to the  $O_2$  absorption will be a function of the two-way air mass  $M$ . Thus, we carried out a series of Monte Carlo simulations for an aerosol-free atmosphere using a variety of solar zenith and viewing angles. Both  $\rho_r$  and  $\rho'_r$  are computed, from which we found the fractional change in reflectance,  $(\rho_r - \rho'_r)/\rho'_r$ , as a function of  $M$ . The results are provided in Figure 3. Note that the minimum air mass is 2, and for this the  $O_2$  absorption results in a decrease in the reflected radiance by approximately 7%. Typical viewing geometries have  $2 \leq M \lesssim 5$ , so the decrease in reflectance will vary between  $\sim 7$  and  $\sim 11\%$ . The dotted line in Figure 3 is a least-squares fit of the computations to the air mass, i.e.,

$$\log_{10} \left( \frac{\rho_r - \rho'_r}{\rho'_r} \right) = a_{r0} + a_{r1}M + a_{r2}M^2 \equiv P_r(M),$$

where the  $a_{r0}$ ,  $a_{r1}$ , and  $a_{r2}$  are  $-1.3491$ ,  $+0.1155$ , and  $-7.0218 \times 10^{-3}$ , respectively. Using this fit, the desired  $\rho'_r$  for any  $M$  can be estimated from

$$\rho'_r = \left( 1 + 10^{P_r(M)} \right)^{-1} \rho_r. \quad (4)$$



Figure 4 provides the error (%) in the estimated value of  $\rho'_r$ , using Eq. (4), for the simulations in Figure 3. It suggests that  $\rho'_r$ , the reflectance when the  $O_2$  absorption is present, can be estimated from  $\rho_r$ , the reflectance in the absence of the  $O_2$  absorption, to within  $\sim \pm 0.2\%$  solely from the sun-viewing geometry.

#### B. Relationship between $\rho_A$ and $\rho'_A$ .

Now we develop a relationship between  $\rho_A$  and  $\rho'_A$ . We proceed in the same manner as with the Rayleigh component, i.e., we carry out a series of Monte Carlo simulations for an atmosphere including *both* aerosol and molecular scattering; however, there is an inherent difficulty in that the relationship cannot be independent of the vertical structure of the aerosol. Therefore, the estimate of  $\rho_A$  from  $\rho'_A$  will be less accurate than the estimation of  $\rho'_r$  from  $\rho_r$ . Clearly, we must choose an aerosol profile, on which to base the relationship, that is as representative as possible. We call this the “base” profile.

To assess the magnitude of the error in the relationship when an unrepresentative base profile is chosen, we begin with a very simple base profile and find the error in the prediction of  $\rho_A$  from  $\rho'_A$ . For this purpose, the base profile will consist of a uniformly mixed aerosol in the boundary layer (thickness of 2 km), with the free troposphere and stratosphere being free of aerosols. Thus all of the aerosol is in the marine boundary layer. The base aerosol optical thickness  $\tau_a$  is taken to be 0.2693 and the aerosol model is the Shettle and Fenn<sup>14</sup> Maritime model at 50% relative humidity (M50). Figure 5 provides  $(\rho_A - \rho'_A)/\rho'_A$  as a function of  $M$  for a series of simulations using this base aerosol. As in the case of a pure Rayleigh scattering atmosphere, the line in Figure 5 is a least-squares fit of the computations to the air mass, i.e.,

$$\log_{10} \left( \frac{\rho_A - \rho'_A}{\rho'_A} \right) = a_{A0} + a_{A1} M + a_{A2} M^2 \equiv P_A(M), \quad (5)$$

where the  $a$ 's are constants. Using this fit, the desired  $\rho_A$  for any  $M$  can be estimated from

$$\rho_A = \left( 1 + 10^{P_A(M)} \right) \rho'_A. \quad (6)$$

We carried out simulations of  $\rho'_i$  for a set of aerosol profiles, concentrations, and type to test the accuracy with which  $\rho_A$  could be estimated given  $\rho'_i$ , if the three steps described at the beginning of this section were used. First we estimated  $\rho'_r$  from  $\rho_r$  using Eq. (4). This provided  $\rho'_A = \rho'_i - \rho'_r$ . Then we estimated  $\rho_A$  from  $\rho'_A$  using Eq. (6), based on their relationship in Figure 5, for the simple base profile. Figures 6 and 7 report the error,  $\Delta\rho_A$ , in this prediction of  $\rho_A$  from  $\rho'_i$ . In Figure 7 the Shettle and Fenn<sup>14</sup> Tropospheric aerosol at 50% relative humidity (T50) has been used as the aerosol type in all layers, although the base aerosol was still M50. Two important conclusions can be drawn from the computations presented in these figures: (1) when the base profile is correct, the error in  $\rho_A$  is  $\lesssim 0.5\%$  for  $M \lesssim 5$ , and nearly independent of the aerosol concentration and the aerosol type; and (2) even with the incorrect base profile, the error is usually  $\lesssim 1\%$  as long as the test profile is not "too different" from the base profile (the case with a 5 km scale height in the free troposphere would be an example of a "too different" profile). This suggests that using the methodology described here,  $\rho_A$  can be derived from  $\rho'_i$  with an error  $\lesssim 1\%$  as long as a realistic base aerosol profile is employed.

### C. Choice of the base aerosol profile and type.

From the results presented above it is clear that it is important to use as realistic a base aerosol profile as possible. In fact, the computations suggest that the base profile should have some aerosol in the free troposphere and the stratosphere (unless these happen to be aerosol free) in order to be assured that the error in  $\rho_A \lesssim 1\%$ . With this in mind, we choose the base aerosol in the following manner. Referring to Figure 2, we use the Shettle and Fenn<sup>14</sup> Maritime model with 80% relative humidity (M80) in the marine boundary layer, and their Tropospheric model with relative humidity of 50% (T50) for the free troposphere. The background stratospheric model<sup>19</sup> (B) is proposed for the stratosphere. The volcanic component is taken to be absent in the base profile. The aerosol concentrations are adjusted so that when the visible range (defined<sup>14</sup> to be 3.96 divided by the total extinction coefficient at 550 nm) is 25 km, the aerosol extinction coefficient is a continuous function of altitude, i.e., there is no discontinuous jump in the aerosol extinction from the top of the boundary layer to the bottom of the free troposphere of the type shown on the figure. Note, for any wavelength other than 550 nm, discontinuities in aerosol extinction will occur at the boundaries of

each region because the extinction coefficient for each region will have a different spectral variation. The base aerosol is denoted by M80-T50-B, which stands for M80 in the boundary layer, T50 in the free troposphere, and B in the stratosphere. Similar notation will be used for aerosol profiles through out the remainder of this paper. The  $(\rho_A - \rho'_A)/\rho'_A - M$  relationship for this base aerosol profile is provided in Figure 8. Comparison with Figure 5 shows that for a given  $M$ ,  $(\rho_A - \rho'_A)/\rho'_A$  is slightly smaller (less  $O_2$  absorption) than it is for the base profile with all of the aerosol in the marine boundary layer. For the M-80-T50-B base profile, the values of  $a_{A0}$ ,  $a_{A1}$ , and  $a_{A2}$  in Eq. (5) are  $-1.0796$ ,  $+9.0481 \times 10^{-2}$ , and  $-6.8452 \times 10^{-3}$ , respectively.

### Application to atmospheric correction

In this section we apply the  $O_2$  absorption correction scheme developed above to simulated ocean color data, e.g., SeaWiFS or OCTS. We will examine the optimum case, i.e., assume that the aerosol profile in the free troposphere and stratosphere is identical to the base profile. Only the aerosol in the boundary layer is allowed to be different from the base profile in concentration and/or in type. This of course would require knowing the free troposphere and stratospheric aerosol profile in advance.

We examined the following cases: (1) a visible range ( $VR$ ) of 40 km, with the Maritime (M80) or Tropospheric (T80) aerosol at 80% relative humidity in the marine boundary layer; and (2) the same aerosol models with  $VR = 15$  km. These correspond to either  $\sim 40\%$  less (case 1) or  $\sim 72\%$  more (case 2) aerosol in the boundary layer than in the base profile. The total and boundary-layer aerosol optical thicknesses for these models are provided in Tables 1–4.

Simulations were carried out for both  $\rho'_t$  and  $\rho_t$  so we could compare the performance of the algorithm in the presence and absence of the  $O_2$  absorption to test the efficacy of the  $O_2$  correction. The geometry of the simulations consisted of solar zenith angles  $\theta_0 = 0(20^\circ)60^\circ$ , with  $\theta_v = 0^\circ$  and  $\sim 45^\circ$  corresponding, respectively, to viewing at the scan center and the scan edge. All the simulations were carried out using the Monte Carlo code described above. The simulated value  $\rho'_t$  (in the presence of the  $O_2$  absorption) at 765 nm was then combined with  $\rho_r$  through Eqs. (4) and (6) to estimate  $\rho_A$ , which was then used in the SeaWiFS correction algorithm. For comparison,

in the absence of the  $O_2$  absorption, the simulated  $\rho_t$  was used in the normal way in the correction algorithm.<sup>9</sup> The measure of effectiveness of the combined algorithm ( $O_2$  removal and atmospheric correction) is the ability to recover  $|t\rho_w|$  at 443 nm with an error of  $\lesssim 0.002$ . In this paper, the particular implementation of the algorithm provided in Ref. 9 utilizes the Maritime, Coastal, and Tropospheric models at relative humidities of 50%, 70%, 90%, and 99% as twelve candidate aerosol models. As in Ref. 9, it is assumed in this implementation that the aerosol is confined to the marine boundary layer.

Figures 9a-9d and 10a-10d show the error in the retrieved value of  $t\rho_w$  (called  $\Delta\rho$  on the figures) as a function of  $\theta_0$  and  $\theta_v$ , for the four test cases: M80-T50-B and T80-T50-B with  $VR = 15$  and 40 km. The open circles represent the error in the retrieval if the spectral band from 745 to 785 nm were free of  $O_2$  absorption. Note that even if the  $O_2$  absorption were absent,  $\Delta\rho$  can at times be quite large. This owes to the fact that in the preparation of the lookup tables for implementation the SeaWiFS algorithm it was assumed that the aerosol was all in the marine boundary layer, i.e., a two-layer radiative transfer code (aerosols on the bottom) was employed. This assumption leads to errors when the aerosol is not confined near the surface. Even so, Figure 9 shows that when the aerosol optical depth at 443 is  $\lesssim 0.4$  the correction error is within the desired range, i.e.,  $\pm 0.002$ . In contrast, when the optical thickness at 443 reaches 0.7-0.8 (Figure 10), the error can become excessive. Measurements suggest that optical thicknesses in the latter range are not common when the aerosol is locally generated over the oceans.<sup>24,25</sup> These simulations suggest that, even in the absence of the  $O_2$  absorption, e.g., the atmospheric correction of MODIS, the assumptions made by Gordon and Wang<sup>9</sup> may need to be modified by the addition of a third intermediate layer containing a mixture of aerosol and Rayleigh scatterers.

However, our main concern here is the efficacy of the removal of the effects of the  $O_2$  absorption from the atmospheric correction. For this purpose we need only compare the differences between the open circles and the filled circles in Figures 9 and 10. We note that the difference is usually  $\lesssim 0.001$  and often considerably less, indicating that the  $O_2$  correction works reasonably well. Recall that if  $\rho_A$  is too small, an undercorrection will occur, i.e., the water-leaving reflectance at 443 will be too large ( $\Delta\rho > 0$ ). Thus, in Figure 9,  $\rho_A$  is a little too large, while in Figure 10 it is

too small. This is consistent with the fact that the  $(\rho_A - \rho'_A)/\rho'_A - M$  relationships in Figure 8 will move upward (more absorption) if the aerosol concentration in the boundary layer is increased and downward if the concentration is decreased with respect to the base profile. This implies that for the cases in Figure 10,  $P_A(M)$  in Eq. (6) will lead to a value of  $\rho_A$  that is too small, while for the cases in Figure 9, the reverse is true.

To provide an appreciation of the magnitude of the  $O_2$  effect that has been removed, in Table 5 we present the average  $\Delta\rho$  over  $\theta_0$  for each model when the existence of the  $O_2$  absorption is simply ignored and the proposed SeaWiFS algorithm operated using  $\rho'_t$ . Comparison with the results in Figures 9 and 10 suggest that we have removed about 97% of the error in the worst case (T80-T50-B at the scan edge).

In the simulated test of the  $O_2$  absorption correction above, we used a base profile that was correct for the free troposphere and the stratosphere. This should be the optimum situation. To try to understand the effect of choosing an incorrect base profile on the end-to-end atmospheric correction algorithm, we computed  $\Delta\rho$  using the base profile that was used in the preparation of Figure 5, i.e., a base profile assuming that all of the aerosol is in the boundary layer and modeled as M50. This is in contrast to the base profile used in the preparation of Figures 9 and 10 in which  $\sim 30\%$  of the aerosol optical thickness at 765 nm was above the boundary layer. The resulting corrections at the scan center using M50 as the base profile are provided in Figure 11. Comparing Figures 9a with 11a, 9b with 11b, 10a with 11c, and 10b with 11d, we see that the filled circles are  $\lesssim 0.001$  (and typically much less) lower using the M50 base profile compared to the M80-T50-B base profile. Thus, a large error in the base profile does not significantly influence the overall atmospheric correction. In fact, for the  $VR = 15$  km case, the incorrect base profile actually produces better corrections. Similar results are obtained at the scan edge (not shown).

### Volcanic Aerosols

A situation in which the base profile can strongly influence the atmospheric correction is that following volcanic eruptions, e.g., El Chichón, which can inject significant quantities of aerosol into the stratosphere. To understand the effect of this on the  $O_2$  correction presented above, we have

examined four cases with volcanic aerosol. We used the El Chichón aerosol model developed by King et al.<sup>20</sup> and considered the aerosol to be concentrated in a layer from 18 to 20 km (Figure 2). The optical thickness at 550 nm was taken to be 0.05 or 0.10. Figure 12 provides the results of simulated retrieval errors  $\Delta\rho$  at the scan center as a function of  $\theta_0$ . The notation for the aerosol profile now includes "V" followed by a number indicating the volcanic aerosol optical thickness at 550 nm, e.g., M80-T50-B-V05 indicates the addition of a volcanic aerosol with optical thickness 0.05 at 550 nm, etc. Examination of Figure 12 shows that the error in the presence of the O<sub>2</sub> absorption (filled circles) is always below (more negative) the error what would occur in the absence of O<sub>2</sub> absorption (open circles). This occurs because the presence of the volcanic aerosol causes less O<sub>2</sub> absorption than the base profile. Thus,  $P_A(M)$  in Eq. (6) is too large so  $\rho_A$  will be too large resulting in an overcorrection ( $\Delta\rho < 0$ ). The effect is more significant the greater the contribution from the volcanic aerosol compared to the boundary-layer aerosol. This can be seen by comparing Figures 9a, 12a, and 12b for which the volcanic optical thickness progresses from 0 to 0.05 to 0.10 with  $VR = 40$  km, and Figures 10a, 12c, and 12d, for  $VR = 15$  km. For  $VR = 40$  km, we see a slow degradation in the quality of the atmospheric correction even in the absence of O<sub>2</sub> absorption with increasing volcanic optical thickness and a large overcorrection in the presence of O<sub>2</sub> absorption. In contrast, for  $VR = 15$  km we see the same slow degradation in the absence of O<sub>2</sub> absorption, but a smaller O<sub>2</sub> absorption overcorrection.

It is clear that application of the proposed O<sub>2</sub> absorption correction in the presence of volcanic aerosol will require information concerning the vertical distribution, concentration, and optical properties of the volcanic aerosol.

### Summary and Conclusions

By simulating the radiance reflected from the ocean-atmosphere system in the O<sub>2</sub> "A" absorption band using a line-by-line backward Monte Carlo radiative transfer code, we have shown the influence of the absorption band on the atmospheric correction of ocean color sensors utilizing a ~ 745–785 spectral band, e.g., SeaWiFS and OCTS. If the O<sub>2</sub> absorption is ignored, unacceptable errors in the water-leaving reflectance will result (Table 5). However, given an aerosol profile — the base profile — through simulations we have found a simple empirical relationship (Eq. (6))

that removes the effect of the absorption from the aerosol component of the reflectance ( $\rho_a + \rho_{ra}$ ). Combining this with a similar empirical expression (Eq. (4)) for the Rayleigh scattering component ( $\rho_r$ ), allows application of the atmospheric correction algorithm developed by Gordon and Wang,<sup>9</sup> that ignored the O<sub>2</sub> absorption. Test simulations in which the actual aerosol profile and the base profiles were identical *above* the marine boundary layer suggest that the difference in the error in the retrieval of the water-leaving reflectance due to the presence of the O<sub>2</sub> absorption is usually reduced to  $\ll 0.001$  using the empirical relations. An important feature of this method of correction for the effects of the O<sub>2</sub> absorption is that it employs lookup tables that can be prepared in the absence of O<sub>2</sub> absorption using more efficient radiative transfer codes.

The dependence of the O<sub>2</sub> absorption correction on an assumed profile is unsatisfying; however, the dependence is very weak (Figures 6, 7, and 11). One exception is the addition of volcanic aerosol which, if ejected into the stratosphere, will cause serious difficulty in the removal of the O<sub>2</sub> absorption effect (Figure 12). A second exception is the presence of thin cirrus clouds. These will produce effects similar to volcanic aerosols. However, in either case the atmospheric correction even in the absence of O<sub>2</sub> absorption is seen to be degraded by the introduction of a high-altitude aerosol layer (e.g., compare Figures 10a, 12c, and 12d). Recalling that in the Gordon and Wang<sup>9</sup> correction algorithm it was assumed that *all* of the aerosol is in the marine boundary layer, this suggests that the basic algorithm itself may have to be modified to incorporate the effects of such aerosols. A simple modification would be to use a more realistic vertical distribution of aerosol which would include some aerosol in the free troposphere and stratosphere. This would also improve the performance of the algorithm in the presence of O<sub>2</sub> absorption.

Finally, it may be possible to identify the presence of volcanic aerosol or cirrus clouds from SeaWiFS imagery. A method we are examining involves the SeaWiFS band at 670 nm. For  $C \lesssim 1$  mg/m<sup>3</sup>,  $\rho_w$  at 670 nm is very small, i.e.,  $\lesssim 0.0008$ . Simulations at 670 nm with volcanic aerosol (similar to those presented in Figure 12) suggest that the recovered  $\rho_w$  there will be negative if there is a significant volcanic aerosol layer, e.g., a stratospheric aerosol optical thickness of 0.05 – 0.10. Thin cirrus clouds would produce a similar effect.

## References

- [1] W. A. Hovis, D. K. Clark, F. Anderson, R. W. Austin, W. H. Wilson, E. T. Baker, D. Ball, H. R. Gordon, J. L. Mueller, S. Y. E. Sayed, B. Strum, R. C. Wrigley and C. S. Yentsch, "Nimbus 7 coastal zone color scanner: system description and initial imagery," *Science* **210**, 60-63 (1980).
- [2] H. R. Gordon, D. K. Clark, J. L. Mueller and W. A. Hovis, "Phytoplankton pigments derived from the Nimbus-7 CZCS: initial comparisons with surface measurements," *Science* **210**, 63-66 (1980).
- [3] H. R. Gordon, J. W. Brown and R. H. Evans, "Exact Rayleigh Scattering Calculations for use with the Nimbus-7 Coastal Zone Color Scanner," *Applied Optics* **27**, 862-871 (1988).
- [4] H. R. Gordon and D. K. Clark, "Clear water radiances for atmospheric correction of coastal zone color scanner imagery," *Applied Optics* **20**, 4175-4180 (1981).
- [5] G. C. Feldman, N. Kuring, C. Ng, W. Esaias, C. R. McClain, J. Elrod, N. Maynard, D. Endres, R. Evans, J. Brown, S. Walsh, M. Carle and G. Podesta, "Ocean Color: Availability of the Global Data Set," *EOS Trans. Amer. Geophys. Union* **70**, 634-641 (1989).
- [6] R. H. Evans and H. R. Gordon, "CZCS 'System Calibration:' A retrospective examination," *Jour. Geophys. Res.* **99C**, 7293-7307 (1994).
- [7] S. B. Hooker, W. E. Esaias, G. C. Feldman, W. W. Gregg and C. R. McClain, *SeaWiFS Technical Report Series: Volume 1, An Overview of SeaWiFS and Ocean Color* (NASA Technical Memorandum 104566, July 1992).



- [8] V. V. Salomonson, W. L. Barnes, P. W. Maymon, H. E. Montgomery and H. Ostrow, "MODIS: Advanced Facility Instrument for Studies of the Earth as a System," *IEEE Geosci. Rem. Sens.* **27**, 145-152 (1989).
- [9] H. R. Gordon and M. Wang, "Retrieval of water-leaving radiance and aerosol optical thickness over the oceans with SeaWiFS: A preliminary algorithm," *Applied Optics* **33**, 443-452 (1994).
- [10] P. Y. Deschamps, M. Herman and D. Tanre, "Modeling of the atmospheric effects and its application to the remote sensing of ocean color," *Applied Optics* **22**, 3751-3758 (1983).
- [11] H. R. Gordon, D. K. Clark, J. W. Brown, O. B. Brown, R. H. Evans and W. W. Broenkow, "Phytoplankton pigment concentrations in the Middle Atlantic Bight: comparison between ship determinations and Coastal Zone Color Scanner estimates," *Applied Optics* **22**, 20-36 (1983).
- [12] M. Wang and H. R. Gordon, "*Influence of Oceanic Whitecaps on Atmospheric Correction of SeaWiFS*," Accepted for publication in *Applied Optics*.
- [13] W. M. Balch, P. M. Holligan, S. G. Ackleson and K. J. Voss, "Biological and optical properties of mesoscale coccolithophore blooms in the Gulf of Maine," *Limnology and Oceanography* **34**, 629-643 (1991).
- [14] E. P. Shettle and R. W. Fenn, *Models for the Aerosols of the Lower Atmosphere and the Effects of Humidity Variations on Their Optical Properties* (Air Force Geophysics Laboratory, Hanscomb AFB, MA 01731, AFGL-TR-79-0214, 1979).
- [15] L. S. Rothman, R. R. Gamache, A. Barbe, A. Goldman, J. R. Gillis, L. R. Brown, R. A. Toth, J. -M. Flaud and C. Camy-Peyret, "AFGL atmospheric absorption line parameters compilation: 1982 edition," *Applied Optics* **22**, 2247-2256 (1983).

- [16] R. W. Fenn, S. A. Clough, W. O. Gallery, R. E. Good, F. X. Kenizys, J. D. Mill, L. S. Rothman, E. P. Shettle and F. E. Volz, "Optical and Infrared Properties of the Atmosphere," in *Handbook of Geophysics and the Space Environment*, edited by A. S. Jursa (Air Force Geophysics Laboratory, Hanscomb AFB, MA, 1985) p. 18-1-18-80.
- [17] C. Cox and W. Munk, "Measurements of the Roughness of the Sea Surface from Photographs of the Sun's Glitter," *Jour. Opt. Soc. of Am.* 44, 838-850 (1954).
- [18] COESA, "U.S. Standard Atmosphere 1976," U.S. Government Printing Office, Washington, D.C. 1976.
- [19] WCP-112, *A preliminary cloudless standard atmosphere for radiation computation* (World Meteorological Organization, WMO/TD-No. 24, Geneva).
- [20] M. D. King, Harshvardhan and A. Arking, "A Model of the Radiative Properties of the El Chichón Stratospheric Aerosol Layer," *Journal of Climate and Applied Meteorology* 23, 1121-1137 (1984).
- [21] F. X. Kenizys, E. P. Shettle, L. W. Abreu, G. P. Anderson, J.H. Chetwynd, W. O. Gallery, J. E. A. Selby and S. A. Clough, *Atmospheric Transmittance/Radiance: The LOWTRAN 7 Model* (Air Force Geophysics Laboratory, Hanscomb AFB, MA 01731, 1989), In Preparation.
- [22] R. G. Isaacs, W. -C. Wang, R. D. Worsham and S. Goldenberg, "Multiple scattering LOW-TRAN and FASCODE models," *Applied Optics* 28, 1272-1281 (1987).
- [23] K. N. Liou, *Radiation and Cloud Processes in the Atmosphere* (Oxford University Press, New York, 1992), 487 pp.

- [24] W. A. Hoppel, J. W. Fitzgerald, G. M. Frick, R. E. Larson and E. J. Mack, "Aerosol Size Distributions and Optical Properties Found in the Marine Boundary Layer Over the Atlantic Ocean," *J. Geophys Res.* **95D**, 3659-3686 (1990).
  
- [25] P. J. Reddy, F. W. Kreiner, J. J. Deluisi and Y. Kim, "Aerosol Optical Depths Over the Atlantic Derived From Shipboard Sunphotometer Observations During the 1988 Global Change Expedition," *Global Biogeochemical Cycles* **4**, 225-240 (1990).

## Figure Captions

Figure 1. A portion of the O<sub>2</sub> A band at 762 nm covering approximately 1.165 nm.

Figure 2. Schematic of the aerosol profile for the atmospheric model described in the text.

Figure 3. Fractional change in reflectance  $(\rho_r - \rho'_r)/\rho'_r$ , as a function of  $M$  for a spectral band from 745 to 785 nm.

Figure 5. Fractional change in reflectance  $(\rho_A - \rho'_A)/\rho'_A$ , as a function of  $M$  for a spectral band from 745 to 785 nm.

Figure 6. Error in the prediction of  $\rho_A$  from  $\rho'_A$  when the actual aerosol profile differs from the base profile.  $h$  is the aerosol scale height. All test profiles use M50.

Figure 7. Error in the prediction of  $\rho_A$  from  $\rho'_A$  when the actual aerosol profile differs from the base profile.  $h$  is the aerosol scale height. All test profiles use T50.

Figure 8.  $(\rho_A - \rho'_A)/\rho'_A$  as a function of  $M$  for the selected base profile.

Figure 9a. Error in the retrieved  $t(443)\rho_w(443)$  for viewing at the center of the scan with aerosol profile M80-T50-B and  $VR = 40$  km.

Figure 9b. Error in the retrieved  $t(443)\rho_w(443)$  for viewing at the center of the scan with aerosol profile T80-T50-B and  $VR = 40$  km.

Figure 9c. Error in the retrieved  $t(443)\rho_w(443)$  for viewing at the edge of the scan with aerosol profile M80-T50-B and  $VR = 40$  km.

Figure 9d. Error in the retrieved  $t(443)\rho_w(443)$  for viewing at the edge of the scan with aerosol profile T80-T50-B and  $VR = 40$  km.

Figure 10a. Error in the retrieved  $t(443)\rho_w(443)$  for viewing at the center of the scan with aerosol profile M80-T50-B and  $VR = 15$  km.

Figure 10b. Error in the retrieved  $t(443)\rho_w(443)$  for viewing at the center of the scan with aerosol profile T80-T50-B and  $VR = 15$  km.

Figure 10c. Error in the retrieved  $t(443)\rho_w(443)$  for viewing at the edge of the scan with aerosol profile M80-T50-B and  $VR = 15$  km.

Figure 10d. Error in the retrieved  $t(443)\rho_w(443)$  for viewing at the edge of the scan with aerosol profile T80-T50-B and  $VR = 15$  km.

Figure 11a. Error in the retrieved  $t(443)\rho_w(443)$  for viewing at the center of the scan with aerosol profile M80-T50-B and  $VR = 40$  km, and a simplified base profile.

Figure 11b. Error in the retrieved  $t(443)\rho_w(443)$  for viewing at the center of the scan with aerosol profile T80-T50-B and  $VR = 40$  km, and a simplified base profile.

Figure 11c. Error in the retrieved  $t(443)\rho_w(443)$  for viewing at the center of the scan with aerosol profile M80-T50-B and  $VR = 15$  km, and a simplified base profile.

Figure 11d. Error in the retrieved  $t(443)\rho_w(443)$  for viewing at the center of the scan with aerosol profile T80-T50-B and  $VR = 40$  km, and a simplified base profile.

Figure 12a. Error in the retrieved  $t(443)\rho_w(443)$  for viewing at the center of the scan with aerosol profile M80-T50-B and  $VR = 40$  km, and the standard base profile, when Volcanic aerosol (V) is added with optical thickness 0.05 at 550 nm.

Figure 12b. Error in the retrieved  $t(443)\rho_w(443)$  for viewing at the center of the scan with aerosol profile M80-T50-B and  $VR = 40$  km, and the standard base profile, when Volcanic aerosol (V) is added with optical thickness 0.10 at 550 nm.

Figure 12c. Error in the retrieved  $t(443)\rho_w(443)$  for viewing at the center of the scan with aerosol profile M80-T50-B and  $VR = 15$  km, and the standard base profile, when Volcanic aerosol (V) is added with optical thickness 0.05 at 550 nm.

Figure 12d. Error in the retrieved  $t(443)\rho_w(443)$  for viewing at the center of the scan with aerosol profile M80-T50-B and  $VR = 15$  km, and the standard base profile, when Volcanic aerosol (V) is added with optical thickness 0.10 at 550 nm.

**Table 1:** Total aerosol optical thickness for model M80-T50-B

| $VR$ (km) | $\lambda$ (nm) |        |        |        |
|-----------|----------------|--------|--------|--------|
|           | 443            | 550    | 765    | 865    |
| 15        | 0.7029         | 0.6345 | 0.5509 | 0.5334 |
| 40        | 0.3594         | 0.3085 | 0.2462 | 0.2259 |

**Table 2:** Boundary-layer aerosol optical thickness for model M80-T50-B

| $VR$ (km) | $\lambda$ (nm) |        |        |        |
|-----------|----------------|--------|--------|--------|
|           | 443            | 550    | 765    | 865    |
| 15        | 0.5242         | 0.4974 | 0.4648 | 0.4538 |
| 40        | 0.1806         | 0.1738 | 0.1602 | 0.1563 |

**Table 3:** Total aerosol optical thickness for model T80-T50-B

| $VR$ (km) | $\lambda$ (nm) |        |        |        |
|-----------|----------------|--------|--------|--------|
|           | 443            | 550    | 765    | 865    |
| 15        | 0.8226         | 0.6345 | 0.4037 | 0.3289 |
| 40        | 0.4006         | 0.3085 | 0.1955 | 0.1589 |

**Table 4:** Boundary-layer aerosol optical thickness for model T80-T50-B

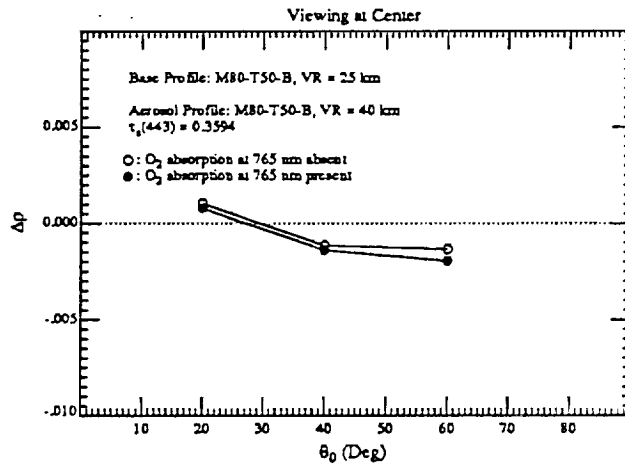
| $VR$ (km) | $\lambda$ (nm) |        |        |        |
|-----------|----------------|--------|--------|--------|
|           | 443            | 550    | 765    | 865    |
| 15        | 0.6438         | 0.4974 | 0.3176 | 0.2592 |
| 40        | 0.2218         | 0.1738 | 0.1095 | 0.0893 |

Table 5:  $\Delta\rho$  when existence of  $O_2$  absorption is ignored.

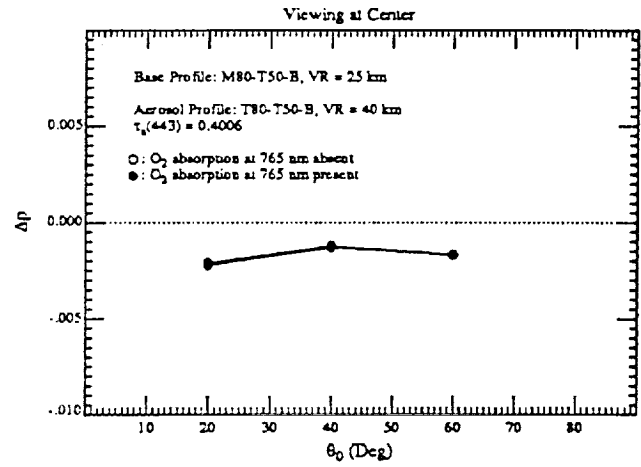
| Model     | $VR$ (km) | Scan Center  | Scan Edge    |  |
|-----------|-----------|--------------|--------------|--|
| M80-T50-B | 40        | $\sim 0.012$ | $\sim 0.014$ |  |
| M80-T50-B | 15        | $\sim 0.013$ | $\sim 0.016$ |  |
| T80-T50-B | 40        | $\sim 0.028$ | $\sim 0.020$ |  |
| T80-T50-B | 15        | $\sim 0.029$ | $\sim 0.031$ |  |



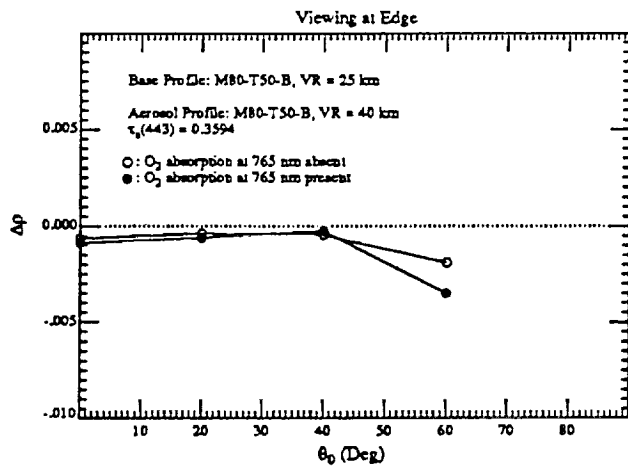
# Suggested layout for Figure 9



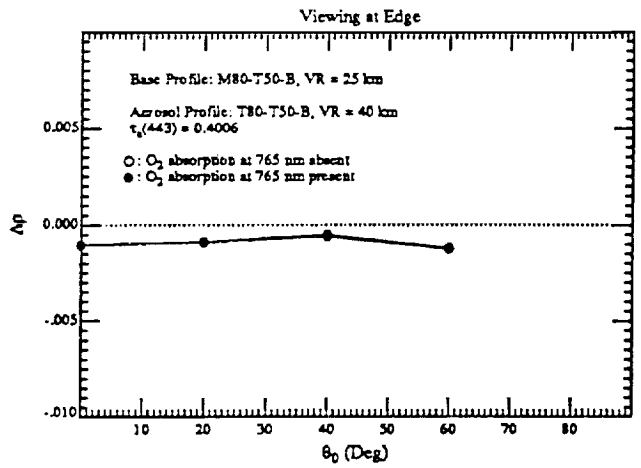
(a)



(b)

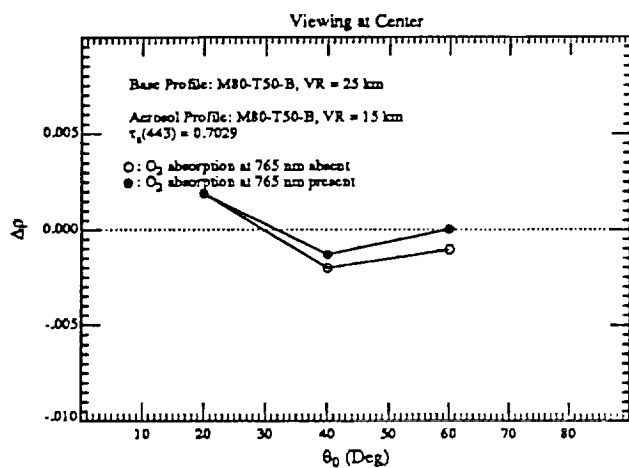


(c)

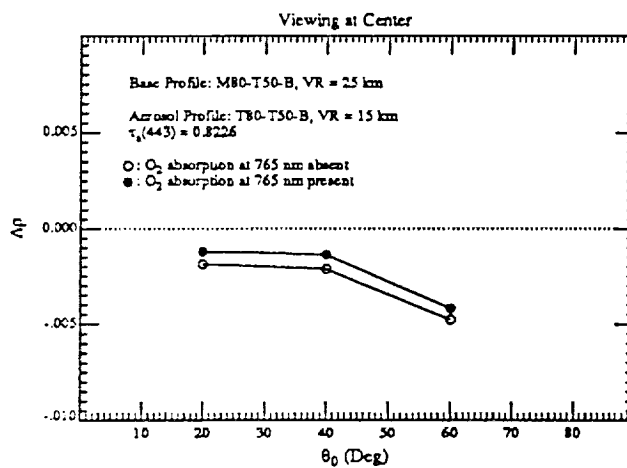


(d)

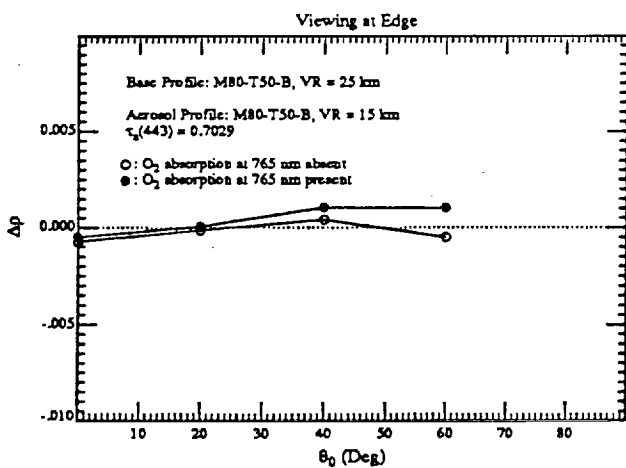
# Suggested layout for Figure 10



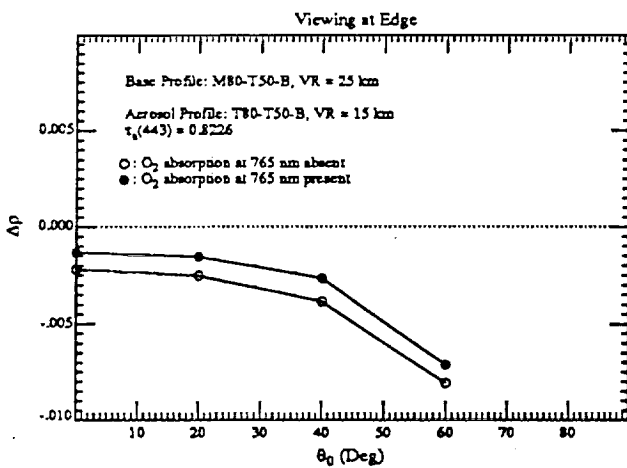
(a)



(b)

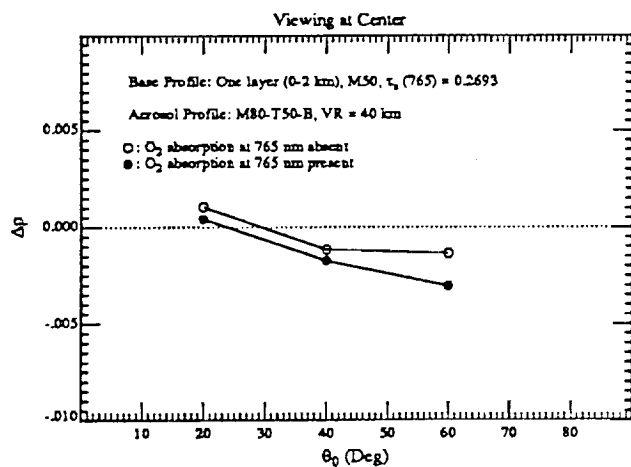


(c)

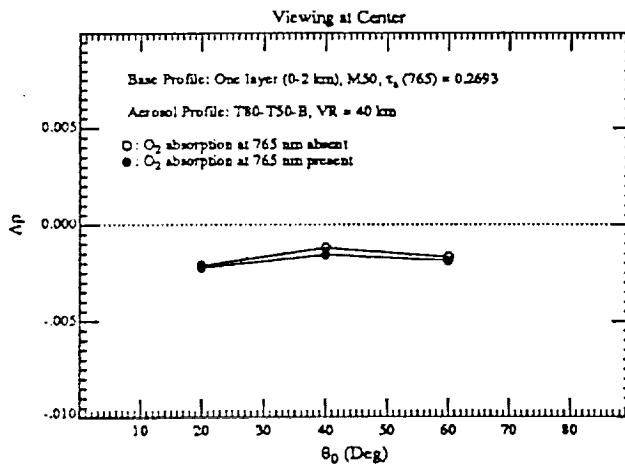


(d)

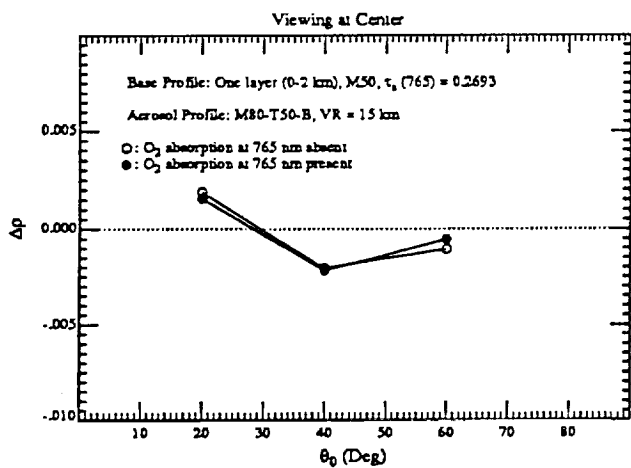
# Suggested layout for Figure 11



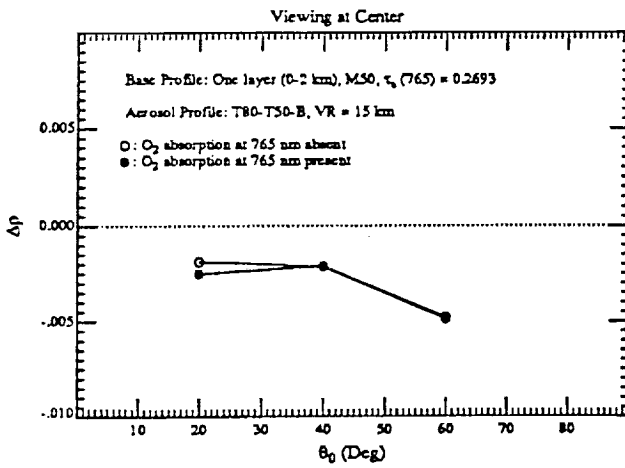
(a)



(b)

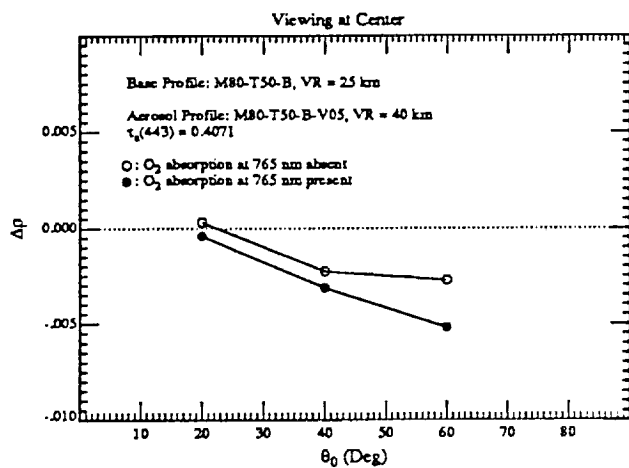


(c)

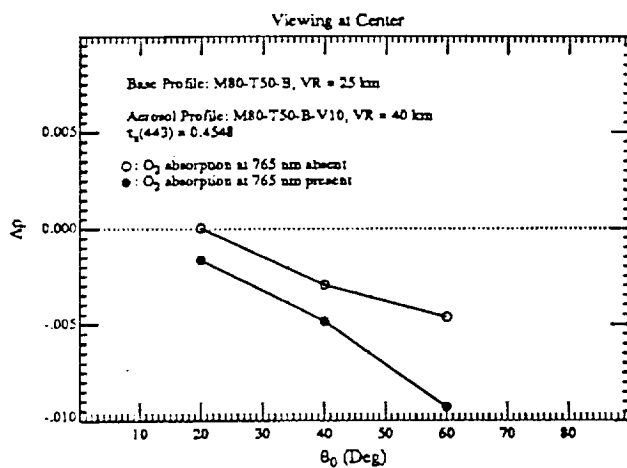


(d)

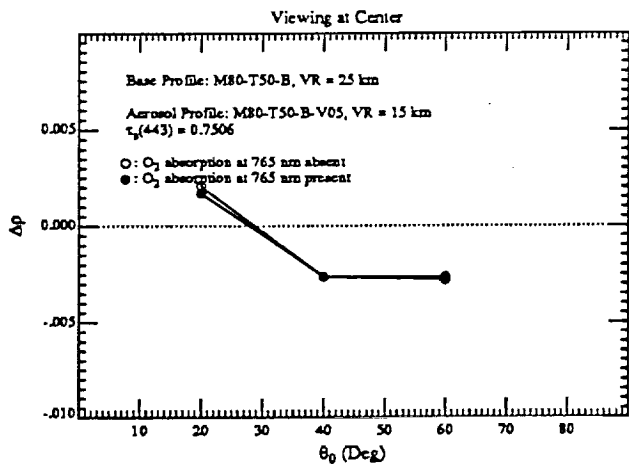
# Suggested layout for Figure 12



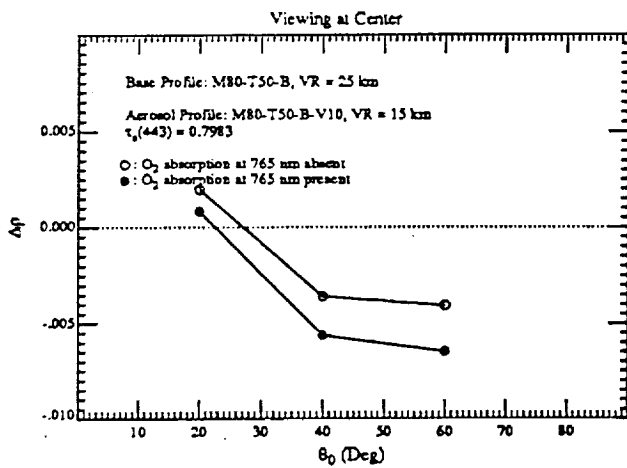
(a)



(b)



(c)



(d)

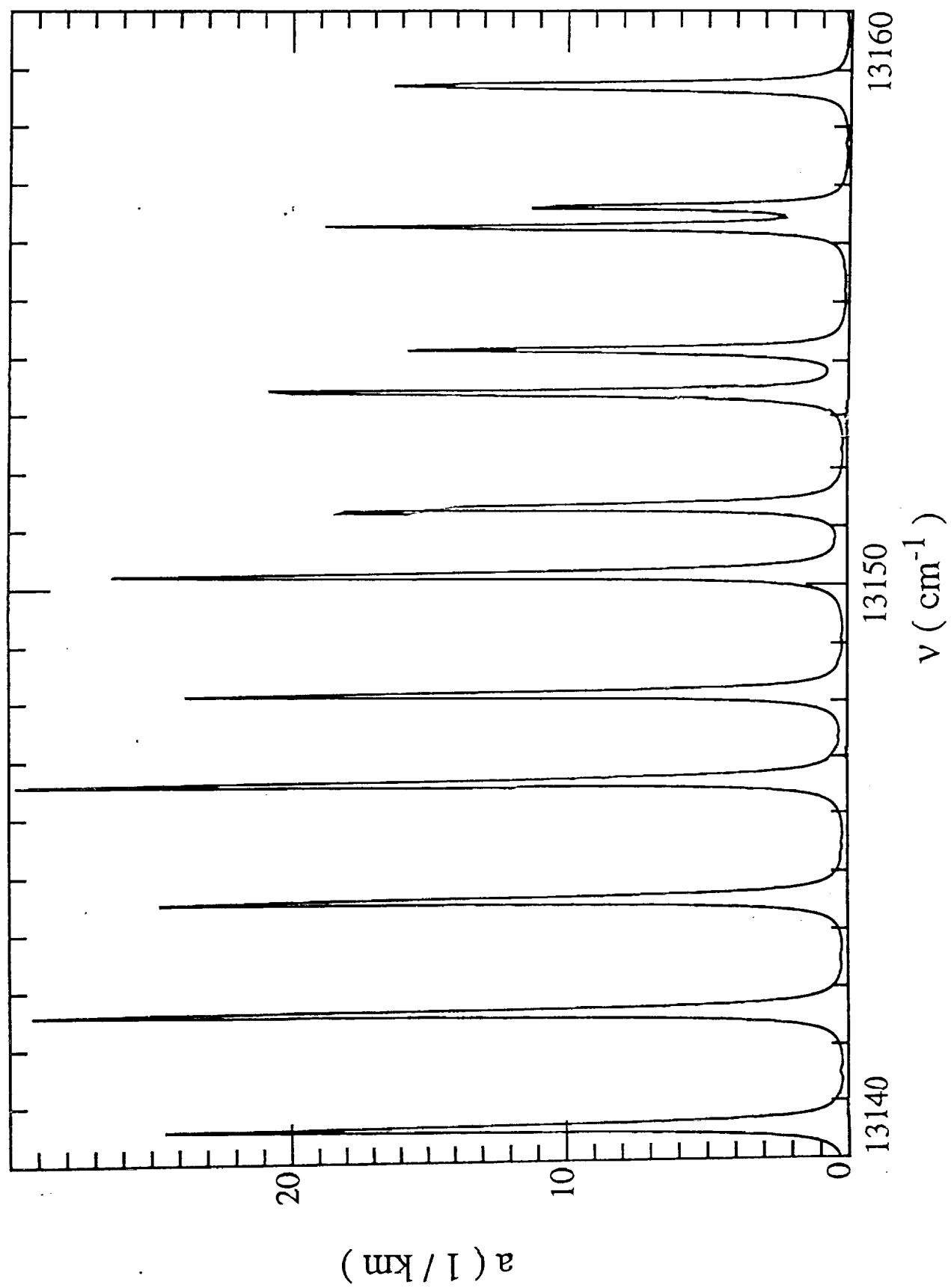


Fig 1

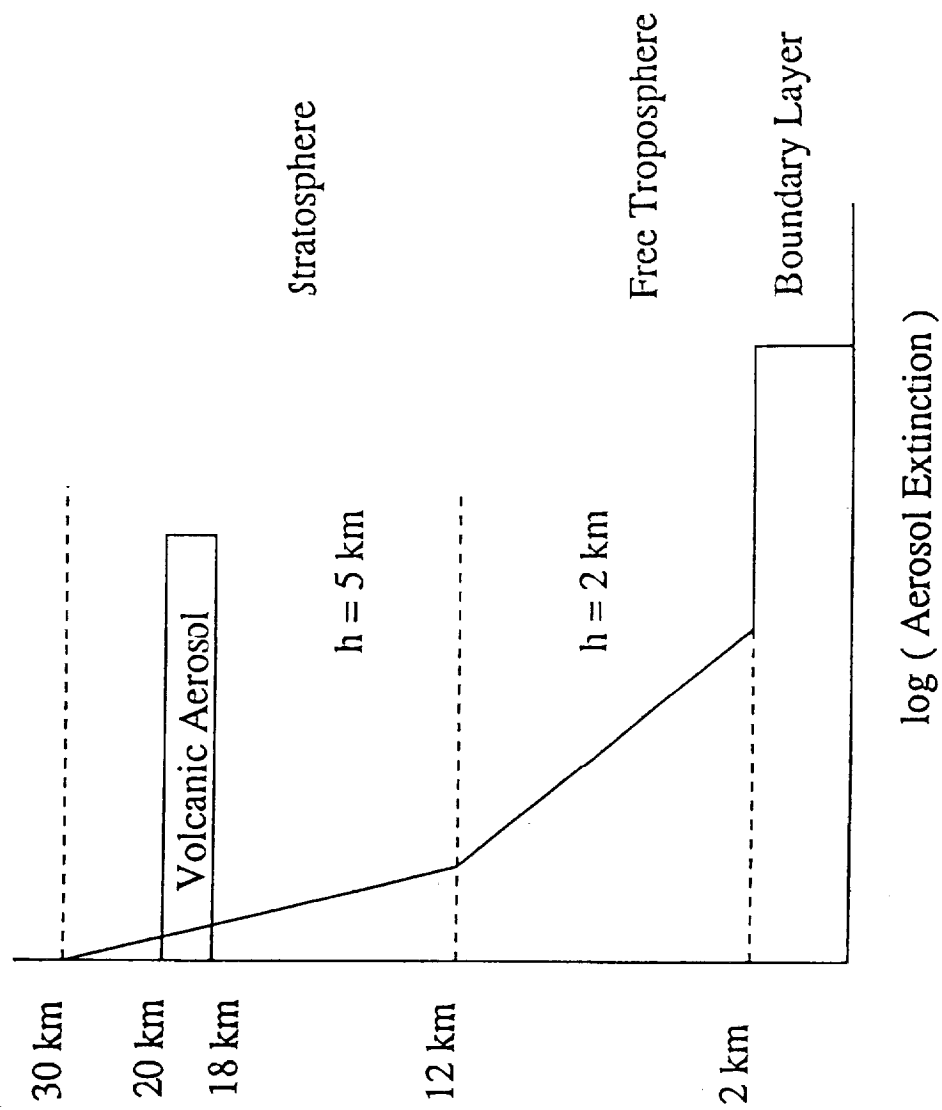


Fig. 2

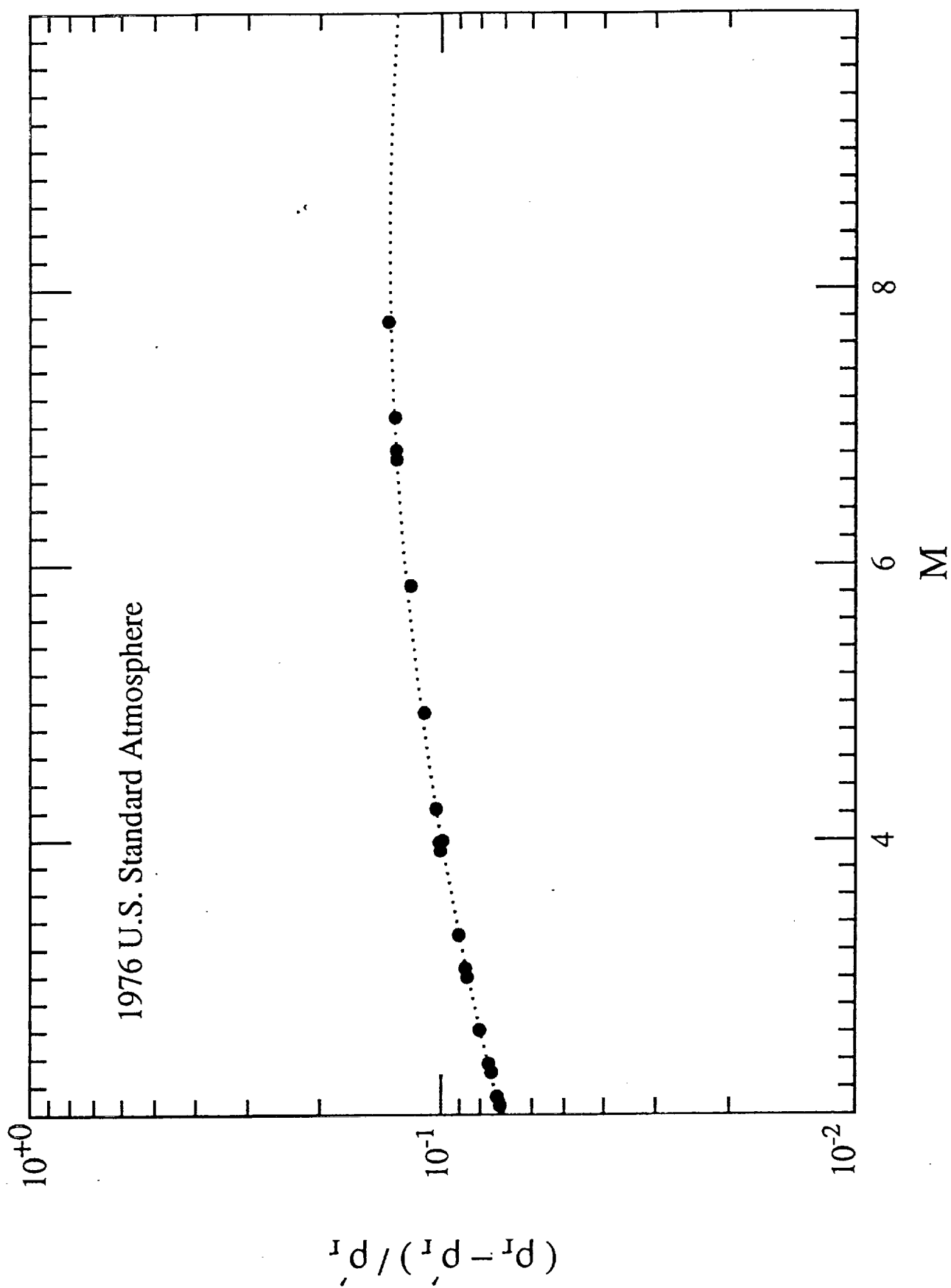


Fig. 3

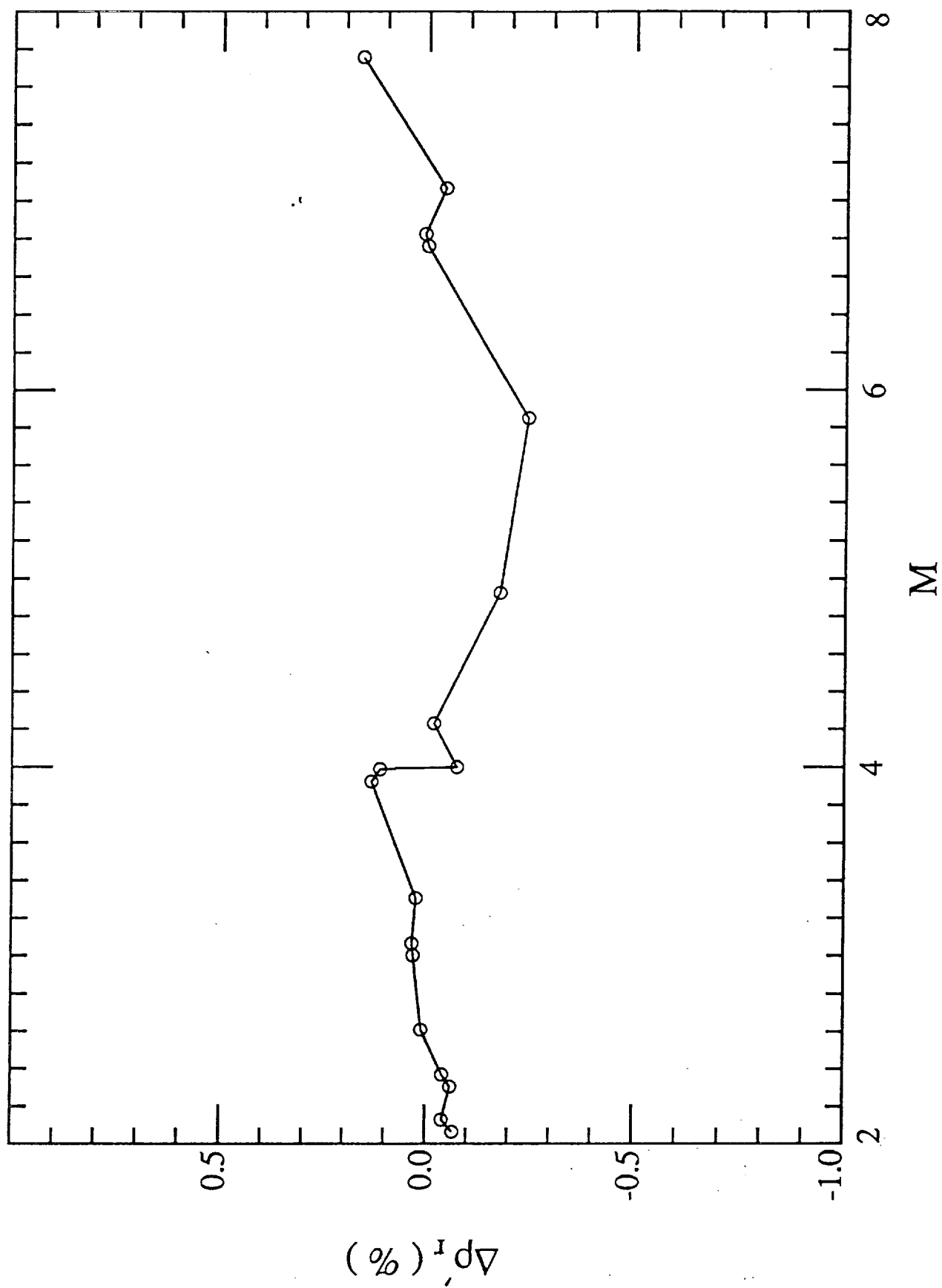


Fig. 4



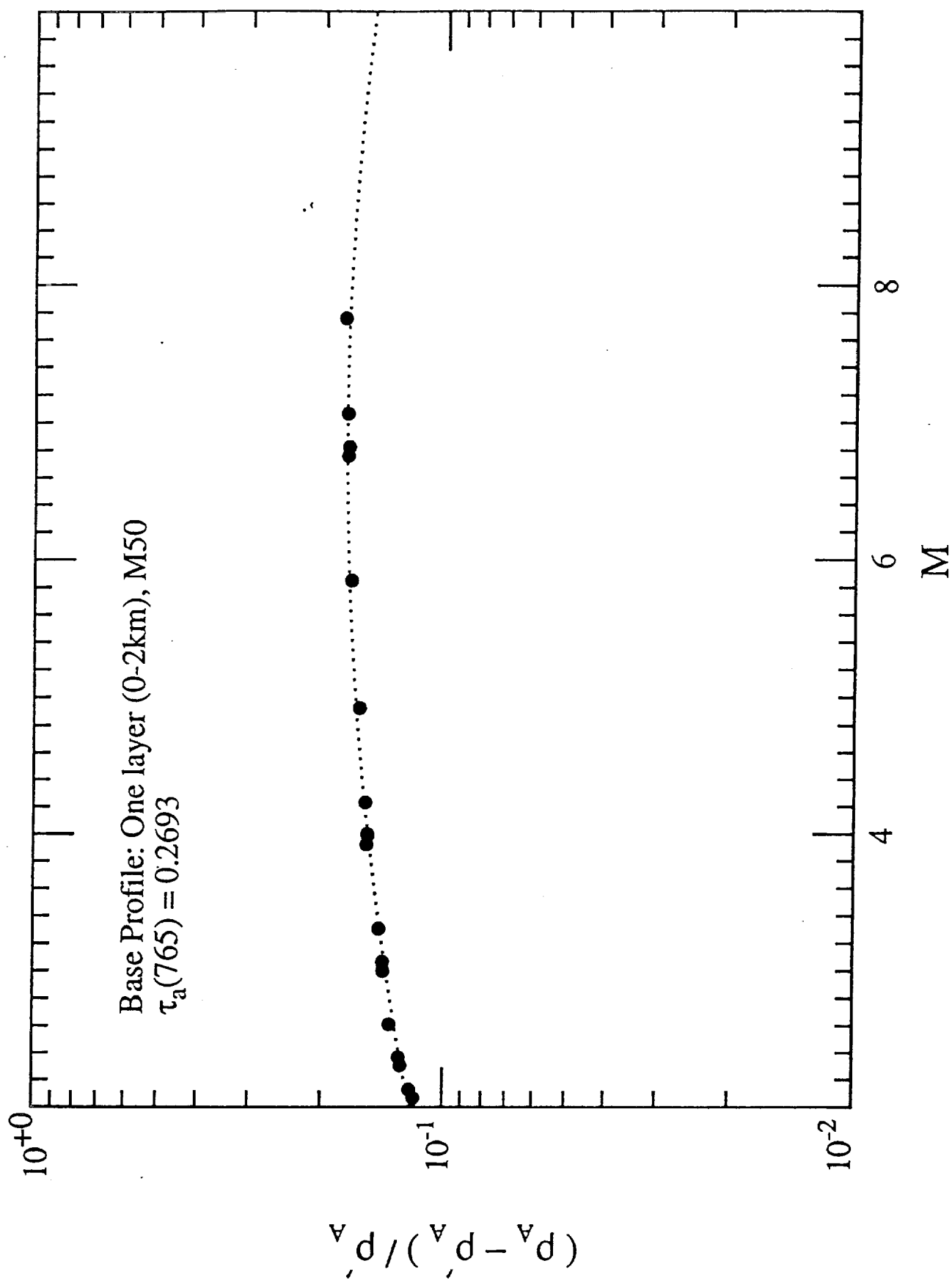


Fig. 5

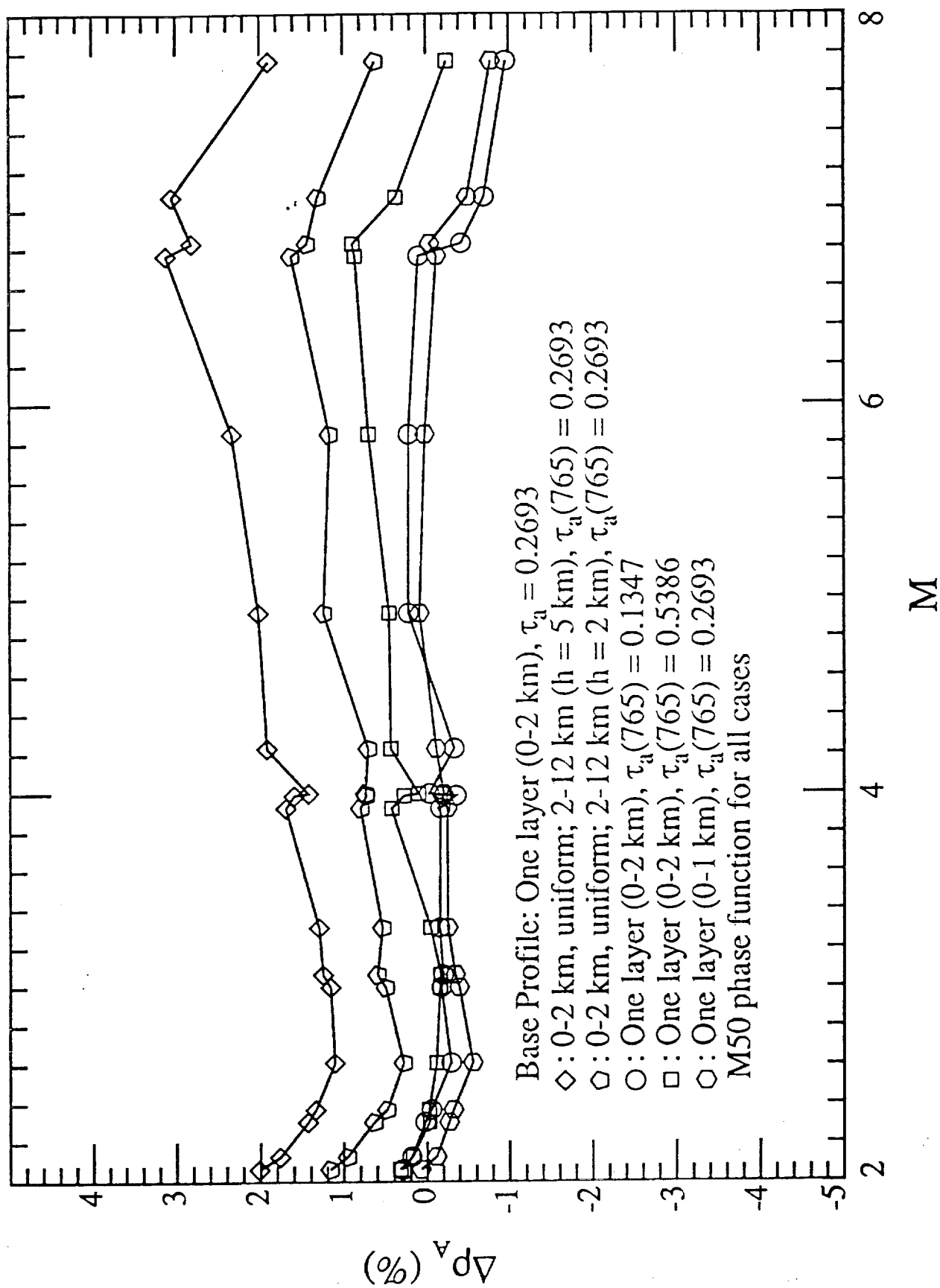


Fig. 6

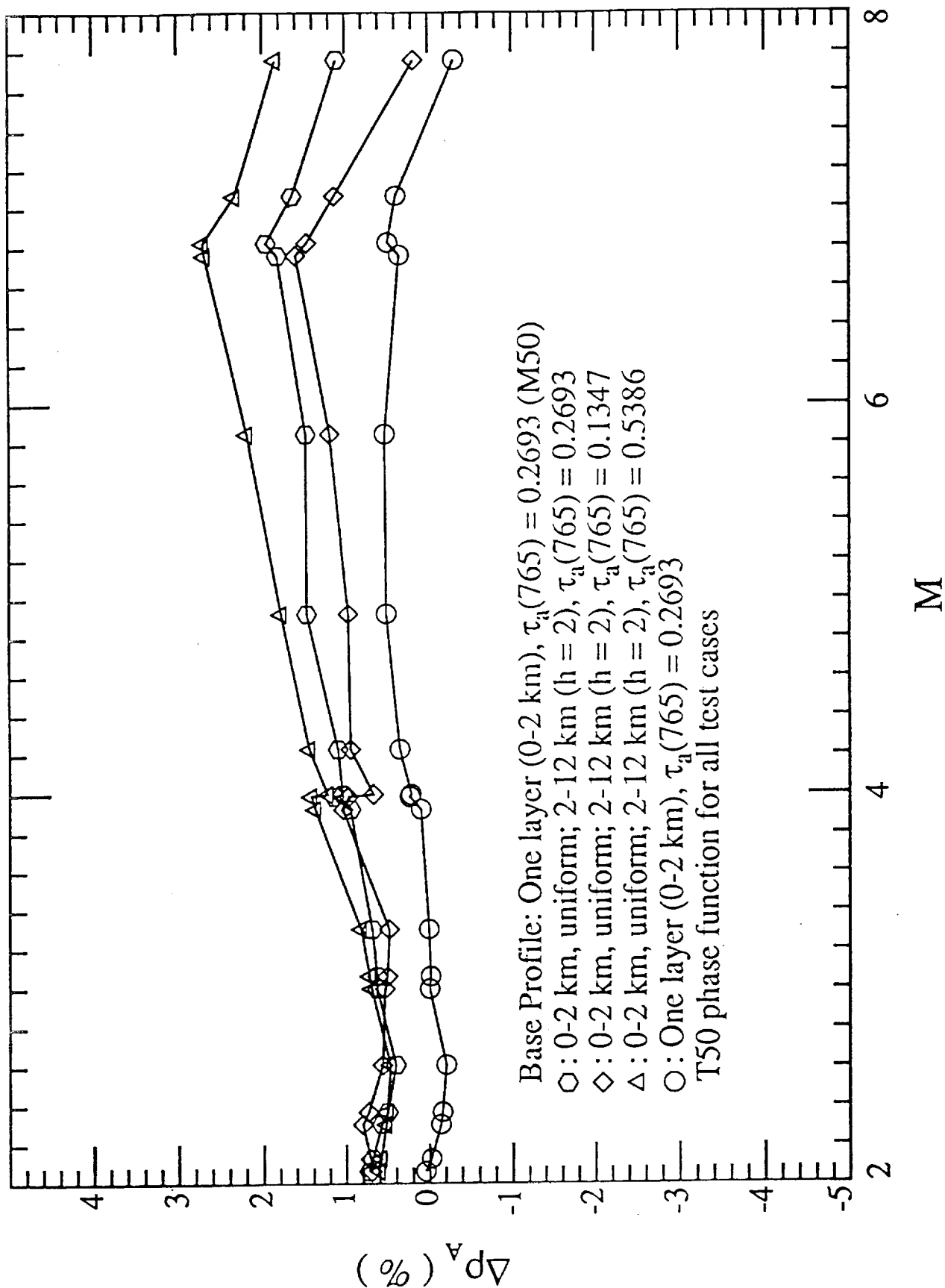


Fig. 7

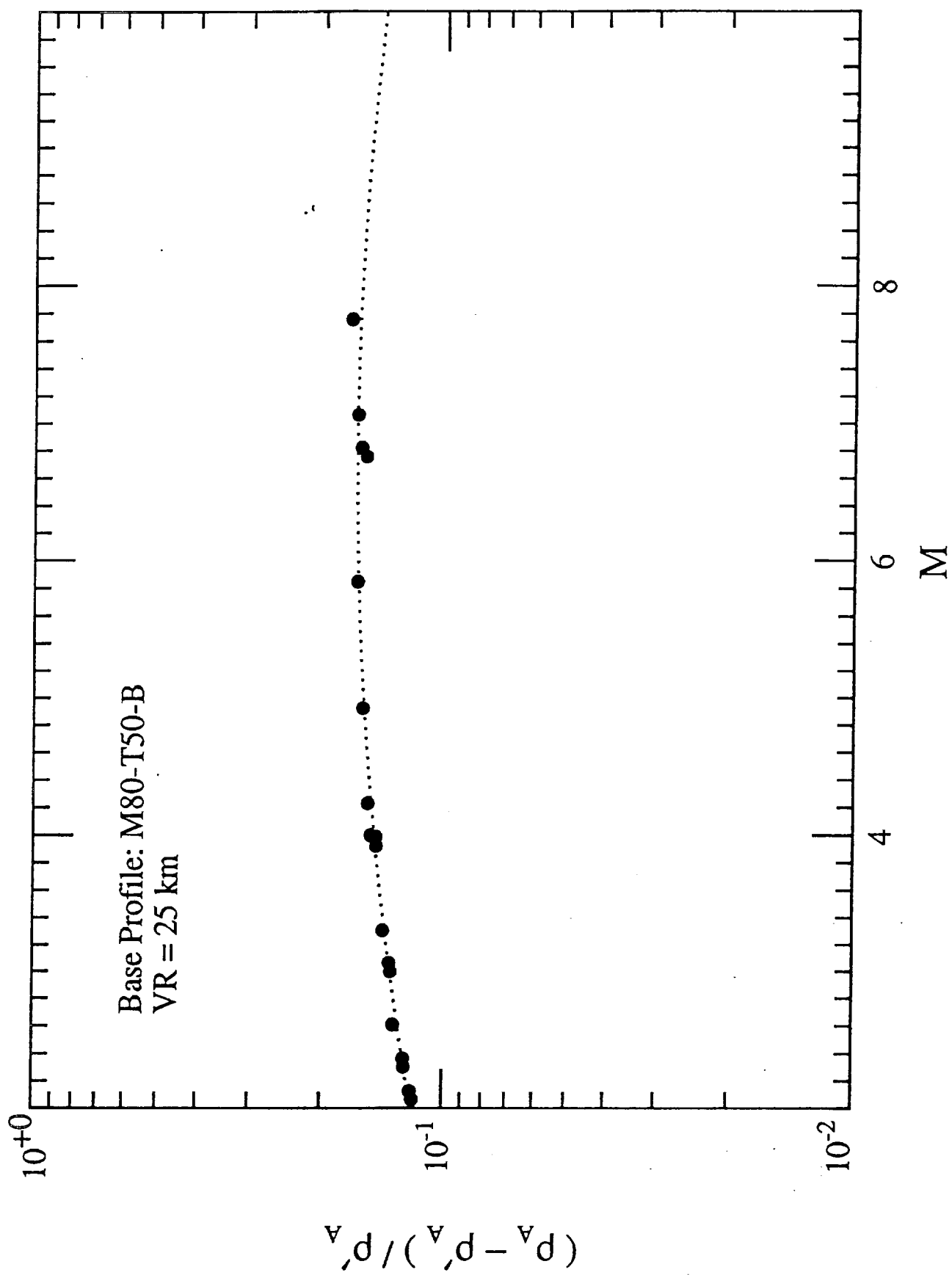


Fig. 8

# Viewing at Center

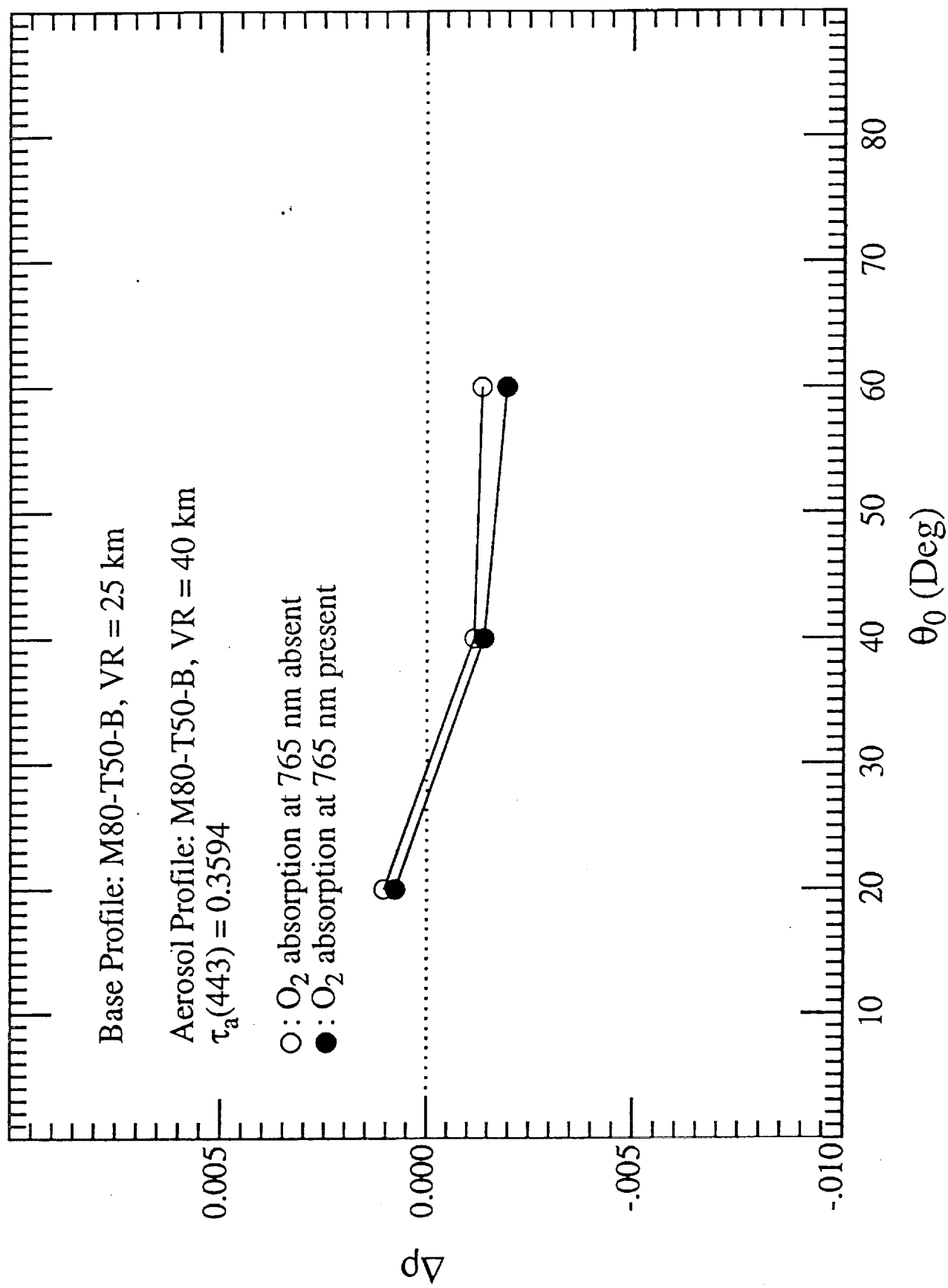


Fig. 9a

Viewing at Center

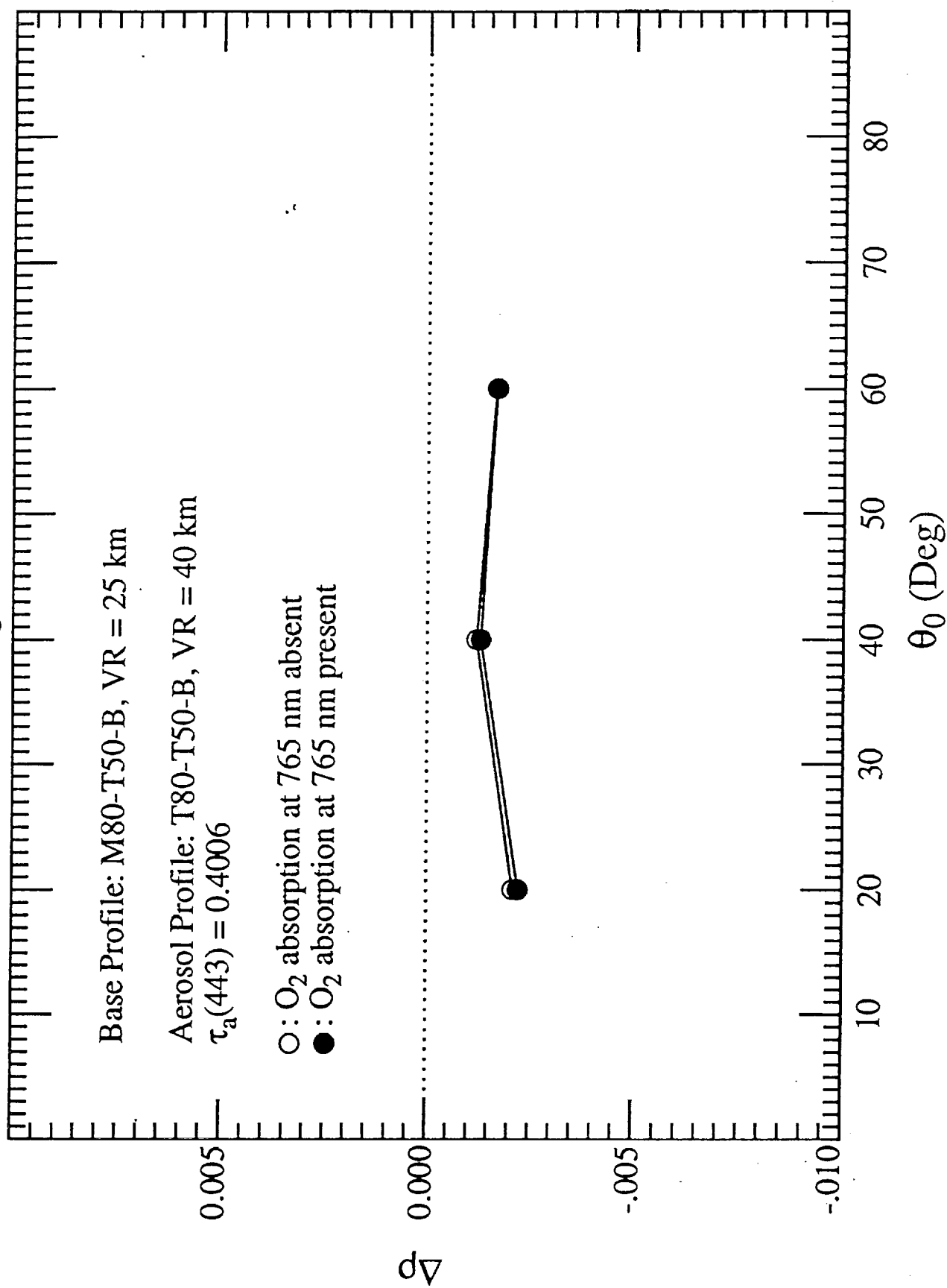


Fig 9b

# Viewing at Edge

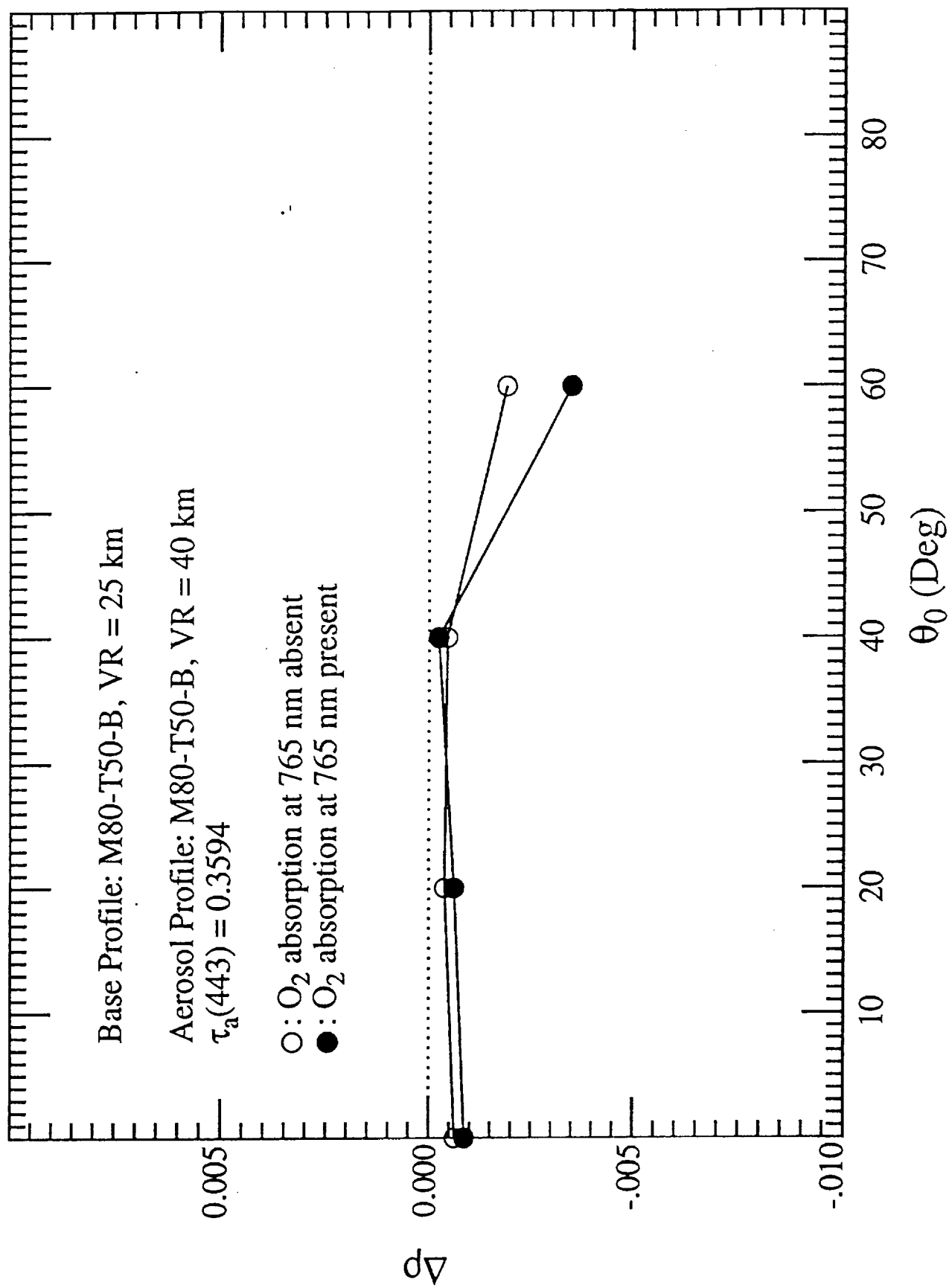


Fig. 9c

Viewing at Edge

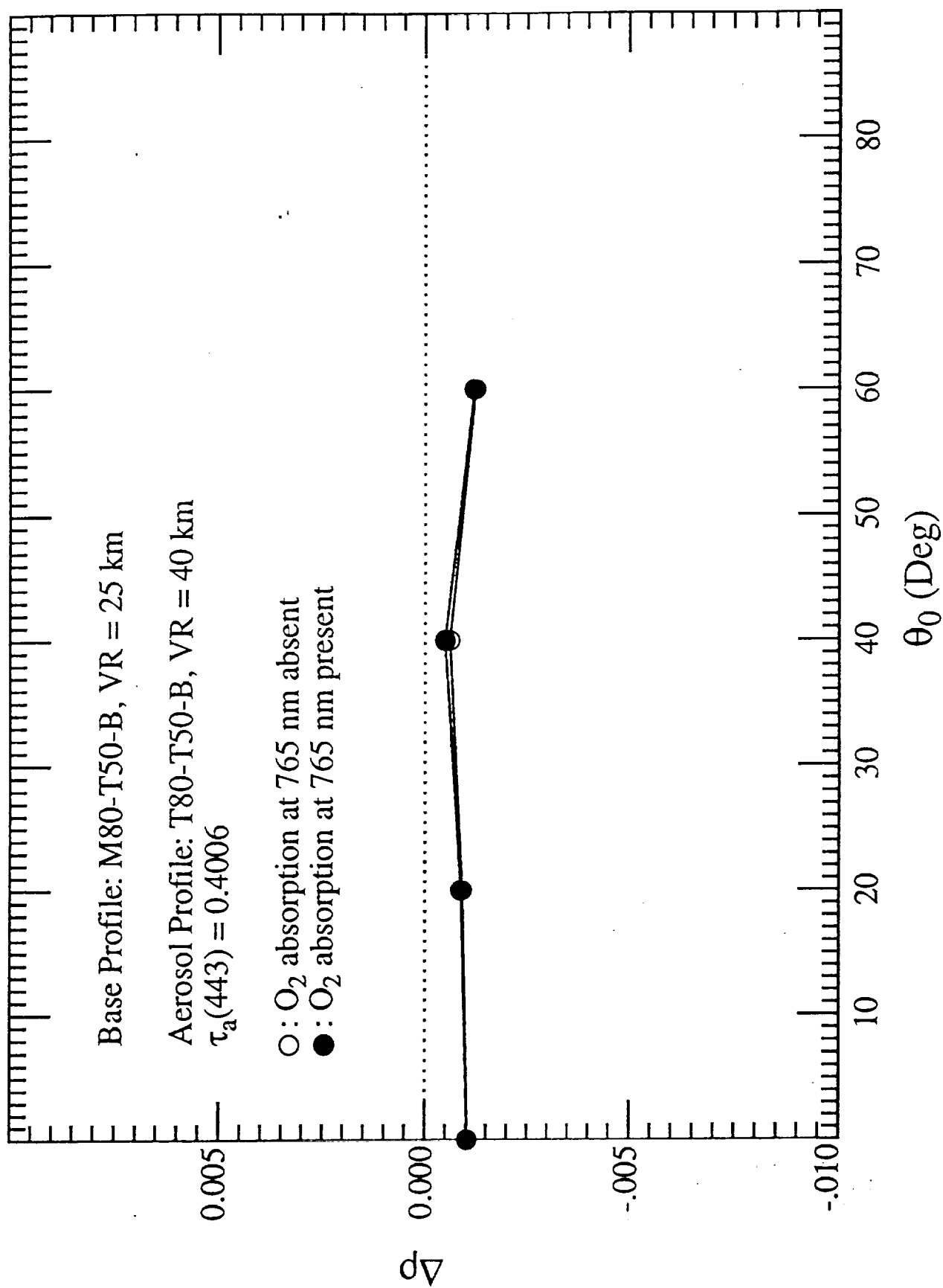


Fig. 9d



Viewing at Center

Base Profile: M80-T50-B, VR = 25 km

Aerosol Profile: M80-T50-B, VR = 15 km  
 $\tau_a(443) = 0.7029$

O: O<sub>2</sub> absorption at 765 nm absent

●: O<sub>2</sub> absorption at 765 nm present

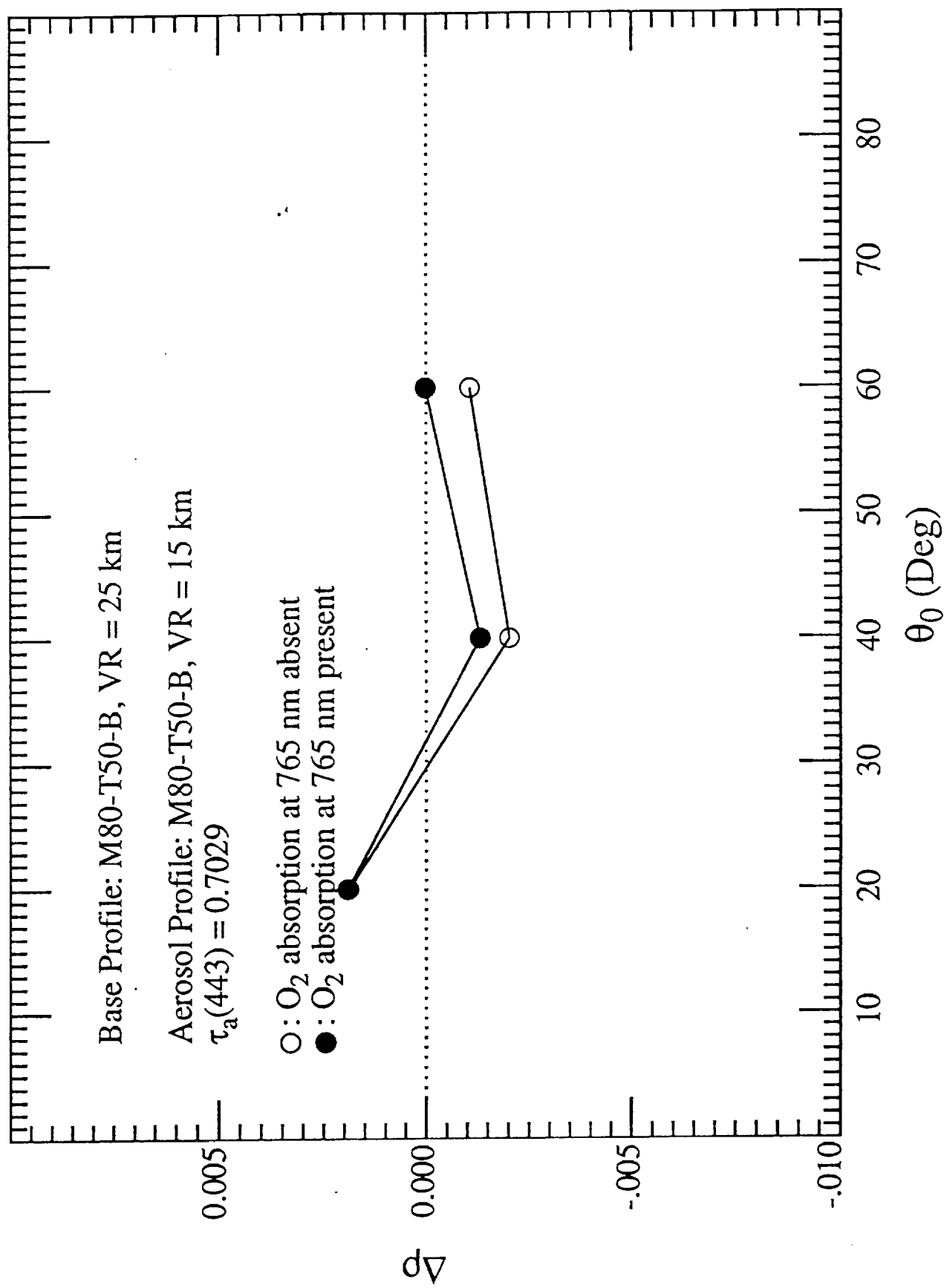


Fig. 10a

Viewing at Center

Base Profile: M80-T50-B, VR = 25 km

Aerosol Profile: T80-T50-B, VR = 15 km  
 $\tau_a(443) = 0.8226$

- O : O<sub>2</sub> absorption at 765 nm absent
- : O<sub>2</sub> absorption at 765 nm present

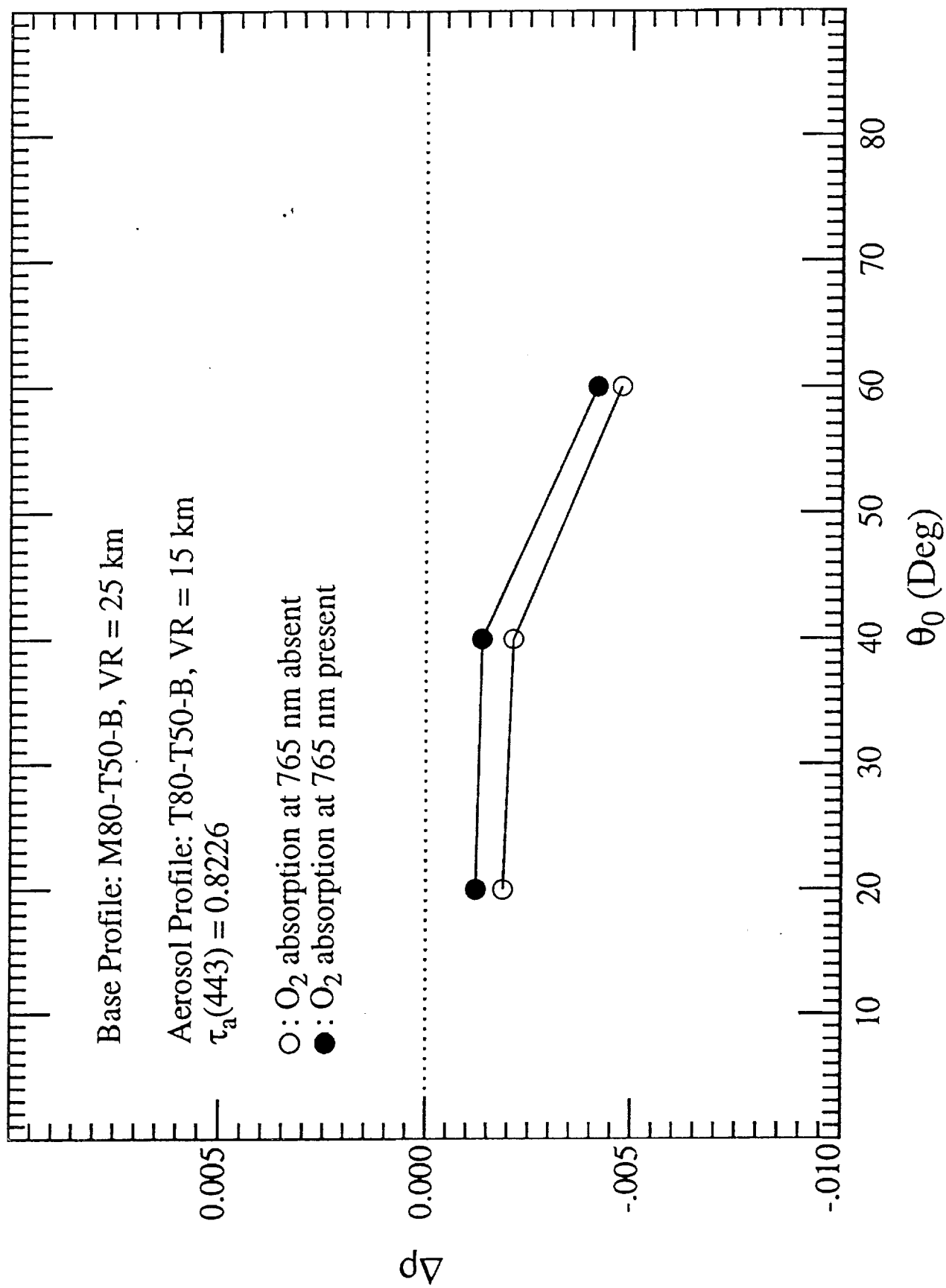


Fig 10b

# Viewing at Edge

Base Profile: M80-T50-B, VR = 25 km

Aerosol Profile: M80-T50-B, VR = 15 km  
 $\tau_a(443) = 0.7029$

O: O<sub>2</sub> absorption at 765 nm absent  
 ●: O<sub>2</sub> absorption at 765 nm present

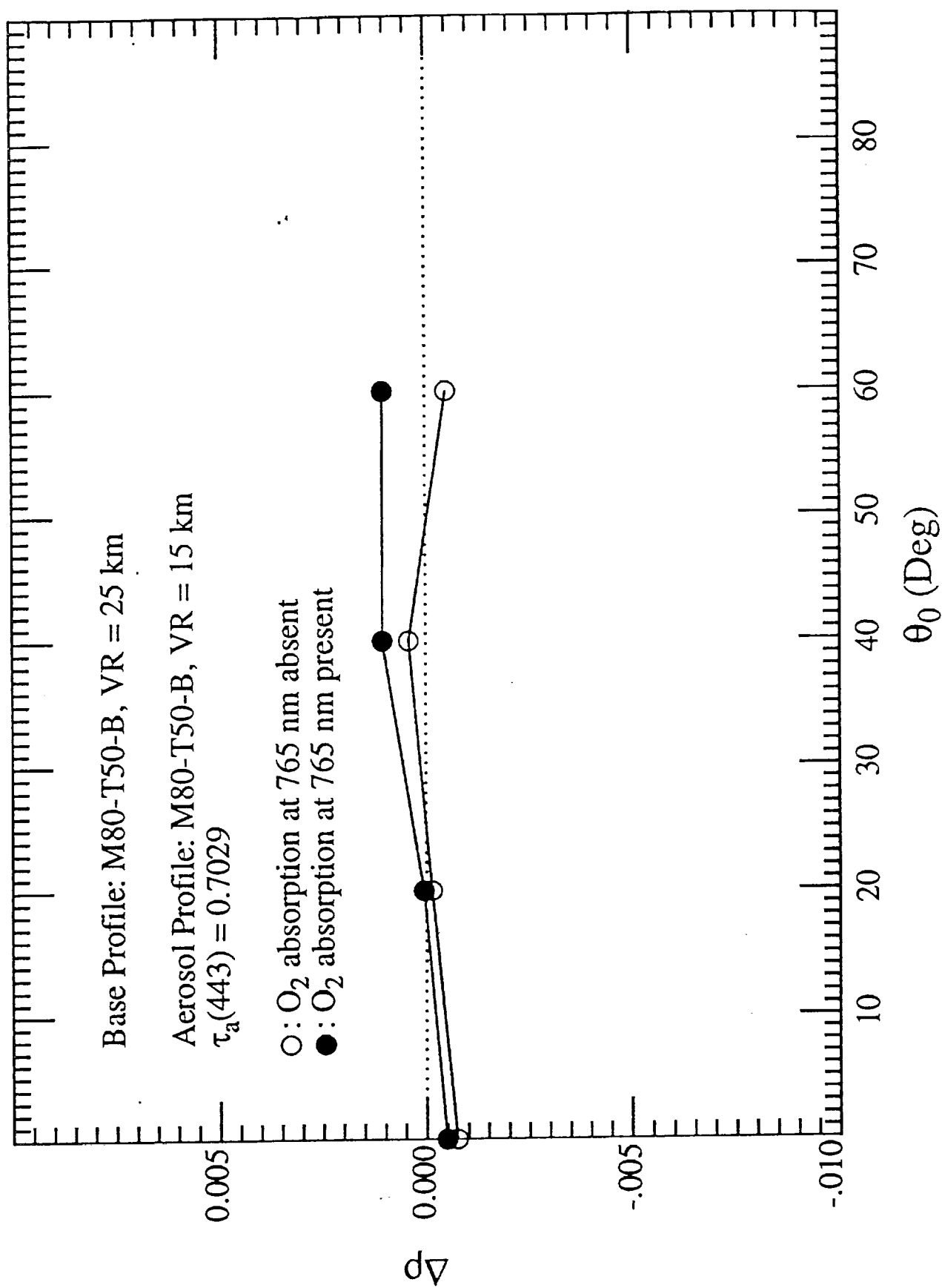


Fig 10c

# Viewing at Edge

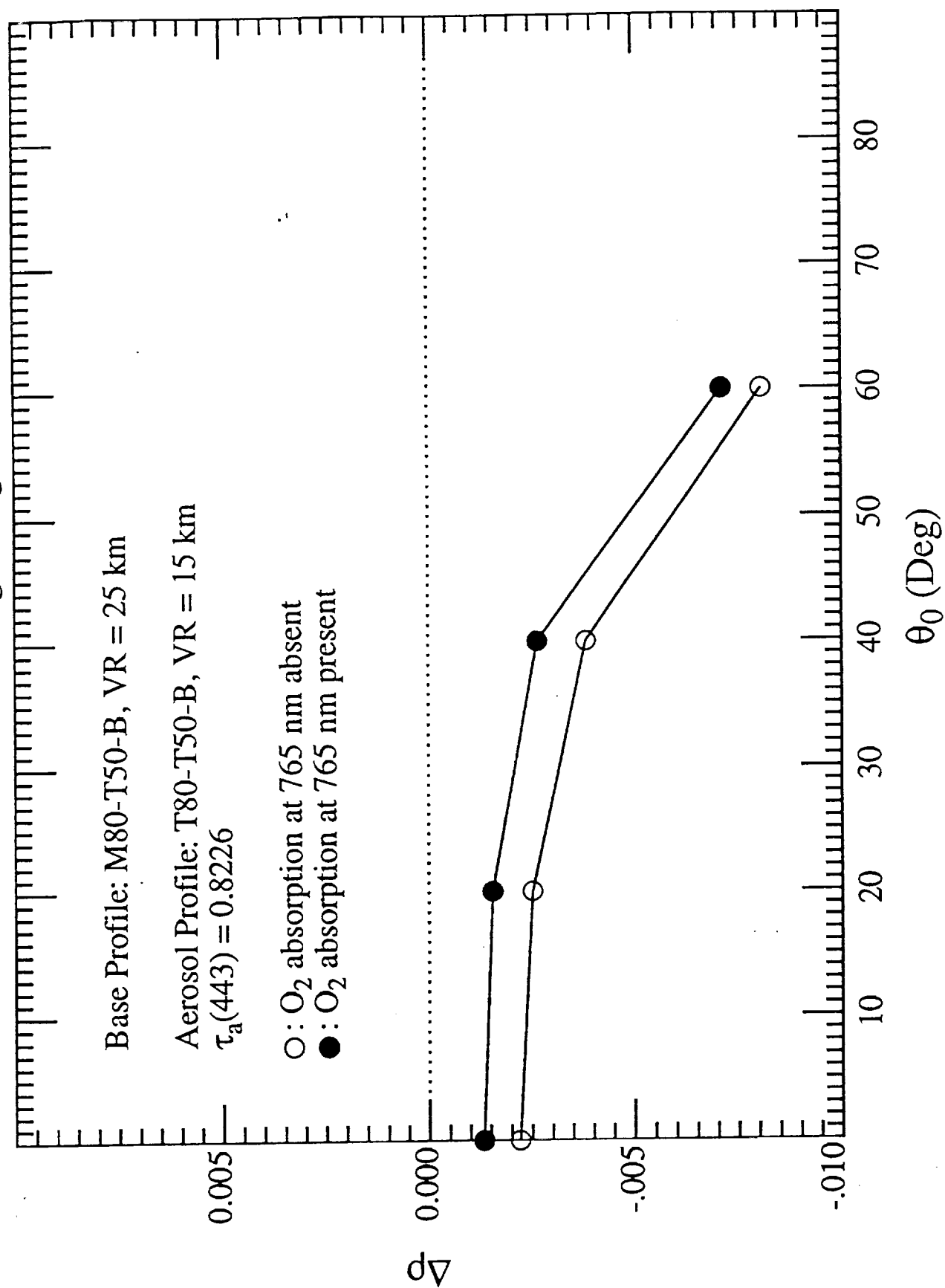


Fig 10d

# Viewing at Center

Base Profile: One layer (0-2 km), M50,  $\tau_a(765) = 0.2693$

Aerosol Profile: M80-T50-B, VR = 40 km

○: O<sub>2</sub> absorption at 765 nm absent

●: O<sub>2</sub> absorption at 765 nm present

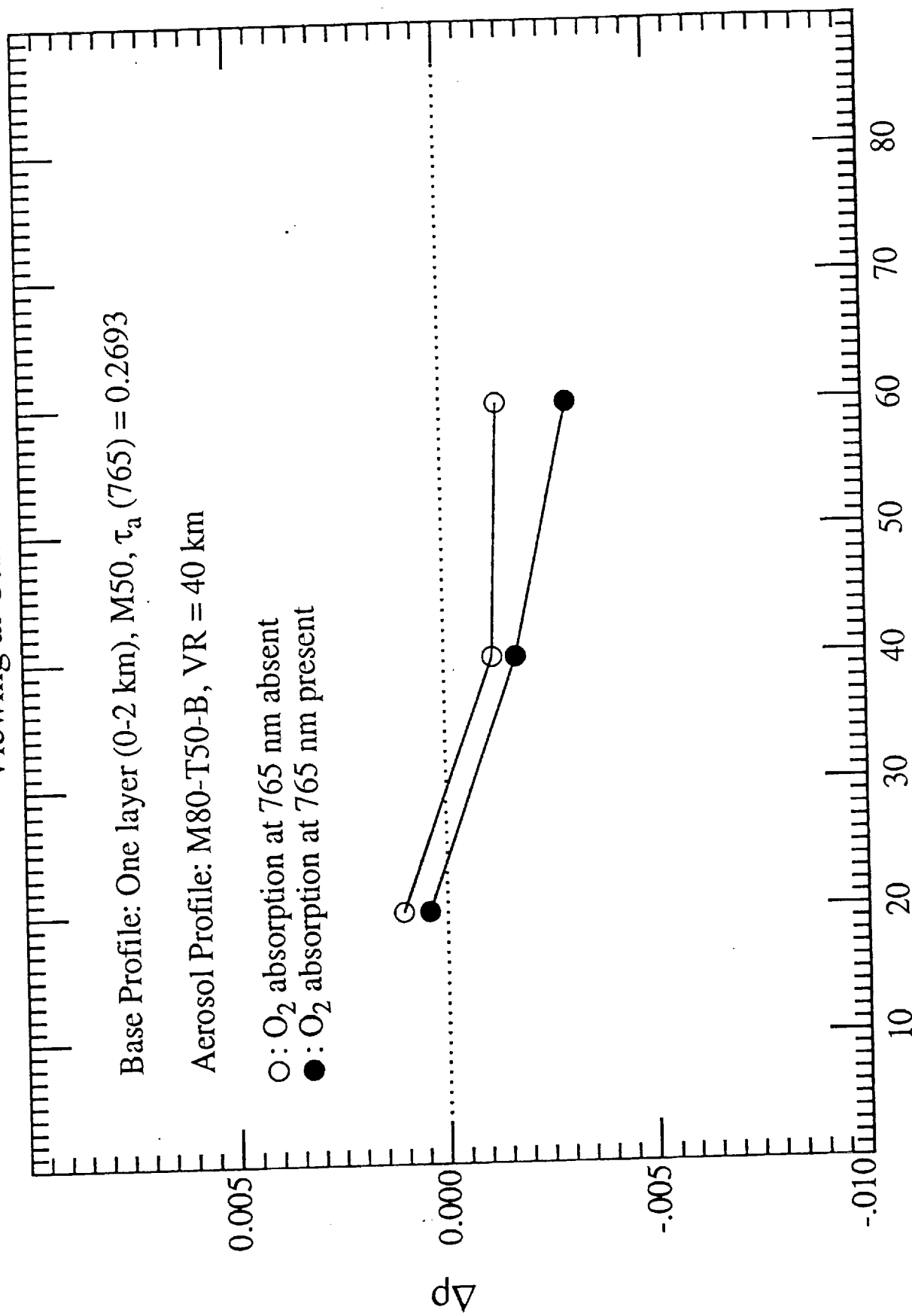


Fig. 11(a)

# Viewing at Center

Base Profile: One layer (0-2 km), M50,  $\tau_a(765) = 0.2693$

Aerosol Profile: T80-T50-B, VR = 40 km

- : O<sub>2</sub> absorption at 765 nm absent
- : O<sub>2</sub> absorption at 765 nm present

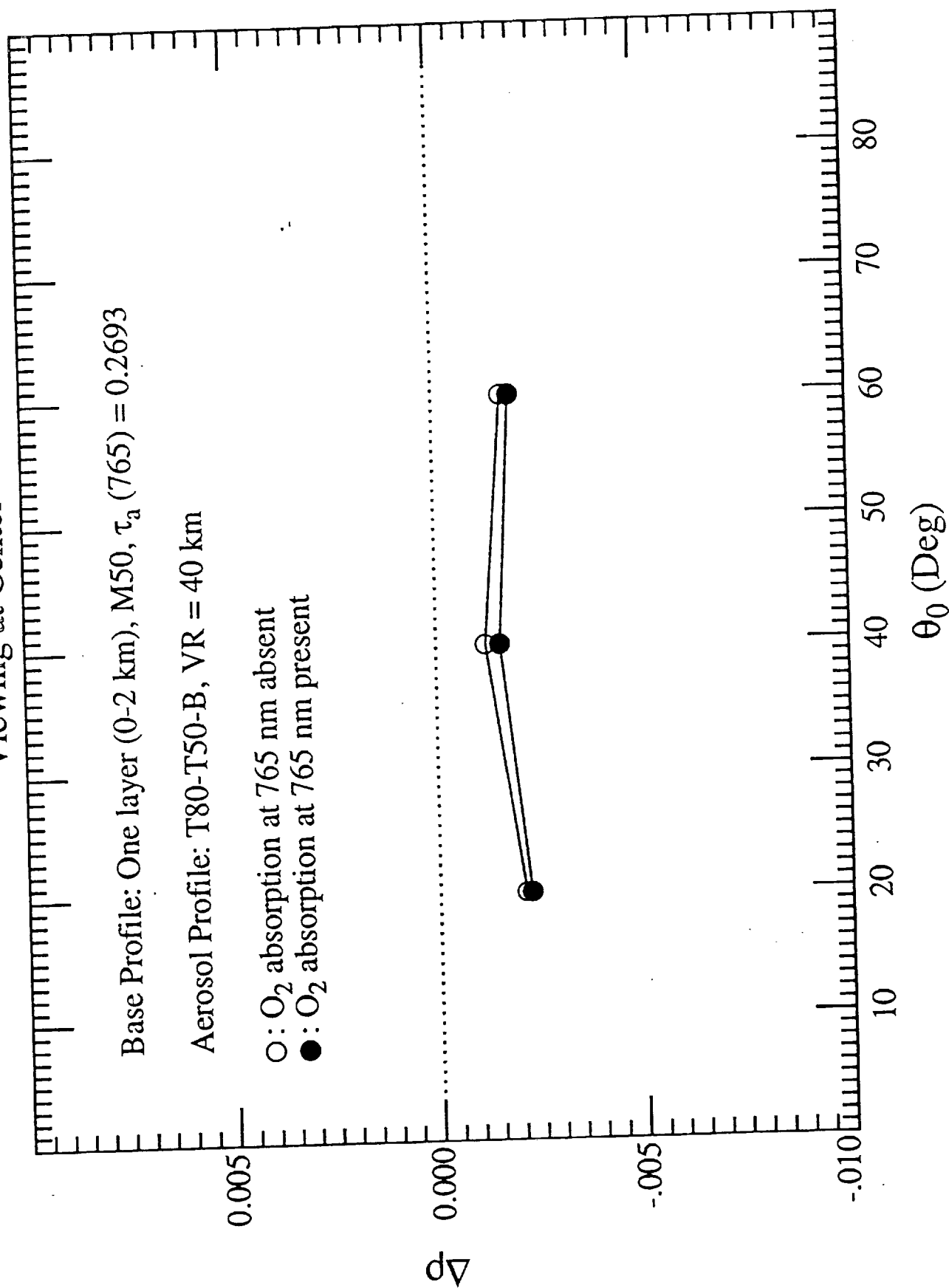


Fig. 11(b)

# Viewing at Center

Base Profile: One layer (0-2 km), M50,  $\tau_a(765) = 0.2693$

Aerosol Profile: M80-T50-B, VR = 15 km

- : O<sub>2</sub> absorption at 765 nm absent
- : O<sub>2</sub> absorption at 765 nm present

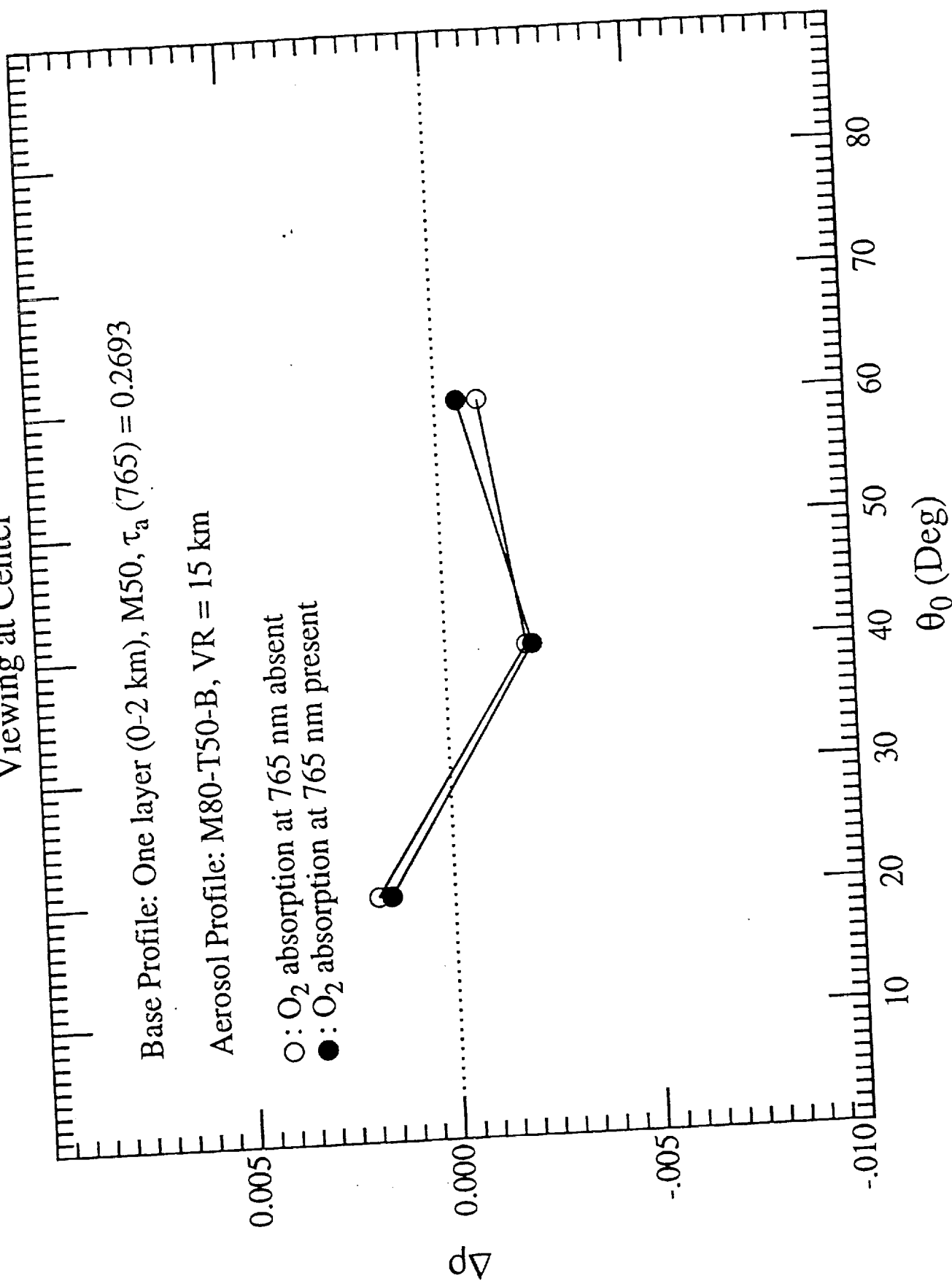


Fig. 11(c)

# Viewing at Center

Base Profile: One layer (0-2 km), M50,  $\tau_a(765) = 0.2693$

Aerosol Profile: T80-T50-B, VR = 15 km

- : O<sub>2</sub> absorption at 765 nm absent
- : O<sub>2</sub> absorption at 765 nm present

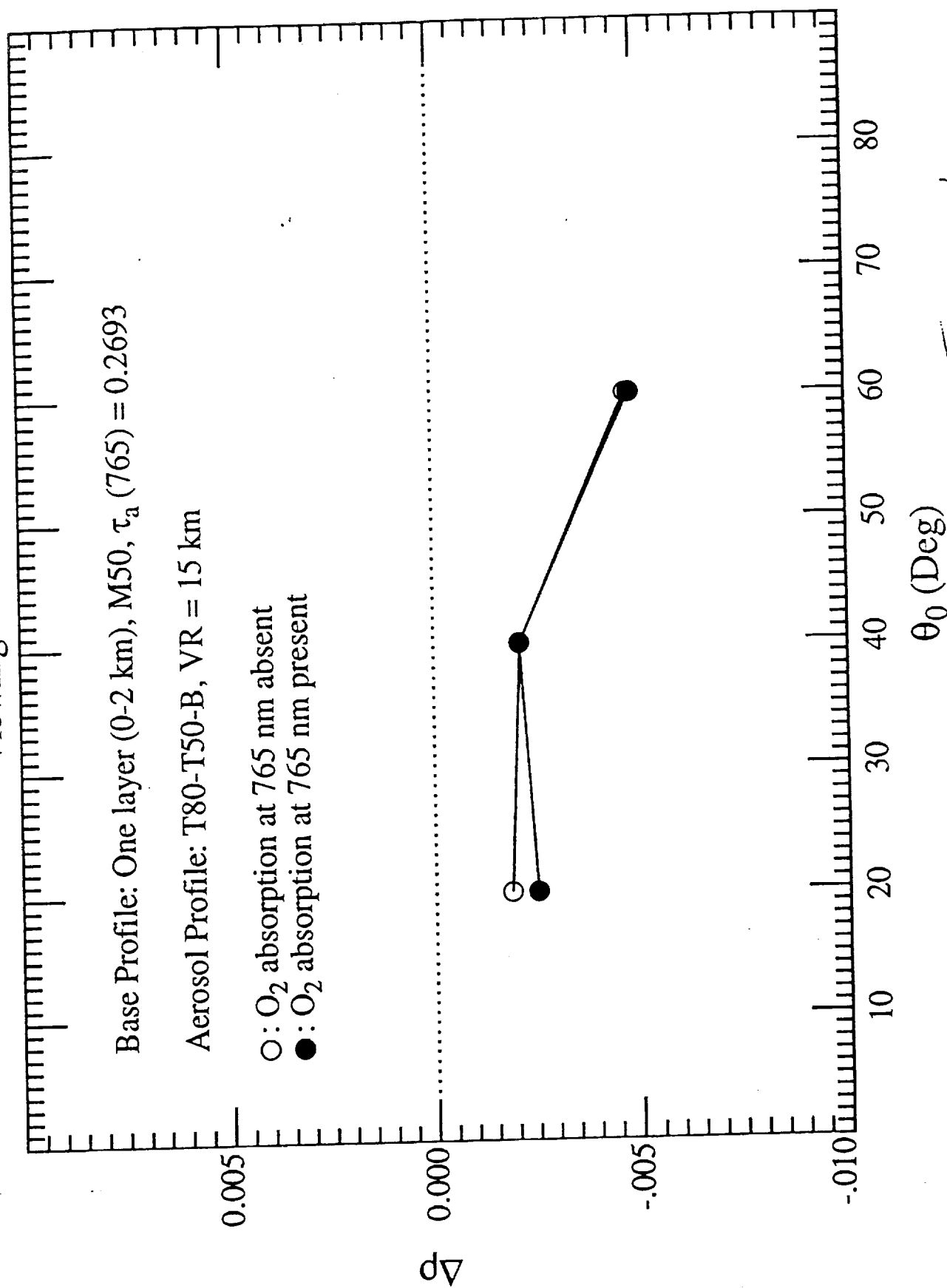


Fig. 11(d)



Viewing at Center

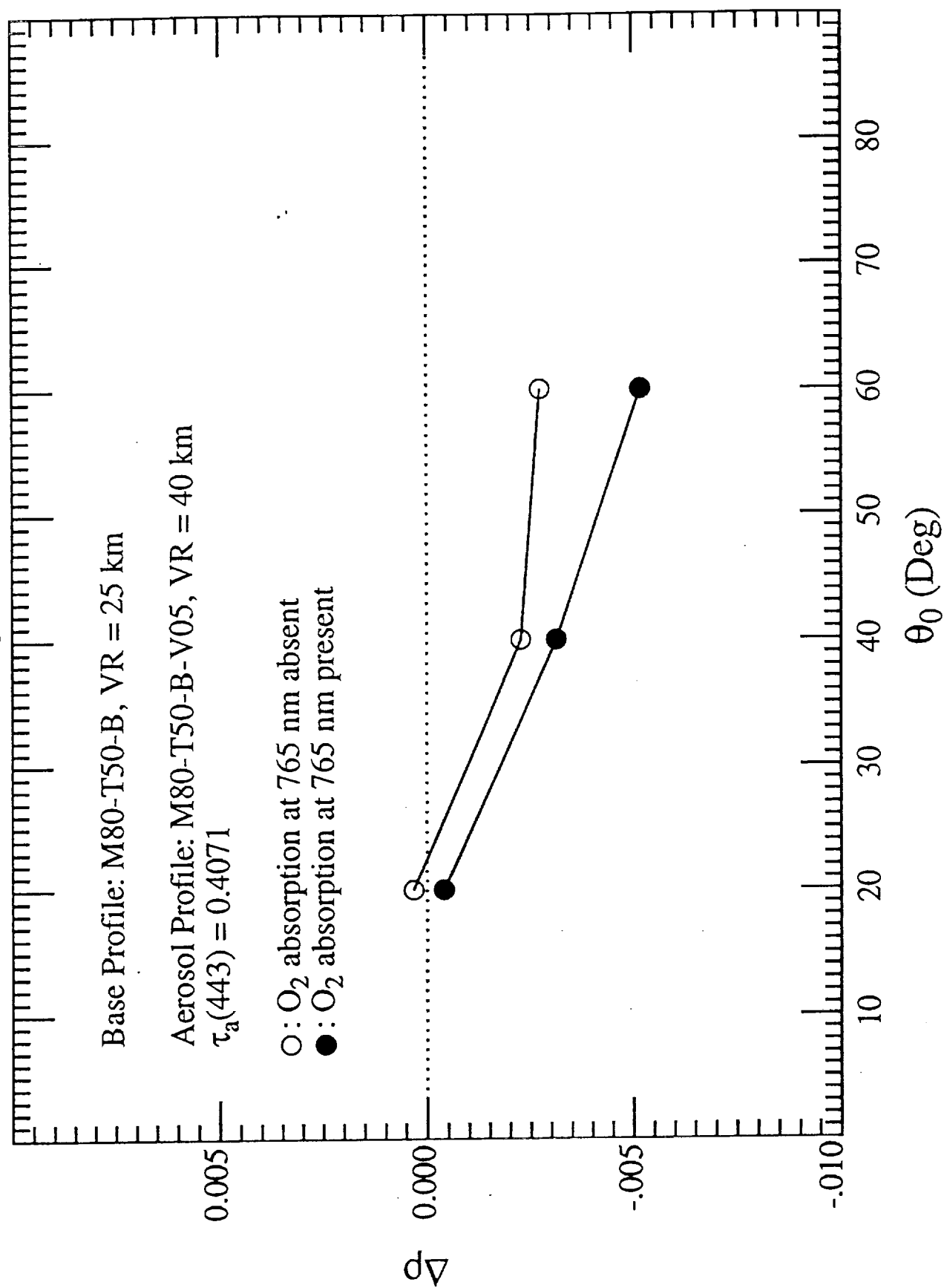


Fig. 12a

# Viewing at Center

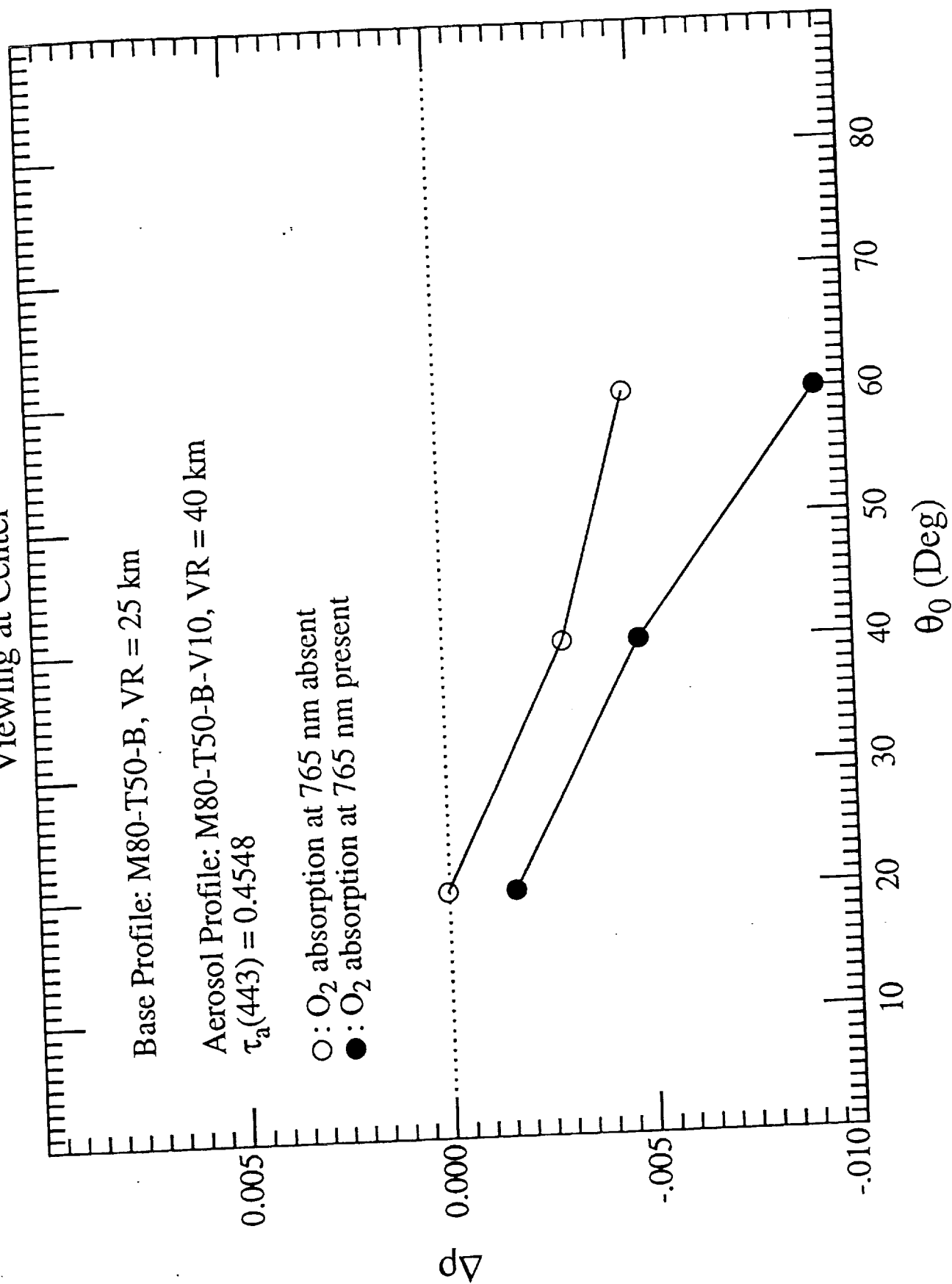


Fig 12b

# Viewing at Center

Base Profile: M80-T50-B, VR = 25 km

Aerosol Profile: M80-T50-B-V05, VR = 15 km

$\tau_a(443) = 0.7506$

○ : O<sub>2</sub> absorption at 765 nm absent

● : O<sub>2</sub> absorption at 765 nm present

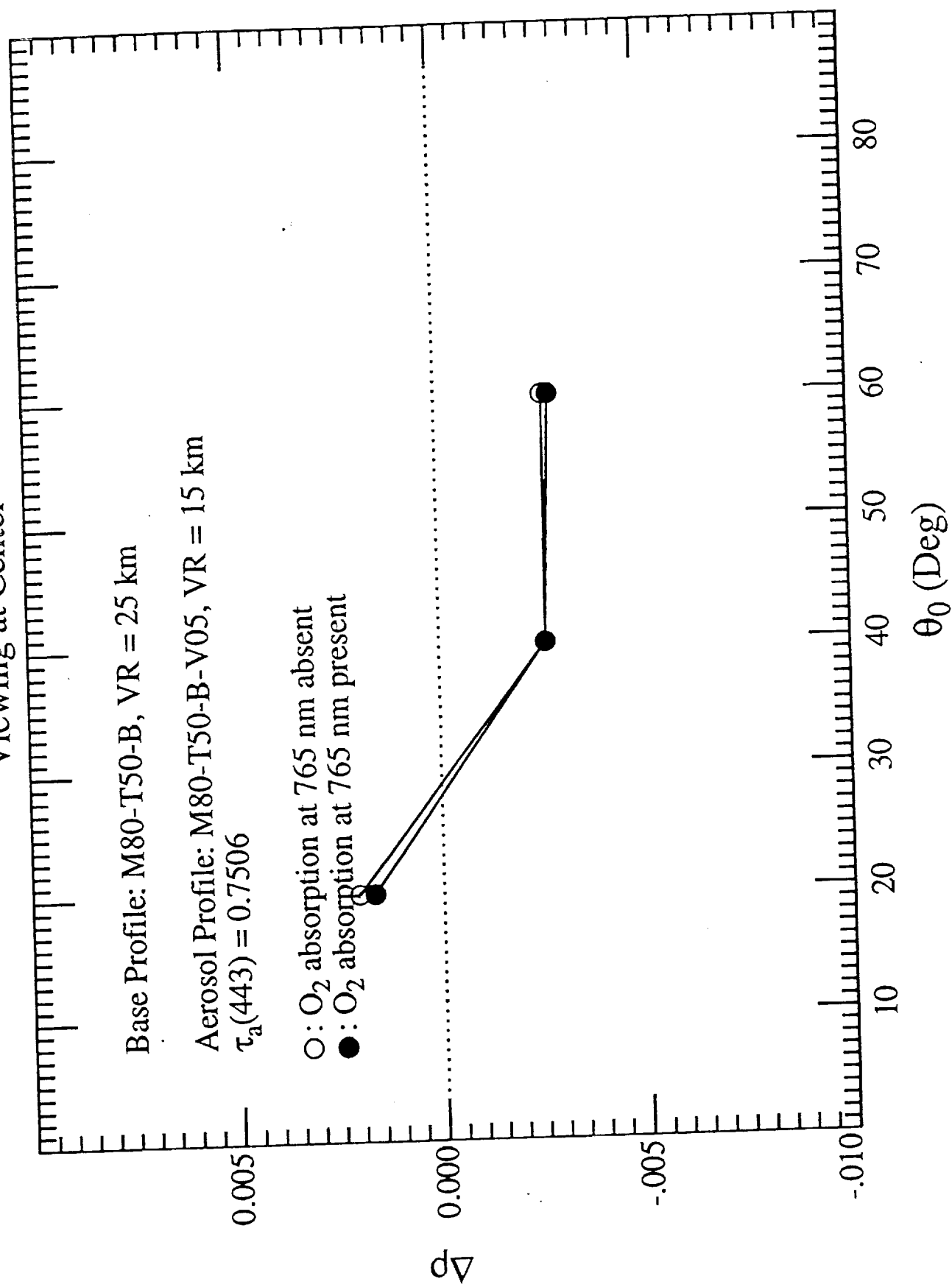


Fig. 12c

Viewing at Center

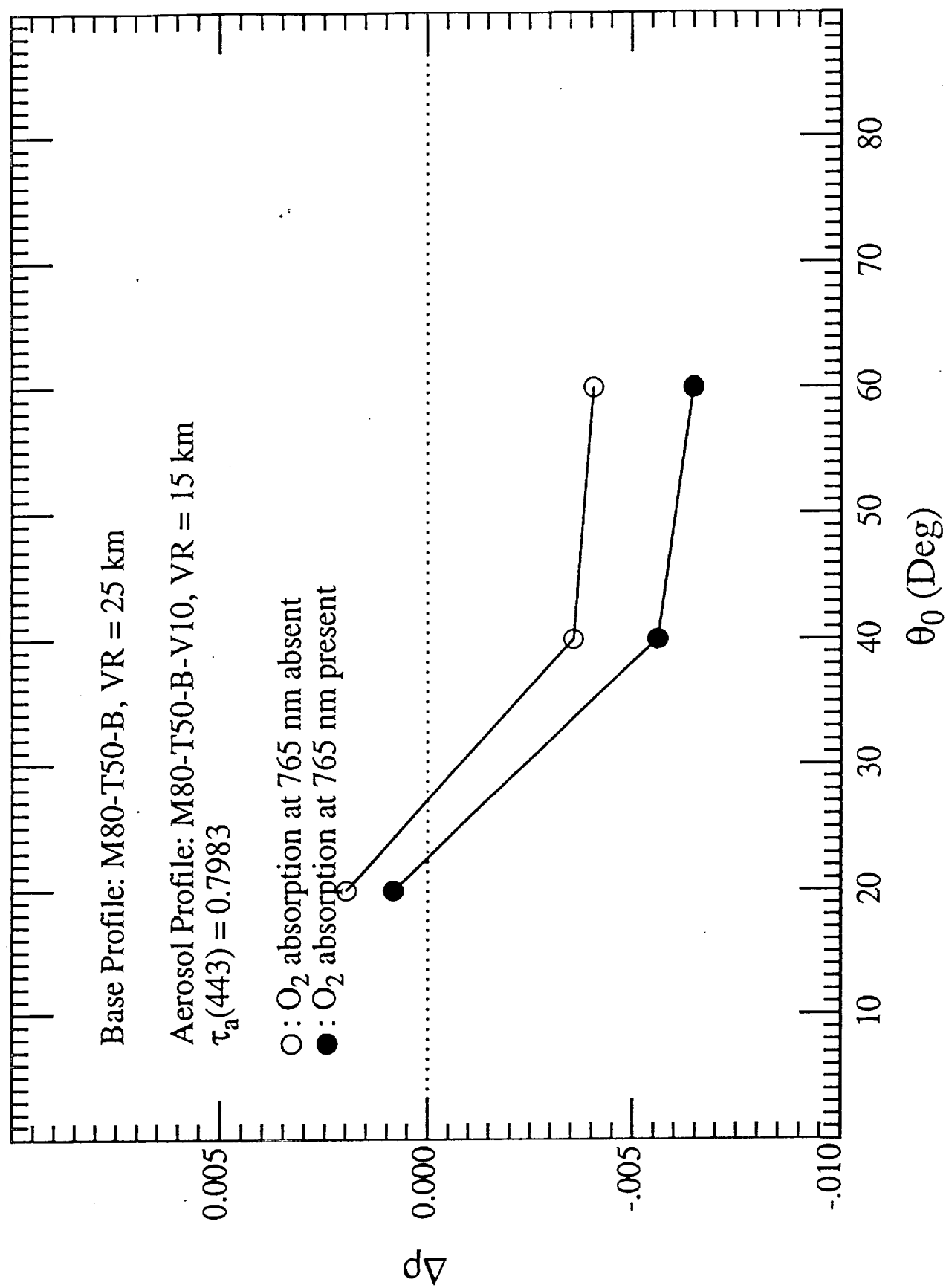


Fig. 12d